UNIVERSITÀ DEGLI STUDI DI TRIESTE

XXX CICLO DEL DOTTORATO DI RICERCA IN NANOTECNOLOGIE

Mechanobiology and mechanotransduction in propathological cellular system

Settore scientifico-disciplinare: BIO/09

DOTTORANDA
Luisa Ulloa Severino

COORDINATORE
Prof. Lucia Pasquato

SUPERVISORE DI TESI
Dr. Denis Scaini

CO-SUPERVISORE DI TESI
Dr. Loredana Casalis

ANNO ACCADEMICO 2016/2017

TABLE OF CONTENTS

Abstract

Cells and tissues respond to environmental forces transducing them into biochemical signals. This cellular property has induced a large interest in biomedical area to study the possibility of using cell (or tissue) mechanical properties (e.g., their stiffness) as a marker for early diagnosis of pathologies or as trigger point to modulate cell/tissue behavior via new, *ad hoc* designed, prosthetic materials. In order to study the mechanical properties of cellular systems, it has been necessary to take advantage of nano-technological tools and techniques such as the Atomic Force Microscope (AFM). In this thesis work I have shown that AFM could represent an excellent tool to evaluate the mechanical properties of different cellular systems. In particular, I have studied the biomechanics in the onset of calcific aortic valve disease, in the tumor associated p53 missense mutants and in myogenesis.

Calcific aortic valve disease is the most common heart disease and is the main cause of aortic stenosis. The primary driver for valvular calcification is the differentiation of valvular interstitial cells (VICs) into a disease-associated phenotype: from myofibroblasts cells to osteoblastic-like cells. Another characteristic of this disease is the significant change in the organization, composition and mechanical properties of the extracellular matrix (ECM) that beside being the result of the dysfunction of the valve cells, seems to contribute to the progression of the pathology altering cellular molecular signalling. In this context, I have initially investigated on the variation of mechanical and morphological properties in human Valve Interstitial Cells when grown on flat polyacrylamide gels at different stiffness. I performed this task using both AFM force spectroscopy and molecular biology essays. My results show that there is a strong direct dependence of cellular rigidity by that of the underlying substrate, resembling a sort of flat matrix. As general rule, any stiffness variation in the matrix affects the activation and consequent nuclear localization of YAP transcription factor. This has allowed me to speculate on the mechanisms regulating human VICs mechanobiology in natural matrix environment identifying three conditions: i) with stiffness lower than ~ 18 kPa, YAP is inactivated; ii) with stiffness between ~18 kPa and ~28 kPa cells could be considered in a “quiescent state”; iii) with stiffness is larger than ~60 kPa a high YAP nuclear localization takes place.

In addition, I observed that inhibition of Rho kinase will result in a preclusion of actin polymerization followed by a reduced cellular stiffness and YAP activation. These processes

revealed to be reversible but, interestingly, stiffness recovery appeared to be slower than the molecular recovery.

I have performed the same AFM characterisation on a more complex experimental model that involves thin sections of explanted stenotic calcific human valves, obtained from patients that underwent aortic valve replacement. I carried out AFM force mapping and immunofluorescence staining on all the leaflet slice. My results demonstrate that the calcified regions of the tissue showed a preferential YAP- nuclear localization.

After this, I moved my studies on the effect of a nanostructured extra-cellular matrix like substrate could have on VICs. I did that taking advantage of multi-walled CNTs carpets grown on glass slides above which I subsequently seeded porcine Valvular Interstitial cells. CNTs substrate developed in our laboratory have two very important features for this study: 1) they are transparent allowing, for the first time, to performed simultaneously AFM force spectroscopy and immunofluorescence essays; 2) their rigidity falls within a range in which I observed a sort of cellular quiescent state, meaning they are "neutral" for cells from the stiffness point of view. Initially I performed a morphological characterization pointing out that CNTs have a positive effect on pVICs, in particular the myofibroblat percentage in VICs developed above CNTs is similar to that of a healthy valve. As consequence of that, I hypothesized a strong interaction between pVICs and CNTs. Interestingly, I performed cell stiffness measurements *via* AFM and I discovered that myofibroblast stiffness is not significantly altered by CNTs. I associated this result to the low density of focal adhesions expressed on these cells by the nanostructures substrate. Therefore, in order to point out the deep CNT/cell membrane interaction, I have broken the cell through osmotic shock making available to direct observation this hidden cellular portion: what I observed is that CNTs below the plasma membrane crossed it completely. At this point I could hypothesize that CNTs, piercing and pinching the plasma membrane, are able to facilitate the creation of clusters of FAs that, at the very end, will increase the cellular rigidity.

Subsequently, I focused my studies to the mechanobiology of tumor associated p53 missense mutants: a mutation associated to a very aggressive cancer, characterized by a strong metastatic potential and drug resistance. In this part of my work I studied the cellular processes and biochemical pathways stabilizing mutant p53 cells. After a drug screening on MDA-MB 231 cell line, a class of drugs, Statins, has been identified as associated with the reduction of p53 mutant levels. Statins have an inhibitor effect on mevalonate pathway and enzymatic activity of RhoA.

Therefore, I performed an AFM force spectroscopy characterization of cells after treatment with different drugs and I confirmed a stiffness reduction in treated cells determined by an actin de-polymerization process. In parallel, I observed that a reduction of stress fibers happened in conjunction with a significant reduction of mutant p53 levels. Following, I studied the same process in a *ex vivo* model taking advantage of AFM nano-indentation procedure. My results established, *in vivo* as *ex vivo*, that the mevalonate pathway is strongly involved in tumor mechanosensing and mutant p53 levels regulation.

At the end of my thesis I studied the muscle development process called myogenesis taking place in muscular tissues. These tissues are characterized by expression of contractile, multinucleated fiber, characterized by a highly-ordered assembly of sarcomeric myofibrils and relevant regenerative capacity. This last feature is strongly regulated by extracellular matrix in terms of spatial organization, structural support and mechanical functionality. These evidences have generated great interest in the design of biomimetic scaffolds able to direct skeletal muscle regeneration. In this framework, I have characterized a new HELP family polypeptide, HELPc, synthetized at the University of Trieste. By characterizing HELPc coating *via* AFM imaging, I found that proteins assemble in an amorphous topology. Following, HELPc coating was used as a substrate for C2C12 myoblasts growth together with HELP and HELP1 control samples. The results showed that the addition of a sequence to from the α2 isoform of collagen type IV, containing to RGD motives, determines an improve of cells activity by combining several methods, as immunofluorescence, Atomic Force Microscopy and Ca^{2+} imaging. In this context, I have studied HELPc three-dimensional hydrogel at different monomer concentration (5% and 7% w/v) and its effects on C2C12 myoblasts development by AFM imaging, force characterization and different molecular biology techniques. I pointed out that topological morphology is the same between the two hydrogels but is different from the properties of a bi-dimensional coating made with the same molecules (2D). Comparing the cell activity results, between gels and coatings, I found some intriguing differences. On the whole, the results underline the potential of HELP family polypeptides as a promising tool for muscle regeneration.

Introduction

1 Mechanobiology

Mechanobiology, or biomechanics, is a discipline that studies the mechanical properties of biological systems and how mechanical forces influence their development, differentiation, physiology and ultimately pathology [1].
In the last decades it has been shown that cells and tissues react to properties such as stress, pressure and extracellular matrix (ECM) microstructure activating specific pathways. This relation opens up the possibility to use cell/tissue mechanical properties as a marker to discriminate between healthy and diseased conditions [2].

1.1 Cell-extracellular matrix interaction

Tissues and organs are formed by cells and by a non-cellular environment in which cells are embedded, called the extracellular matrix (ECM) (Fig. 1). ECM not only contributes to bind cell together, but also provides the physical scaffold into which the cells grow influencing their migration, differentiation, survival, homeostasis and morphogenesis. The ECM consists of an interconnected network of fiber-forming proteins and glycosaminoglycans (GAG) chains, built from proteins and polysaccharides locally produced by the cells in the matrix, which in turn helps in determining cells organization. Cells in fact interact with ECM both mechanically and chemically, to drive the matrix architecture. Starting from a reduced variety of building blocks, a wide variety of matrix materials are built, as the hard structure of the bones, the ropelike structure of tendons or the transparent organization of cornea. The same cells which build the matrix can degrade it, to allow for instance for tissue repairing, but also to guarantee tissue growth, cell division and migration. This close connection between cells and their supporting matrix is operated by cell-matrix receptors and is intimately dynamic, with the cells organizing the matrix and the matrix in turn influencing cell fate through the exchange of mechanical signals from the matrix to the cytoskeleton and *viceversa*. Therefore when a disease, as for instance cancer of a cardiovascular disease, occurs, the ECM should be strongly involved.

In the next paragraph, we will review the major macromolecular component and superstructures of the ECM in animal tissues, as well as the basic players in cell-matrix junction formation, in the framework of their mechanical interplay and proteoglycans [3].

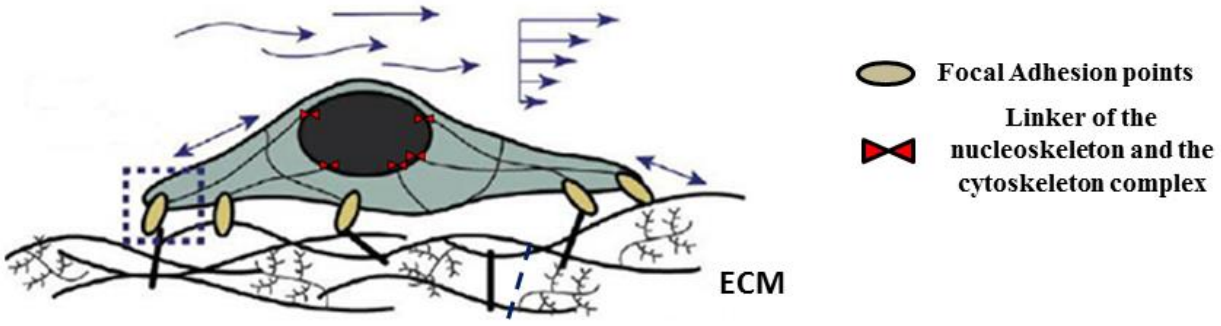

Figure 1: *Cellular and extracellular matrix scheme* [4].

1.1.1 ECM components

The major classes of macromolecules constituting the ECM are three: 1) glycosaminoglycans (GAG), unbranched, highly charged, large polysaccharides, and their covalent assembling with protein to form proteoglycans; 2) fibrous proteins, member of the collagen family; 3) non-collagen glycoproteins, proteins linked to oligosaccharides. Hereafter we review the structure of the major components of the ECM.

- ***Proteoglycans (PGs)*** (Fig. 2a) are the major component of the ECM. They consist of a core protein covalently attached to glycosaminoglycans (GAG) chains. GAGs can be of six different types called chondroitin sulfate (CS); dermatan sulfate (DS); heparan sulfate (HS); heparin (HP), Keratan sulfate (KS), hyaluronan (HA). CS, DS, HS, HP are composed by repeating disaccharides of hexosamines (N-acetyl-galactosamine or N-acetyl-glucosamine) and uronic acids (D-glucuronic acid or L-iduronic acid) that are being sulfated at various positions, while KS is composed of repeating disaccharides containing N-acetyl-glucosamine and galactose. HA is the only GAG that is not covalently bound to any core protein. Proteoglycans are very important in the onset of various diseases, because they are markedly modified during ECM remodeling [5]. This phenomenon occurs in two ways: 1) strong interactions between PGs and other ECM components that define PGs GAGs chains and 2) their preferential interaction with growth factors, cytokines and chemokines.

- ***Collagen*** (Fig. 2b) constitutes the most abundant fibrous protein in the ECM of connective tissues and is synthesized by fibroblasts [6]. There exist twenty-eight different collagen types, the type I being the major structural element in tissues. In all cases, collagen basic structural motif consists of three polypeptide chains wound together to form a triple helix which then elongates to form fibrils. Increased collagen deposition characterizes some pathologies, as tumor [7] or cardiomyopathies [8], and reflects into an ECM rigidity increase.

- ***Other non-collagen fibrous protein structures***

- ***Elastin*** (Fig. 2e) is the elastic fibrous component of tissues. It is synthesized starting from the monomeric precursor called tropoelastin. Tropoelastin is a 60-70 kDa protein and is formed by a hydrophobic domain, that induce the tissue elastic properties [9]. and lysine-containing cross-linking domains (LOX-like domains) that stabilizes it. In fact, the tropoelastin secreted by the cells interacts with microfibrillar proteins, which are cysteine-rich glycoproteins of large size (~ 350 kDa), by a cross-linking through LOX-link domains forming the elastic fibers. The elastic fibers bind cell surface throughout integrin-binding Arg-Gly-Asp (RGD) sequences [10].

- ***Fibronectin (FN)*** (Fig. 2d) is a fibrous protein expressed in the ECM of different cell types. It is a high molecular weight glycoprotein (440 kDa) which binds both the main protein component of the ECM and specific membrane receptor proteins called integrins. It is formed by two subunits that are united with disulfide bonds at their C-termini. Integrins bind FN in two possible cell-binding sites within FN, either the RGD-dependent cell binding domain or the CS1 segment of the alternatively spliced V region [11]. *In vivo* the fibronectin molecules must be assembled in fibrillar state in order to be active. The active form can be synthesized by using the soluble fibronectin derived from plasma, or cells can produce their than are assembled into fibers [12].

- ***Laminins*** (Fig. 2c) are large cross-shaped glycoproteins. Laminin molecules, throughout the interaction with other ECM components, participate at the organization of ECM and to cell adhesion [13]. There are different laminin isoforms and each one of them is

involved in a particular tissue function. They influence cell differentiation, adhesion, migration and are involved in many human congenital diseases [11].

ECM interacts with the cells through cell surface receptors, such as integrin, discoidin domain receptors which bind a number of different collagen types and play important roles in embryo development and CD44 receptors involved in cell–cell interactions, cell adhesion and migration, in particular of lymphocytes. Indeed, through these receptors cells are continuously stimulated by ECM signals that determine their functions and behavior [14]. Integrins constitute the most relevant receptor family (see section 1.2). They function as a link between the actin fibers in the cytoskeleton and the ECM fibers: intracellular signals are transmitted to the outside of the cell by influencing integrin affinity for ECM ligands affecting in turn ECM assembly, cell migration ad adhesion processes [15].

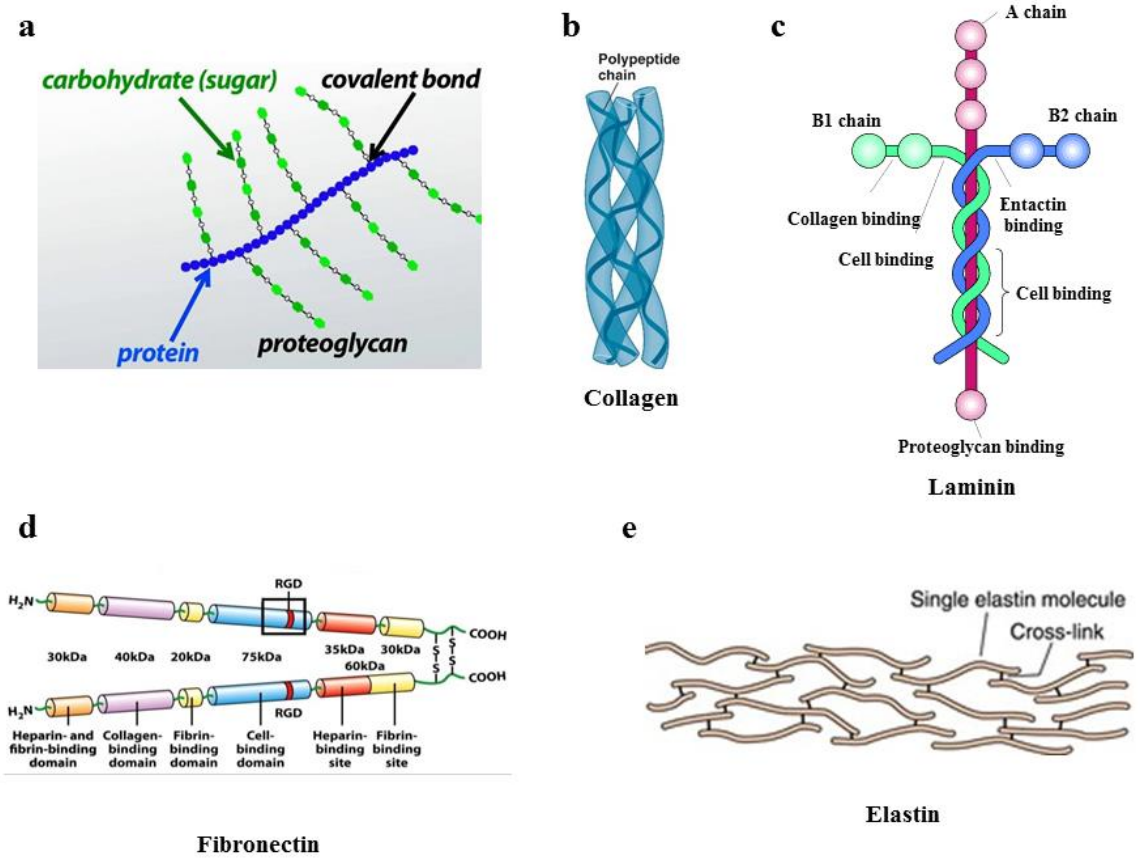

Figure 2: *ECM fibers; (a)Proteoglycan, (b)Collagen, (c)Laminin, (d)Fibronectin and (e)Elastin structures*

1.2 Cytoskeleton rearrangement and cell force transmissions

Cytoskeleton is the cellular part that stabilizes cell shape through internal organization of complex network of interlinking actin filaments, intermediate filaments and microtubules, that extend throughout the cytoplasm, from the nucleus to the plasma membrane (Fig. 1). It is also responsible for the mechanical support of many cell functions such as cell division and movement [16]. The structures responsible for cell shape are actin filaments, helical polymers of the actin protein, which can organize into different supramolecular assemblies, as linear bundles, 2D networks or 3D gels. The formation process of actin filaments is called polymerization. It proceeds in three sequential phases. The first phase is marked by a period in which G-actin forms short, unstable oligomers. Once the oligomer reaches a certain length it acts as a stable nucleus, which elongates into a filament adding actin monomers to both of its ends (second phase). In the third phase as F-actin filaments grow, the concentration of G-actin monomers decreases until reaching an equilibrium with the filament [17]. Actin filaments are known to respond to external forces through their rearrangement (see Mechanotransduction section) leading to the variation of cell mechanical properties [18]. This cellular property, called cell polarization, is fundamental to the functions of most eukaryotic cells, as development, intracellular transport, cell division, differentiation, and directional cell movement. Front–rear cell polarity occurs in both single cells and cell collectives. During migration a single cell must first polarize and forms its front or leading edge, which is characterized by cytoskeleton assembly that produces a protrusion called lamillopodia. These filaments are connected with extracellular environment via large protein complexes called focal adhesion points (FAs), which we will discuss in detail in the next paragraph. FAs are located on the plasma membrane and include integrins, and are the constitutive interface for mechanical force transduction between the extracellular and intercellular environment. Anchoring of mature cell–ECM contacts to actomyosin allows the formation of longitudinal stress fibers (see paragraph 1.2.2). Other two components, we have already mentioned before, are intermediate filaments and microtubules. Microtubules are composed by the globular proteins called tubulin which is a dimer formed by two 55 kDa polypeptides, α-tubulin and β-tubulin [19]. In addition, a third type, called γ-tubulin is specifically located in the centrosome. In order to form the microtubules, the tubulin dimers polymerize into 13 linear proto-filaments assembled around a hollow core. Consequently, microtubules are polar structures with two distinct ends: a fast-growing plus end and a slow-

growing minus end. This polarity is an important consideration in determining the direction of movement along microtubules, as in the case of actin filaments which polarity defines the direction of myosin movement. The microtubules are involved in the duplication of centrosome during mitosis process. Differently from actin filaments and microtubules, the intermediate filaments are composed of a variety of proteins. More than 50 different proteins have been identified and classified into six groups based on similarities between their amino acid sequences [19]. The first stage of filament assembly is the formation of dimers in which the central rod domains of two polypeptide chains are wound around each other in a coiled-coil structure. The dimers then associate to form tetramers, which can assemble end to end to form proto-filaments. The final intermediate filament contains approximately eight proto-filaments wound around each other in a ropelike structure. In contrast to actin filaments and microtubules, intermediate filaments are apolar without having distinct plus and minus ends. Intermediate filaments are most needed to strengthen the cytoskeleton of cells in the tissues of multicellular organisms, being mainly involved in cell-cell junctions.

1.2.1 Focal adhesion points

Focal adhesion points (Fig. 4) are protein complexes formed by more than 150 proteins, which are linking the actin cytoskeleton to the ECM through the integrin receptors [20]. It has been shown that these structures are mechanosensitive and that the ECM mechanical properties contribute to the dynamic FAs assembly/disassembly [18,21]. The shape of the cells and many cellular processes, such as proliferation, migration, differentiation and in the onset of malignant phenotype, are associated with FAs size and density. The main players FA points are integrins, talin, paxilin, vinculin and focal adhesion kinase (FAK).

- ***Integrins*** (Fig. 5a) constitute the superfamily of transmembrane receptors which mediate cell-ECM adhesion (the other adhesion protein superfamily being represented by cadherins, which instead mediate cell-cell adhesion). Integrins are heterodimeric glycoproteins formed by two non covalently bound α and β subunits. There are eighteen different α subunits and eight β subunits, for a total of 24 combinations of heterodimers. Integrins have a large extracellular domain (~80–150 kDa), a single-spanning transmembrane domain and a short cytoplasmic tail domain (Fig. 3). Their extracellular domain binds ECM proteins as collagen, fibronectin, laminin and cellular receptors as

different adhesion proteins, while the intracellular domain communicates directly or indirectly with the cytoskeleton network [22] modulating actin polymerization and signal transduction pathways that control cell adhesion, migration, proliferation, differentiation and apoptosis. However, integrin itself in the short cytosolic tail does not have any binding site for actin. It requires then the recruitment of different proteins, as talin/kindlin and vinculin, to mediate this binding. The talin activated integrin form consists in a conformation in which the cytosolic tail and the transmembrane domains separate and the extracellular domain extends out. In this conformation integrins can bind protein ligands in the ECM promoting adjacent integrin clustering, essential to guide the recruitment of other proteins for the formation of tight but dynamically evolving FAs, which in turn regulate the binding/assembling of actin cytoskeleton and signal pathways that control cell adhesion, migration, proliferation, differentiation and apoptosis [23]. The entire stiffness sensing machinery of the cell has a contractile/adhesive dynamic nature, given by different molecular players mechanically linked to form a "molecular clutch" [24].

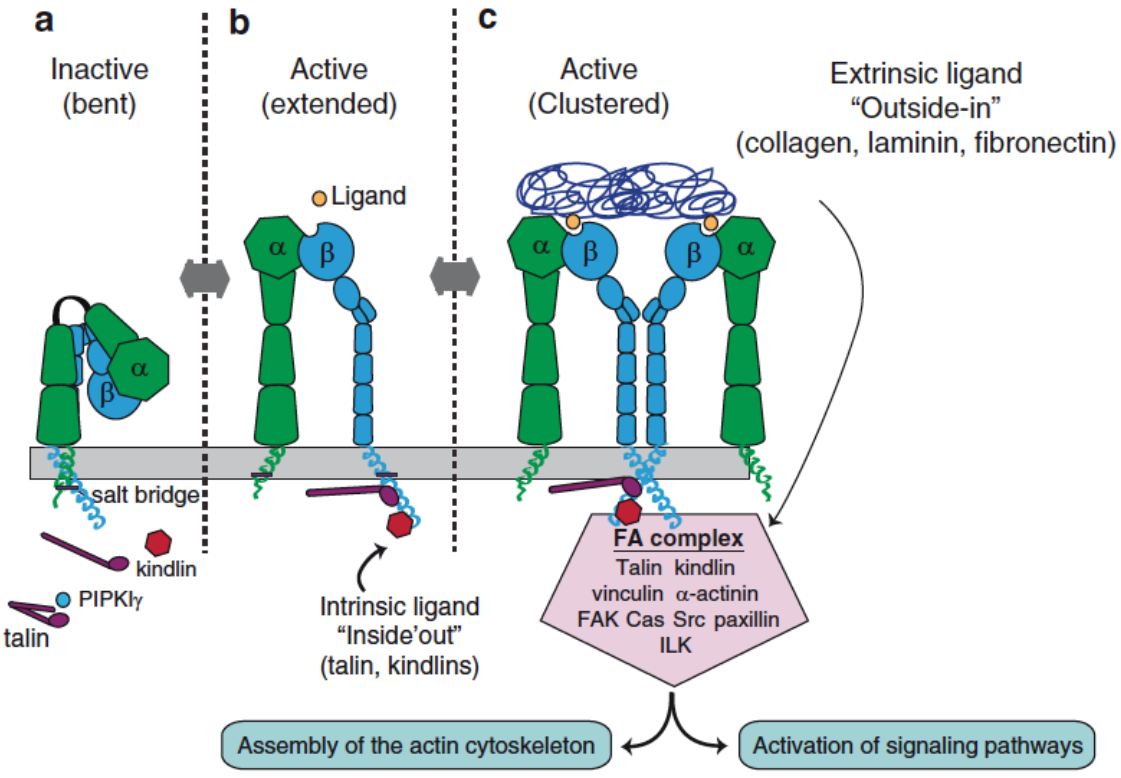

Figure 3: Integrin Structure and Function

- ***Talin*** (Fig. 5e) is a protein of ~2500 amino acids. It has two integrin-binding sites in the head portion, three actin-binding sites in the tail portion. It has been shown that their recruitment is amplified by cytoskeleton tension [25]. Talin together with vinculin have a relevant role in two important process of the mechanotransduction: they increase the integrin mediated actin-ECM affinity binding. Talin in particular strengthen the clutch linkage between ECM-bound integrins and actin by binding to actin on one side and to the cytoplasmic tail of β-integrins on the other. Vinculin reinforce the ECM-binding side to integring. Following a recent model of the molecular clutch proposed by the group of Roca-Cusachs P. (Fig. 4) [24,26], there is a rigidity threshold for transmitting the force signal from ECM to the actin, above which talin is required. This threshold correlates with the growth of vinculin-rich FAs. Higher traction forces induce in fact talin unfolding, exposing cryptic vinculin binding sites and therefore favoring the recruitment of vinculin to reinforce the clutch. At low stiffness ECM no forces are transmitted through talin since integrin-ECM bond lifetime is faster than the loading rate on the clutch. Beyond a certain threshold, clutch loading gets faster than the integrin-ECM bond lifetime resulting in force transmission to talin which promotes talin unfolding, vinculin binding and overall an increase of adhesion and traction force. At his same threshold FAs grow and associate to actin stress fibers, inducing the nuclear translocation of the mechanosensitive transcription factor YAP (see below).

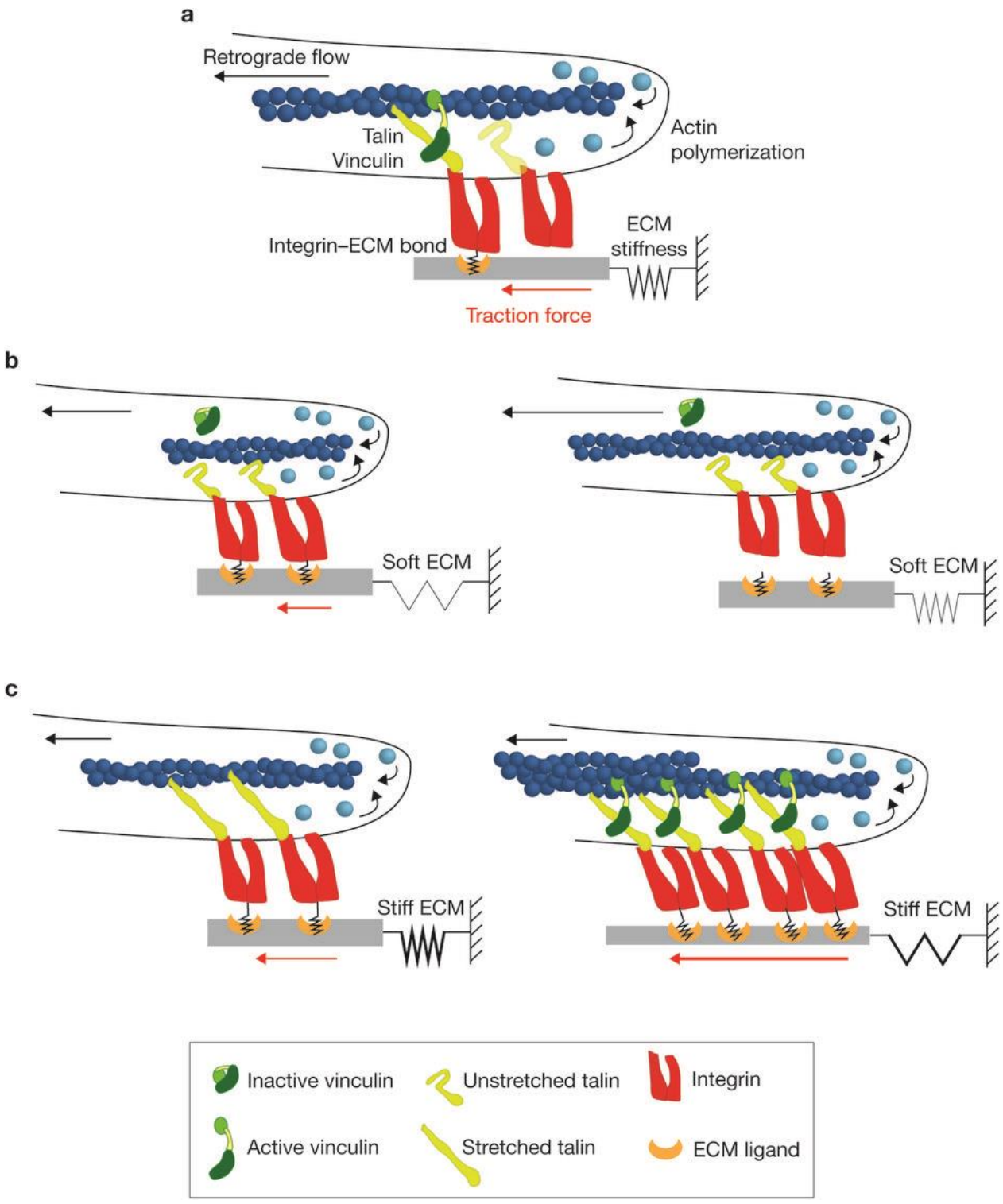

Figure 4: *Schematic molecular clutch proposed by the group of Roca-Cusachs P. described in News and Views of Swaminathan V.* [26]

- ***Vinculin*** (Fig. 5b) accumulation in FAs regulates intracellular tensions and ECM stiffness [27]. Vinculin is a protein of about 1066 amino acids formed by a global head (V_H) and a tail domain (V_T). V_H contains the integrins binding site while V_T contains the actin binding site. As mentioned above, vinculin is activated when localized in FAs, forming a link between integrins and the cytoskeleton associated with the generation of mechanical forces [28].

- ***Paxilin*** (Fig. 5d) is a protein which participates to assembly and disassembly the focal adhesion points through the recruitment of all the proteins necessary for the formation of these [29]. This protein is formed by N-terminus rich in leucine and C-terminus rich in cysteine and histidine. Paxilin is a link between the FAK and Vinculin by influencing the actin polymerization.

- ***Focal adhesion kinase (FAK)*** (Fig. 5c) is involved in a FAs formation and in the regulation of many biomechanical processes, such as cell cycle progression, cell survival and cell migration. The FAK structure is made up by a N-terminus domain which facilitate protein–protein interactions, the kinase domain which contains three tyrosines for phosphorylation and a last C-terminus domain with two subdomains, a protein-binding domain and a catalytic domain [30]. It has been shown that the FAK protein is very sensible to stretching of cells: the integrin aggregation determines the number of recruited FAKs during cell stretching determining a grow of the FAs [31].

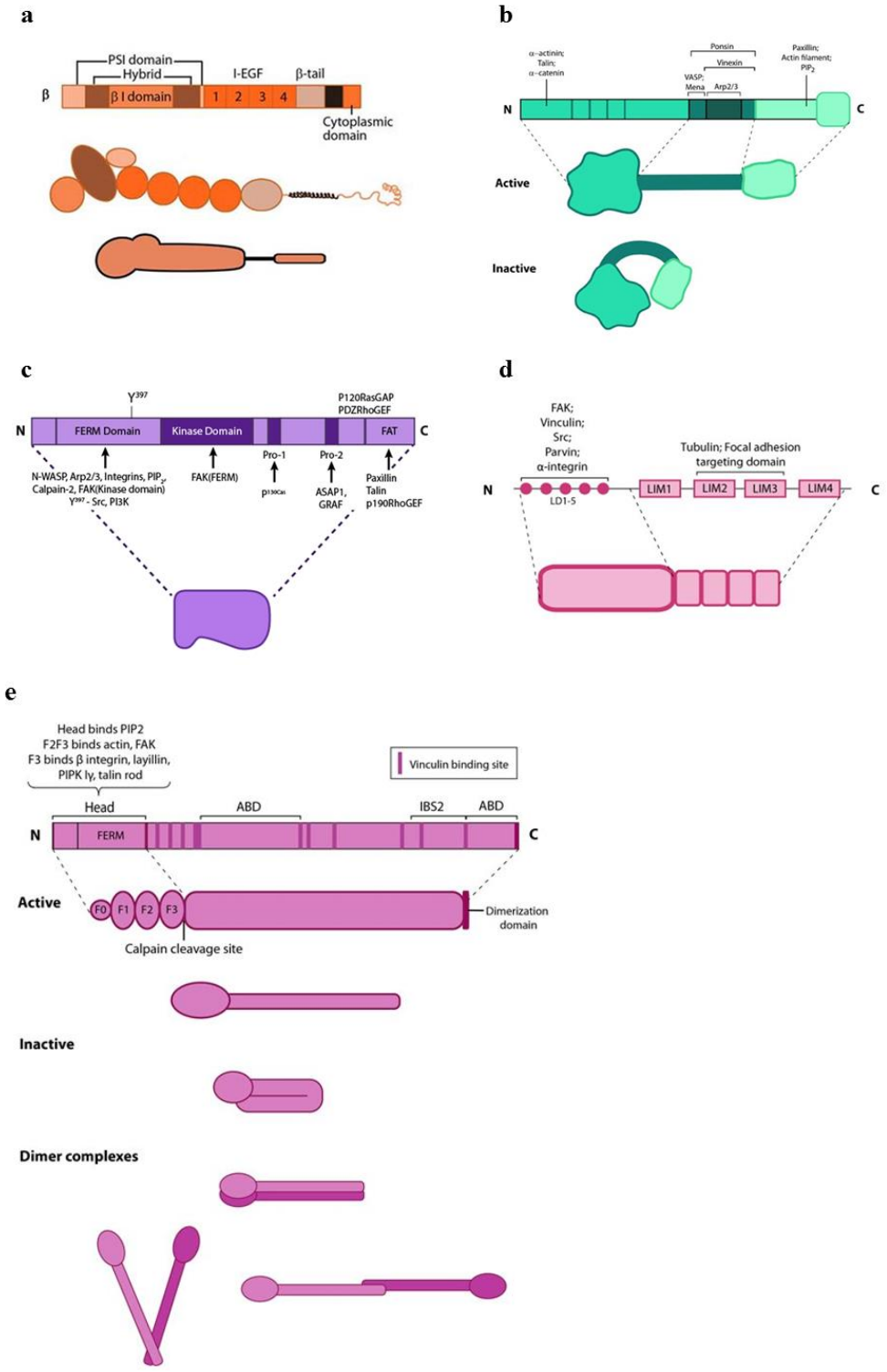

Figure 5: *Focal Adhesion point proteins; (a)Integrin, (b)Vinculin, (c)Focal Adhesion Kinase, (d)Paxilin and (e)Talin structures*

1.2.2 Stress fibers

As already mentioned in paragraph 1.2, actin filaments are the most important components of the cell cytoskeleton. These filaments are semi-flexible polymers formed by G-actin which can give rise to several structures such as parallel bundles, anti-parallel contractile structures, branched and crosslinked networks. The organization of actin filaments into two chains intertwined assemble what are called the F-actin chains. When the cells is subjected to same stress, these chains super-organize to form stress fibers. The stress fibers (SFs) are filamentous actin (F-actin) bundles, assembled by α-actinin, myosin II and other binding proteins. Usually, these are associated to FAs at one or both extremities [20]. There are different types of stress fibers: ventral stress fibers, dorsal stress fibers, transverse actin arcs and perinuclear actin fibers (Fig. 6).

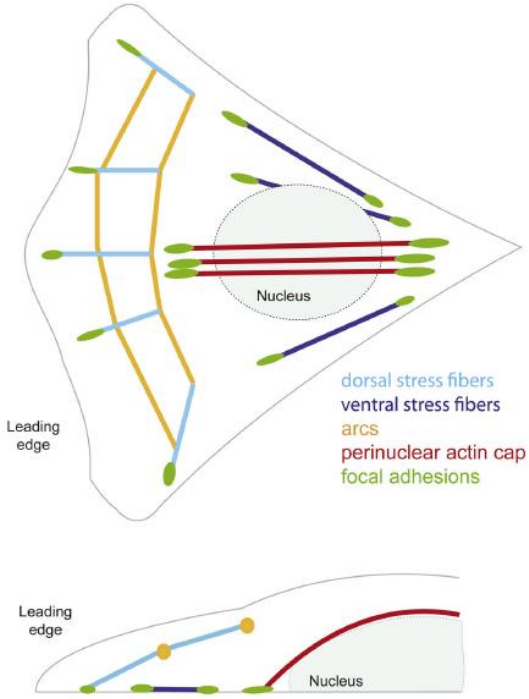

Figure 6: *Different types of stress fibers.* [20]

Ventral stress fibers lie at the basal side of cells and are anchored to each end through a FAs, while dorsal stress fibers develop on the dorsal side of cells and are anchored through a FAs only to one of its end. Transverse actin arcs are linked to dorsal fibers, run parallel to the leading migratory edge and are not anchored to FAs [32]. Perinuclear actin fibers (or perinuclear actin

cap) consist of α-actinin and myosin II organized in parallel bundles along the longer axis of the cell and extended to cell edges. It has been shown that the perinuclear actin fibers are associated with a structure on the nucleus membrane called Linker of the nucleoskeleton and the cytoskeleton complex (LINC) [33] (Fig. 7) .

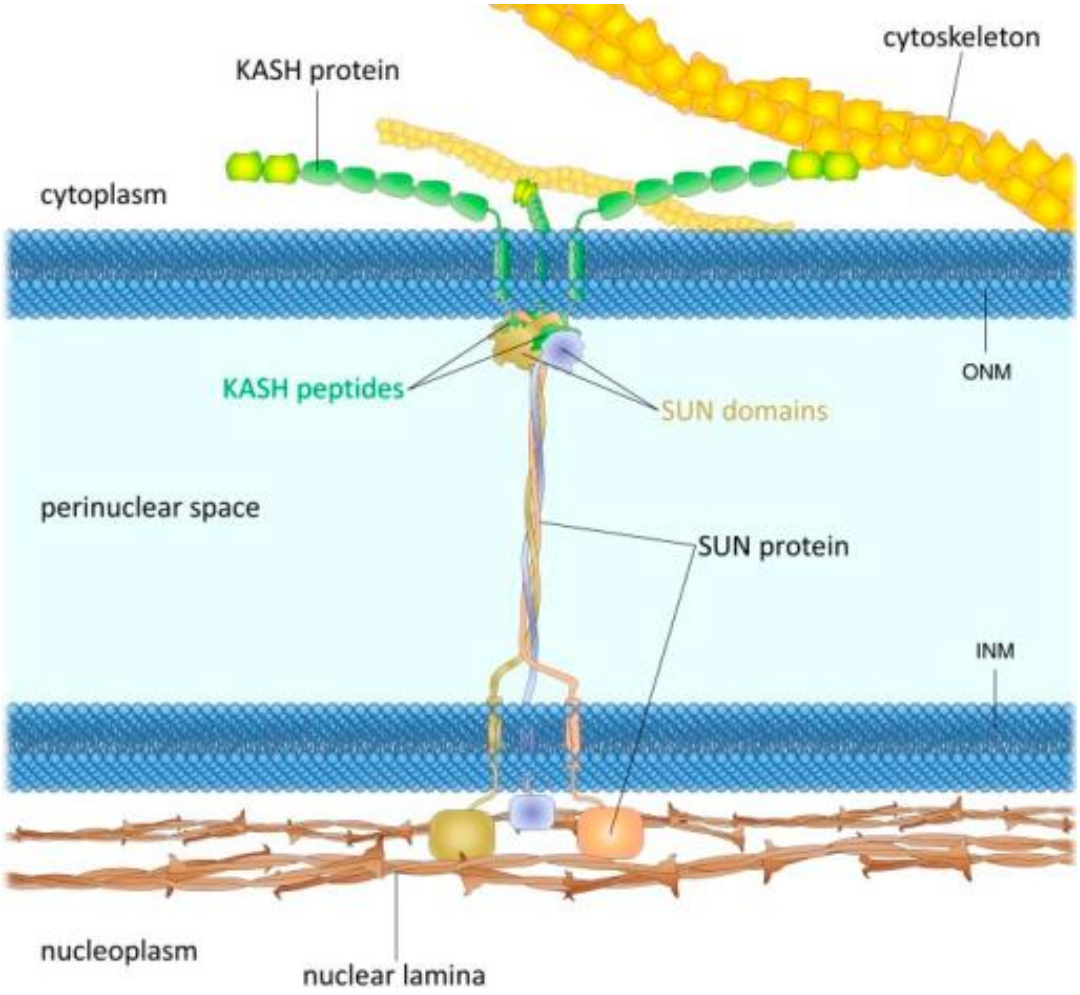

Figure 7: *Linker of the nucleoskeleton and the cytoskeleton complex*

These linking determine a specific nuclear shape, are involved in cell migration and affect the cell morphology. Therefore, these fiber subtypes are the only ones that connect the ECM with nucleus through the LINC complex. Stress fibers mostly provide the energy necessary for the movement and define the migration direction [34]. It has been discover that solitary migrating mesenchymal cells have a polarized shape with two distinct morphological and functional parts: an outward-curved (convex) shape at the protruding leading edge and an inward-curved

(concave) shape both laterally and posteriorly [20,35]. Furthermore, Hakkinen K. M. et al. have seen that in migrating mesenchymal cells stress fibers are less abundant, thinner and located predominantly at cellular periphery [36]. On the other hand, cortical actin filaments are located beneath the inner face of the cell membrane and give the cortex the contractile strength through myosin. Cortical actin is mostly responsible for the cell shape changes during migration. It seems that polymerization of cortical actin favours cell deformation in cell motility [37]. In cancerous cells, there are both a re-arrangement of actin filaments (such as stress fibers) and changes in actin gene expression (such as cortical actin filaments). High expression of actin and an abundant presence of stress fibers have been demonstrated in some non-malignant cells. On the contrary, malignant cells show low expression of actin and few stress fibers. Therefore, the deformability of cancer cells can be mainly related to these two actin filament types. Integrity of the actin cytoskeleton and the amount of stress fibers play an important role in the activation and nuclear translocation of YAP-TAZ complex. However, regulation of YAP-TAZ is unrelated to the ratio between the free G-actin and F-actin. For example, it has been noted that sometimes rounded cells have higher amount of F-actin than spread cells and *viceversa* [8,38].

1.2.3 Nucleus

In conclusion, we are going to discuss the last structural element of the cell affecting mechanobiology, the nucleus. Cell nucleus is 2-10 times stiffer than the cytoplasm and occupies the majority of the cell volume. The Nuclear Envelope (NE) defines the nucleus and it is a sub-domain of the endoplasmic reticulum (ER), composed of Outer Nuclear Membrane (ONM) which is in direct contact with cytoskeleton elements, and Inner Nuclear Membrane (INM). Nuclear pore complexes (NPC) connect the nucleus with cytoplasm (Fig. 8), allowing the exchange of several molecules. INM is in contact with nuclear lamina, composed of intermediate lamin filaments [39]. It has been shown that there are two lamin types: A-type lamins (lamin A and C are splice variants) and B-type lamins. These lamins have a different splicing isoforms of which different cell types have a characteristic expression pattern. In addition, these proteins confer shape, elasticity and stiffness to the NE and they are correlated with the mechanical stress of tissue. In particular, the A/C-type lamins is involved in the reaction to mechanical stress. In fact, the expression of these isoforms is low in soft tissues and high in stiff tissues [40]. It is also know that lamins tether the chromatin to the NE by contributing to the random chromatin

organization. Therefore, nuclear lamina can modulate gene expression directly through the interaction with transcription factor or indirectly by acting on chromatin organization, this regulate cellular proliferation, differentiation and apoptosis [39]. As anticipated, the NE contains also the LINC complex. This protein structure is formed by two protein domains called KASH and SUN respectively localized in ONM and INM (Fig. 7). Therefore, KASH proteins bind different cytoskeletal elements and SUN proteins interact with intra-nuclear elements. In fact, The SUN proteins are connected with A/C-type lamins and they are involved in the force transmission and in nuclear deformability in many pathologies [41].

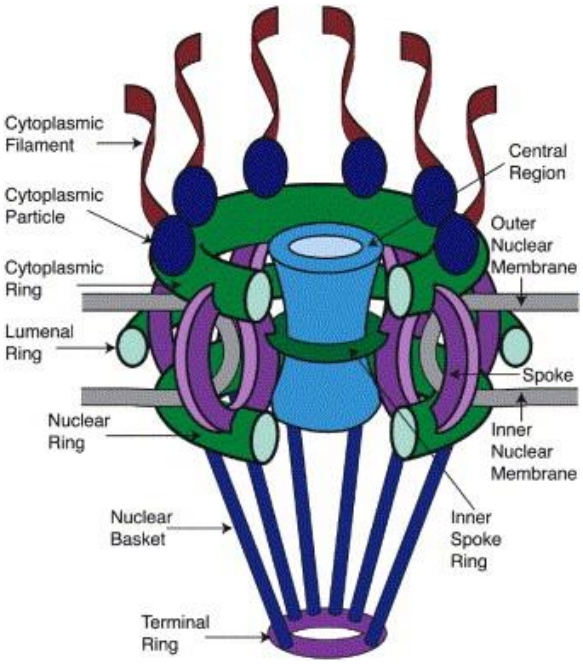

Figure 8: *Nuclear pore complex*

2. Mechanotransduction

As introduced in the previous section, mechanical stimuli exchanged between cells and between a cell and its extra-cellular environment activate specific biochemical and biological functions, which influence cell behavior [42]. This additional dimension of functional regulation is defined mechanotransduction. All the molecules described in section 1 cooperate in a complex network to perform cell mechanotransduction: in this way ECM stiffness signal is transmitted from the membrane through the cytoskeleton to the cell nucleus regulating gene expression by means of the action of specific effectors. In the mechanical regulation of tissue growth and organogenesis, of particular relevance is the Hippo network and its mechanosensing-driven transcription factor, YAP. In the next paragraph, we will review the recent literature on the Hippo Pathway, highlighting its role in mechanotransduction and tissue development.

2.1 Hippo Pathway and the mechanical stresses

Hippo pathways (Fig. 9) has been identified for the first time in *Drosophila melanogaster* as the controller of organ size through cell proliferation and apoptosis [43]. At the core of the mammalian hippo pathway are two kinases, namely MST and LATS, which control the activity of two closely related transcriptional co-activators, the Yes-associated protein YAP and the transcriptional co-activator TAZ through phosphorylation at a specific Serine residue in the amino-terminal region of YAP-TAZ [44]. The phosphorylation allows the formation of a protein complex which sequesters YAP-TAZ within the cytoplasm. If the LATS kinase is inhibited, then YAP-TAZ enter the cell nucleus and, after binding to specific transcription factors (TEADs), promote cell proliferation. The scientific community identified two different Hippo network signal ways: the “canonical Hippo pathway” which involves the direct regulation via LATS and and the “non-canonical Hippo pathway” where YAP-TAZ are regulated independently of the LATS kinase. This second pathway is specifically involved in mechanotransduction, and has not been completely understood yet. Hereafter we describe the two pathways more in detail.

Canonical Hippo pathway (Fig. 9)) is an evolutionally conserved signal cascade [45]. The activation of this pathway can start in two ways, through Serine/threonine-protein kinase (TAOK1/2/3) that phosphorylate actives mammalian Ste20-like kinases 1\2 (MST1/2), or through the direct dimerization of MST1/2 [46]. Following, MST1/2 activates the phosphorylation of two

scaffold proteins, Salvador homolog 1 (SAV1) and MOB kinase activator 1A (MOB1A/B) that are responsible of the recruitment and phosphorylation of large tumor suppressor 1\2 (LATS1/2). However, Yin F. *et al*. have seen that also the Neurofibronina2/Merlin (NF2/Merlin) have a most important role because they can directly interact with LATS1/2 by facilitating LATS1/2 phosphorylation by the MST1/2-SAV1 complex [47]. LATS1/2 phosphorylation inactivates the YAP-TAZ complex. Inactivation of YAP-TAZ is due to it binding with 14-3-3 protein by causing of YAP-TAZ cytoplasmic sequestration by resulting ubiquitination and degradation by the proteasome [48].

- ***Non-canonical Hippo pathway*** (Fig. 9) is involved in mechanotransduction response although the precise mechanism of action is not completely understood. Variations of ECM mechanical properties determine the canonical Hippo pathway inactivation due to the destabilization of the actin cytoskeleton integrity [44]. This reduces its downstream kinase-mediated YAP phosphorylation [49]. This reduces its downstream kinase-mediated YAP phosphorylation. Therefore, YAP moves in the nucleus and binds TEAD/TEF-family transcription factor by activating transcription of target gene involved in proliferation and conditions of stress as ANKRD1, CTGF, CYR61 [50]. It has been shown that this phenomenon is determined by the polymerization and depolarization of F-actin which it is regulated by Rho GTPase [45,51] (described with more details in the next paragraph). Therefore, the Rho GTPase activation determines a cytoskeleton modification which, not yet entirely clear whether through a direct or indirect effect of LATS1/2, leads to the nuclear translocation of YAP-TAZ complex [45,52].

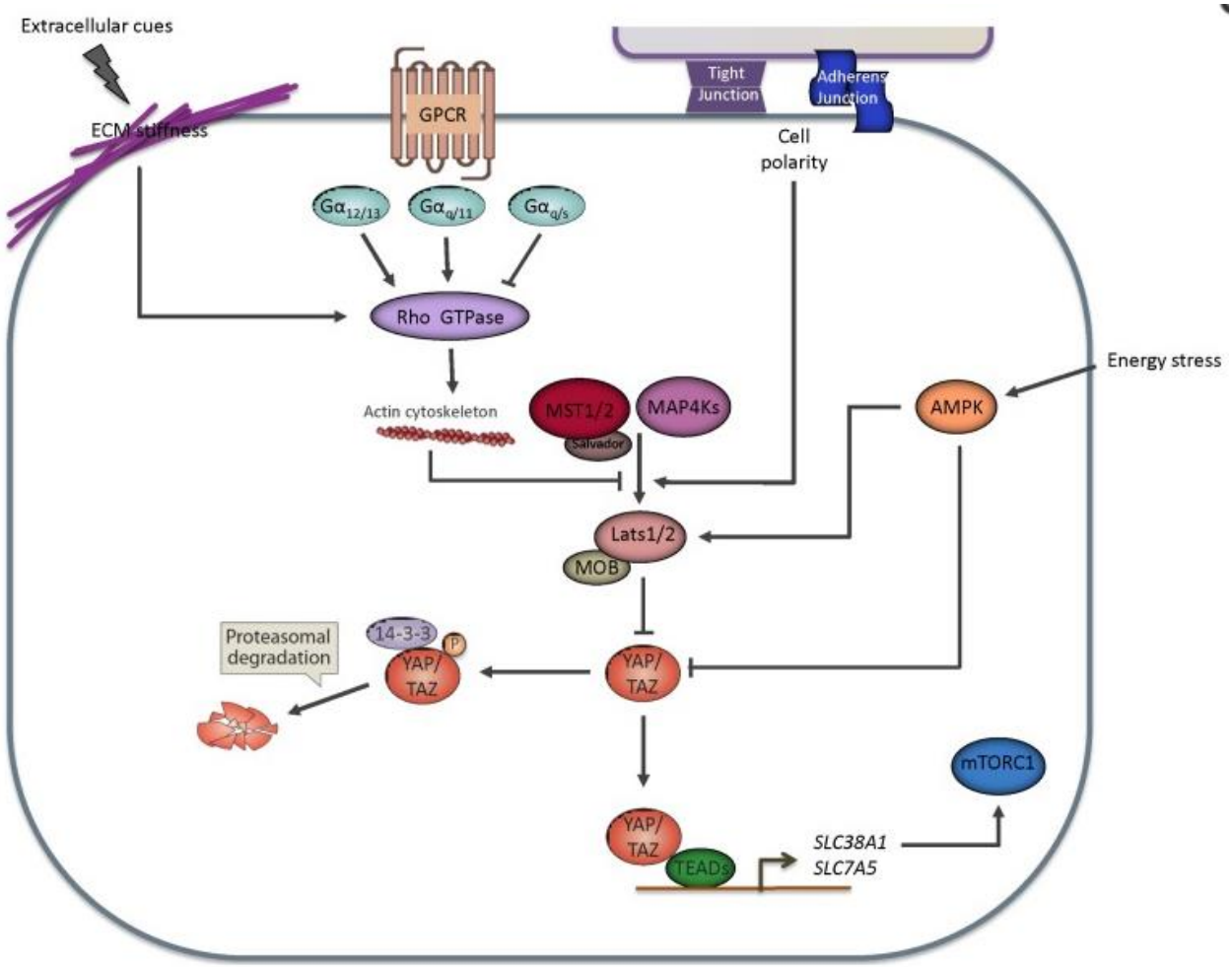

Figure 9: *Hippo pathway*[49]

2.1.1 The importance of the way of RHO GTPases

RHO GTPases are a family of proteins that are responsible of actin cytoskeleton rearrangement after the ECM mechanical properties variations. This family of proteins is formed by about 22 members with best-studied members being RhoA, Rac1 and Cdc42. Rac1 and Cdc42 are known to induce plasma membrane protrusions known as lamellipodia and filopodia by stimulating actin polymerization [53]. RhoA has been seen to be activated by mechanical stress, by self-inhibition, or also by its downstream effectors. It affects cyclic stretch-induced cells and stress fibers reorientation [54]. Rho GTPases are activated by Rho-guanine nucleotide exchange factor (Rho-GEFs) and inactivated by Rho GTPases activating proteins (Rho-GAPs) through the conversion of Rho GTPases from GDP-bound forms to GTP-bound forms and conversely [55]. However, there are different Rho-GEFs and Rho-GAPs which regulate the spatial and temporal control of a variety of actin cytoskeletal structures through Rho family members by determining a different cell response [56].

2.1.2 Role of Yap-Taz in the cell fate

The transcriptional co-activators YAP-TAZ the downstream effectors of the Hippo pathway, and are responsible of the biomechanical answer to cell shape and ECM elasticity. The complex is involved in the regulation of stem cell function, malignant transformation and cell fate determination. It has been shown that when the cells are grown on a stiffer matrix, the YAP-TAZ complex is localized in the nucleus and activates the transcription. Whereas, when the cells are grown on a softer substrate, YAP-TAZ is localized in the cytoplasm. In this case cells adopt a round shape and have lower adhesion with the substrate. Therefore, YAP-TAZ activity is regulated by cell stretching, spreading and cell size through the cytoskeleton rearrangement [57]. Recent studies have shown that YAP-TAZ plays a major role in the breast cancer development. Instead, it has been demonstrated that many types of cancer have higher microenvironment stiffness accompanied by an increased collagen deposition and the formation of linear patterns of collagen fibers than normal tissues [58]. These microenvironment variations determine the transcription of YAP-TAZ target genes which promotes tumorigenesis and the metastasis formation [59]. YAP-TAZ complex has a fundamental role also in the heart organ development, function, and regeneration. In particular in 2016, Ma H. and co-workers have studied the

mechanical interaction between porcine valve interstitial cells (pVICs)and different ECM in the onset of calcific aortic valve disease, correlating ECM stiffness to YAP-TAZ activation and translocation in VICs nuclei [8]. Also in the hVICs, ECM stiffness leads to high cytoskeleton tensioning which determines reversible high levels of YAP nuclear localization. We have studied the reversibility of the process treating hVICs with the pharmacological inhibitor of rho-associated protein kinase (ROCK) signaling pathways Y27632 and we evaluated the molecular and mechanical cell response. Surprisingly, we have found that the molecular phenomenon is completely reversed 24 hours after drug washout/removal while the mechanical response is completely reversed 48 hours after inhibitor washout (see Results, section 6).

3. Nanotechnology applications in mechanobiology

3.1 An overview of the principal techniques used in the study of the mechanical properties of cells and tissues

Cells are susceptible to different types of physical and chemical stimuli and these perturbations may alter their physical, biochemical and biological properties. Over the years, in order to study cellular and sub-cellular mechanical properties, it has been necessary to resort to nano-technological techniques such as the Atomic Force Microscopy (AFM), the optical tweezers and others (Fig. 10). In the last years, these techniques allowed to study how the biomechanics of the cell and its micro-environment varies [60] and how these variations are involved in different cellular processes and in the onset of different diseases [1,2].

- ***Optical Tweezers*** (Fig. 10a) use as probes glass particles moved by focusing on them a laser beam to a diffraction-limited point by means of a high numerical aperture microscope objective. These dielectric particles may have dimensions ranging from 20 nm to several micrometers. Optical tweezers use a highly-focused laser beam to provide an attractive or repulsive force (typically on the order of pico-newton), depending on the refractive index mismatch between the immersion medium and the probe, to physically hold and move microscopic dielectric objects to punch, press and pinch microscopic objects in a similar way tweezers are doing in the macroscopic world. Optical tweezers are able to apply forces in the range from 0.1 to 100 pN [61] and have been particularly successful in studying a variety of biological systems in recent years [62]. In cell stiffness characterization, the spherical probe, usually made by glass, is positioned on the top of the cell and the piezoelectric stage holding the sample moves vertically in order to obtain the indentation. Displacement-indentation curves are subsequently used to determine the mechanical properties of the measured sample.
- ***Micropipette aspiration*** (Fig. 10b) uses a set of micromanipulators to move in the three dimensions a glass capillary micropipette. In this framework, a vacuum generator is used to apply a suction negative pressure on the micropipette final aperture in order to such part of the cell under investigation. An optical microscope is used to evaluate the amount/portion of cell sucked by the pipette acquiring an optical image [63]. This system

evaluates the mechanical properties data of the single cells by evaluating the cell deformation after the pressure suction [64].

- ***Microfluidic device*** (Fig. 10d) are usually constituted by a micrometrical chamber that allows to study cells in physiological condition mimicking their in vivo environment when a (usually) shear force is applied to the cells. However, many different device configurations were developed in order to study the biomechanical and/or biochemical properties of cells. In particular, the biomechanical flow cytometry is a common system to study cell mechanical properties. This device is constituted by narrow microfluidic channels hosting sample cells in which the cell solution is pumped. Subsequently, changes in cell size due to shear-induced deformation are recorded [65] together with the transit time of the cells inside the channels [66].
- ***Magnetic nanoparticle stimuli*** (Fig. 10c) is an original method similar, in some way, to the optical tweezer approach: magnetic fields are used to press magnetic nano- or micro-particles on the cell membrane evaluating, in this way, their mechanical properties as expression of displacement-indentation plots. In some experimental procedure, the magnetic nanoparticles are internalized by the cells and moved in an oscillatory fashion by means of a micro-magnetic culturing slide [67].
- ***Atomic Force microscopy*** (Fig. 10e) is a scanning probe microscopy relying on mechanically scanning a surface with a nanometric sharp probe and providing a three-dimensional space reconstruction of the entire sample. However, this technic could be used not only for surface reconstruction purposes but to evaluate the cell or tissue mechanical properties too via force-indentation curves. Briefly the piezoelectric scanner moves the tip until it interacts with the sample surface and indents it by elastic deformation. From the resulting force-displacement curve, the elastic modulus of the portion of sample below the tip is calculated [68].

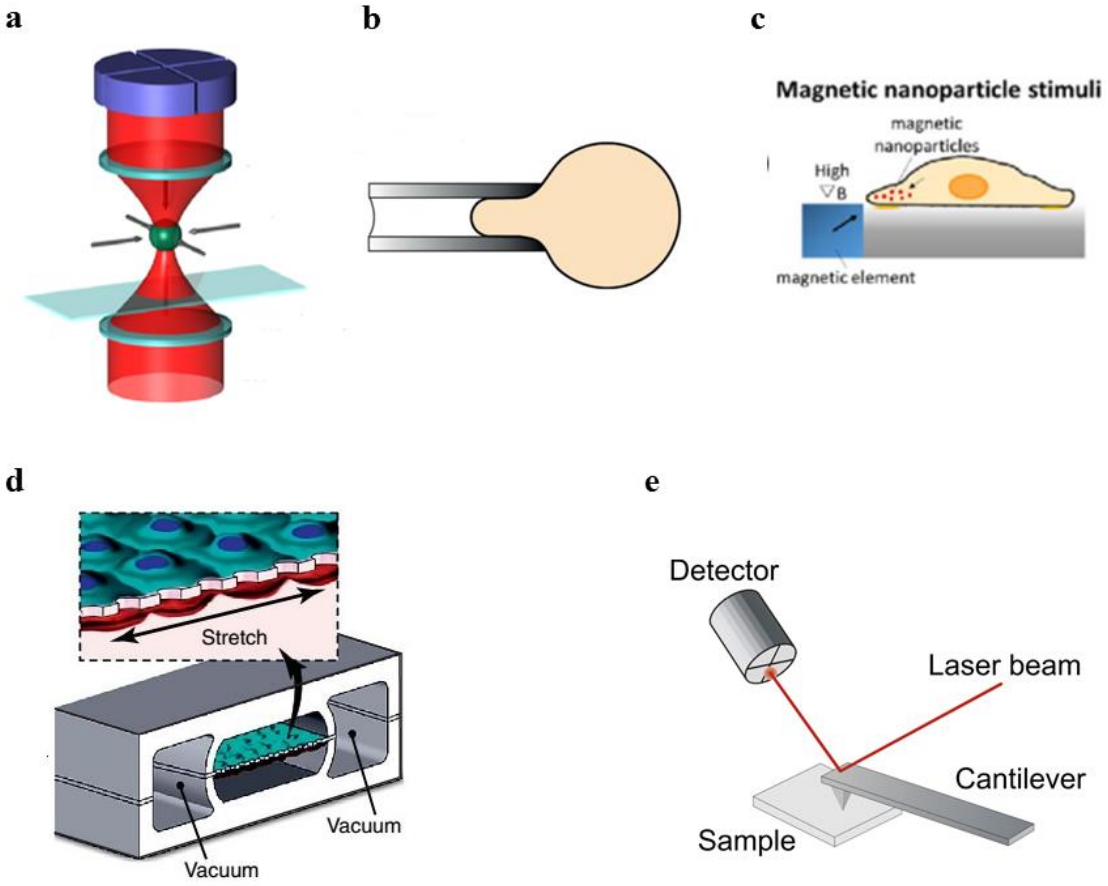

Figure 10: *An example of different approaches usable to determine mechanical properties of cells or of their compartments (e.g. nuclei or processes): (a)Optical Tweezers; (b)Micropipette aspiration; (c)Magnetic nanoparticle stimuli; (d)Microfluidic device; (e)Atomic Force Microscopy*[69–71]

4 The Atomic Force Microscopy

The atomic force microscope (AFM, in short) belongs to the family of scanning probe microscopes (SPMs) and is characterized by the use of a nanometric sharp probe to investigate morphological properties of surfaces with sub-nanometer resolution. In general, the AFM is characterized by the use of an ultra-sharp tip mounted at the end of a flexible micro-cantilever made by silicon or silicon nitride. The relative scanning motion of the cantilever above the surface is possible thanks to one or more piezoelectric crystal, allowing sub-nanometric displacement control and resolution. These piezoelectric scanners move the tip above the sample surface (or, depending on instrument configuration, the substrate below the tip, that stays stationary) by following a raster-scan motion: a sequence of fast horizontal lines alternated by slow steps in the vertical direction. Tip deflection is recorded through a laser that is reflected by the back of the cantilever onto a four-quadrants photodiode detector. When the tip interacts with the sample surface the cantilever deflects and the laser spot changes position on the photodiode. Every nanometrical deflection of the cantilever is converted by an optical lever path in a large movement of the laser spot on the four quadrants photodiode detector allowing an easy and fast determination of the amount of cantilever deflection. Hereafter the deflection induced by the tip-surface interactive forces [72], is converted into an electrical signal whose variation is proportional to the variation of sample surface height (Figure 11).

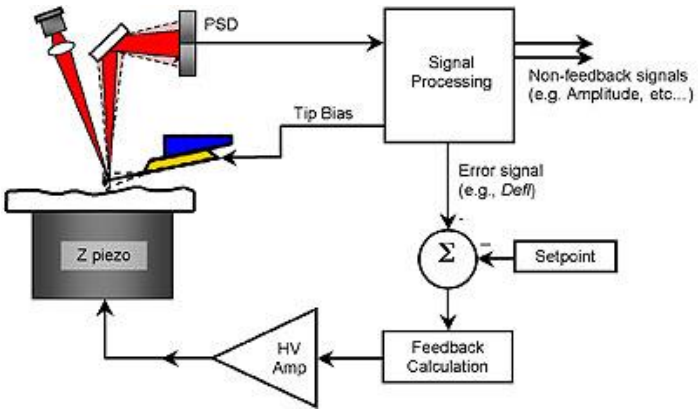

Figure 11: *Atomic Force Microscopy working principle* [73]

In contact-mode modality (see the following paragraph about AFM working modalities for details), thanks to a force feedback loop, the AFM tip applies during its canning a constant force

to the sample. We can determine the value of the exert force by knowing the cantilever stiffness (k) and applying the Hooke's law: in this way, we can use this linear relationship to evaluate the applied force (F) as function of cantilever deflection:

$$F = -kx \qquad (4.1)$$

where F is usually a value between 10 pN and 1 μN, the elastic modulus of the cantilever k is about 0.01÷50 nN/nm and the displacement z is in the nm to μm range.

The imaging resolution of AFM technique depends, among other parameters, by tip shape and its cantilever elastic characteristic. Regarding possible cantilevers geometries, they can be rectangular or triangular (Fig. 12a) with a length between 2 and 200 μm and thickness usually above 1 μm, resulting in a spring constant in the range of tens of pN/nm to tens of nN/nm [74]. Whereas, the choice of the appropriate AFM tip is determined by the sample morphology, stiffness and kind of characterization we would to carry on (e.g., surface reconstruction, force mapping, electric measurements, etc. etc.). As a general rule, for contact-mode imaging purposes on soft materials (e.g., cells), soft or ultra-soft triangular or rectangular cantilevers are used. Instead, for nano-indentation experiments on cells, cantilever stiffness has to be choose as function of tip shape in order to apply to the cell a sufficed load to test it but not so large to damage the cell itself. In this context, I would like to anticipate that cantilever endowed with different shapes of the probes at the end, such as flat-punch, spherical tip, pyramid tip and conical tip (Fig. 12b-e) could be used. Each of these tips has its own advantages and disadvantages: the flat-ended cylindrical punch is preferred for a very soft and fragile cellular or subcellular structure and its data interpretation is very easy because the contact area is a constant. Unfortunately, punch edges could result in substrate damage if medium to high forces are applied [75]. The spherical tip is used as well for soft and delicate samples as in the punch cylinder case, but it is particularly useful if the risk of sample damaging is high. In fact, using this penetrator, the contact area is not constant but function of the applied force. Consequently, sample is subjected to a stress where the effective strain is connected to the ratio between the contact radius and the sphere radius [76]. Finally, the very sharp pyramidal tip is employed to study extra-small features thanks to its low contact surface (few square nanometers) but may easily damage the

sample due to enormous pressure exerted by the tip that reduce the control we have on its effective value [77].

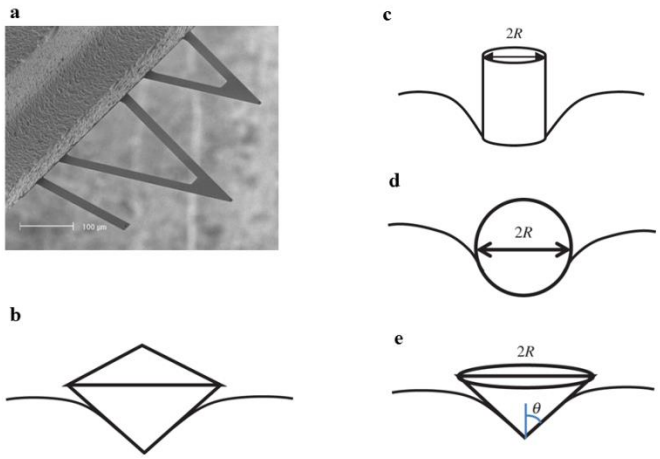

Figure 12: *(a)rectangular and triangular cantilever;(b) pyramidal tip;(c) flat-punch; (d) spherical tip;(e) conical tip.*

4.1 AFM working modalities

AFM working modalities are strictly correlated to the interaction force region where the tip/sample interaction fall. This interaction could be repulsive in short distance (< 1 nm tip-sample separation) or attractive over long distances (Van der Waals force, tip/sample distance larger than 1 nm but lower than 100 nm). As consequence of that three operation modes could be defined for AFM: if the repulsive force is predominant, AFM work in the so-called *contact mode*. During the contact mode AFM tip is in constant and gentle contact with the surface of the sample. In this regime, a small variation in the distance causes a steep variation in the attractive potential and the repulsive forces cause a negative deflection of the cantilever. In the AFM contact imaging mode, the measurement of the cantilever deflection, and so, the applied force, is given as input to a feedback circuit, which point-by-point corrects the cantilever bending by moving the tip closer or farther to the surface maintaining it fixed at a certain set-point (the force value defined before starting the AFM measurement) all along the time the tip is scanning the sample (*force-constant contact mode measurement*) [78]. In this regime, the tip is in direct physical contact with the sample surface and the amount of the exerted force is function of the force set-point set and of the shape (aka the contact area) of the used tip. If, instead, the attractive force is prevalent and the tip never physically touch the sample, the mode is called *not contact*

mode. In this method, the probe is made oscillating near to its resonance frequency at an amplitude ranging from a few nanometers to a few micrometers. The variation of the amplitude of oscillation when the excitation frequency is maintained constant could be only due to a perturbation connected to the establishment of a tip surface interaction. A feedback-loop able move the tip closer or farther is used to maintain constant the amplitude during tip scanning enabling, in this way, to obtain the topographic image of the sample [78]. The third AFM mode of operation is the so-called *intermittent contact mode* where both attractive and repulsive force are involved. In this case during the scanning it is possible to record and maintain constant the cantilever oscillation amplitude as in *no-contact mode*. Anyhow, in this modality, the tip touches intermittently the surface, falling "instantaneously" in the force repulsion regime and, as a consequence of this, the resolution this modality gives is intermediate to the resolution achievable by *contact* and *no-contact modes* [79] (Fig. 13).

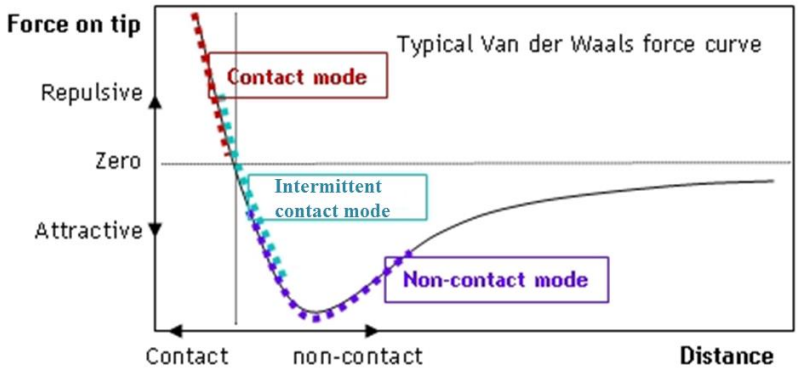

Figure 13: *AFM force-distance curve. In this curve, it is represented the role of different interaction between the tip and the sample. The tip begins to feel attractive long range forces which is non-contact AFM region, until tip and surface electron orbitals are so close to start exerting repulsive forces called contact mode AFM region. Between these two regimes lies the intermittent-contact region.*

4.2 AFM force spectroscopy

As previously stated, the AFM has been initially used in the biological research field just for three-dimensional image acquisition of living biological samples [74]. Following, the microscope has been extended in its use to evaluate many other biological parameters, such as interaction forces between single molecules, cell adhesion forces and, pf course, sample mechanical properties. Thanks to AFM ability to measure the elastic properties of biological samples in

physiological conditions, its use is increasingly growing pointing out, in particular, how the mechanical properties of cells are extremely important to study many pathological conditions [80]. Therefore, many research groups and companies are making efforts to develop innovative diagnostic tools giving the possibility to perform AFM force characterization of cellular/tissutal samples directly in hospitals for early stage disease diagnosis [81,82].

4.2.1 Single cell AFM force spectroscopy

In the last few years, many studies have focused on the study of single cells mechanical properties or on the study of factors that are involved in the variation of cells mechanical properties. One of the most important of such parameters influencing elasticity of cells is the stiffness of the extracellular matrix (ECM) [2]. Many studies have demonstrated that the ECM mechanical properties are extremely important in cell development [83,84], differentiation and in the speed of drug delivery [85]. AFM was used in this contest to characterized both mechanical properties of the ECM and of the cells. Interestingly, AFM could be used as well to evaluate the effect of specific drugs, due to the fact many of them interact with cell actin and microtubules structure or pathway determining variations in the cell elastic modulus [86].

AFM indentation data demonstrated that in many pathologies such as the anemia, diabetes, cardiomyopathies, Parkinson's and Alzheimer's diseases, cancer and many others, the mechanical properties of affected cells are perturbed resulting in a characteristic fingerprint for these diseases [82]. For example, Wu X. and coworkers, in 2016, used the AFM to study the mechanical properties of neurons in the mice model of chronic epilepsy [87]. They demonstrated that an increase in neuronal elasticity could be associable to pathology progression [87]. However, cancer is so far the most studied disease by means of AFM, due to the fact the high versatility of this microscopy technique allows to study cell migration, morphology and stiffness, all parameters of great relevance for cancer studies [88]. In particular, breast cancer is the most studied due to the social impact among female population. The AFM evaluation of cell elastic modulus in different types of breast cancer has made it possible to point out that the most aggressive tumor cell phenotypes are significantly softer than healthy cells, allowing cell sorting based of cell mechanoresponse [89,90]. In another study they shown that the Young's modulus of breast cancer cells is proportional to the migration capability of such cells [91]. Nevertheless, there are as well evidences, such as in the case of Maherally Z. and co-workers' studies,

demonstrating that, in the case of low aggressive tumors, there is any correlation between the reduced cell stiffness and their invasive potential [91].

4.2.2 AFM force spectroscopy on tissutal slides

In the last decade, atomic force microscopy has been used not only to evaluate the mechanical properties of individual cells, but also to carry out tissue force maps. Although the number of articles on this topic is limited, there is an increasing interest in developing new evaluation procedures able to detect chemical or physiological changes at very early stages of disease progression, meaning well before the pathological fingerprint become histologically visible [92]. The first tissues analyzed by AFM were breast cancer slices from Human. In fact, Plodinec M. and co-worker have exploited high-resolution stiffness mapping of tissue slices in order to distinguish cells and ECM on the base of their mechanical properties and, moreover, they tried to study cell stiffness as function of tumor progression. Their results have confirmed the pivoting hypothesis that metastatic cells must be very soft to easily migrate into and through the surrounding tissues [81]. Another research group carried out a classification of breast cancer aggressivity by correlating force maps with histological staining of typical cancer markers such as Luminal A, Luminal B and Her2 [93]. Moreover, the AFM could be used as well to measure the brain tissue stiffness. Elkin B. S. *et al*. have studied how the rigidity of hippocampal and cortex tissue changes with aging on rat brain tissue slices. They have found that with aging the stiffness of the tissue significantly increases [94]. Following the work of Elkin B. S. and coworkers, other groups analyzed the hippocampal tissue but with a higher resolution in force map reconstruction: thanks to the higher spatial resolution of AFM, they could identify regions in the hippocampus which are characterized by different stiffness; these areas have been traced back to different levels of cell maturation [95]. It was seen that there is a strong correlation between the cell distributions and axon orientations and tissue stiffness in the spinal cord tissue too [96]. AFM force mapping has allowed to demonstrate that the variation of grey matter pH is consistent with tissutal stiffness values [92]. Following, Franze K. *et al.* studied how elasticity of neocortex and spinal cord change over post-injury time by means of AFM. In their work they have clarified that the neuronal growth is regulated and guided by tissue paths characterized by a lower stiffness than the surrounding regions [97]. In parallel, Jorba I. *et al.* proved that the brain stiffness is influenced by ageing and chronic intermittent hypoxia [98]. With this very short review about the topic I would just stress about the fact tissue mechanical properties are extremely important in the

onset of many tissue organization and maturation, pathological development cellular migration. In particular, tissue stiffness and ECM structure seems interconnected entities able to mutually influence through their chemical and mechanical properties. In this framework, AFM micro-indentation analysis have shown that ECM stiffness increases after fibrosis in the lung and this data is confirmed by the lack of expression of cyclooxygenase-2 and synthesis of prostaglandin E_2 [99].

4.3 Evaluation of mechanical properties by AFM *via* force-distance curves

Different strategies could be followed to determine the mechanical properties of a sample taking advantage of AFM, anyhow the most common consists in the analysis of force-distance approach curves. These are derived indenting an AFM tip of specific shape (see previous paragraphs) into the sample surface recording the deformation of, and consequently the force applied by, the cantilever. Analyzing in detail what happens to the probe when it is advanced close to the sample, at a certain point the tip jumps into contact with the surface (Fig. 14). From this contact point, by pushing more the base of cantilever against the sample, the negative deflection of the cantilever increases proportionally to the applied contact force. The cantilever penetrates into the material more or less as function of material compliance and force *vs.* indentation data may be used to investigate the elastic properties of the sample itself, obtaining in this way the value of sample stiffness in terms of Young's modulus (see previous paragraphs). Reversely, an inverse curve can be obtained when the tip is progressively removed from sample surface until anymore in contact with it. This is called the retracting force-distance curve, and it is tremendously useful to study the presence of any adhesion forces between tip and surface.

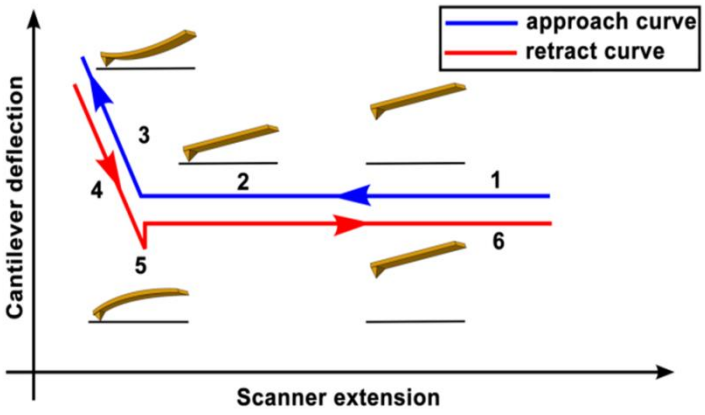

Figure 14: *Force curve: 1) there is not interaction between tip and sample and they are far; 2) the tip "jump to contact"; 3) the tip approaches with sample that leads to a positive deflection of the cantilever due to repulsive forces; 4) the tip moves toward the opposite direction and, at the beginning, the behavior is similar to that described for the approach; 5) the cantilever deflects negatively for the adhesion between tip and sample; 6) adhesion forces are overcome by cantilever restoring forces and the tip is detached from the sample*

The force curve is an x-y plot, in which the distance between the base of the AFM cantilever and the surface under investigation is reported in the x-axis for both the approach and retraction parts while in the y-axis the deflection of the cantilever (measured in mV) is reported. It is important to point out that:

(i) the variation in the distance between the base of the AFM cantilever and the surface is similar to the variation in the distance between tip apex and the surface until contact point is reached. At this point, if the material has infinite rigidity, the tip surface distance will be zero while the distance between the base of the AFM cantilever and the surface could be further reduced and will result only in cantilever deformation (so, increase in applied force).

(ii) If the material is soft, the tip could penetrate into the surface and the deflection of the cantilever due to the further reduction of the distance between the base of the AFM cantilever and the surface has to be corrected by the distance apex tip penetrate into the material. The entity of this penetration is inverse function of the stiffness of the sample. The applied force is always given by the cantilever deflection but the amount of indentation has to be calculated. In this way, the deflection can give a direct measure of the force exerted by the tip on the sample [68].

In general, qualitatively speaking, if the slope of the curve is linear and at a slope of about 45°, this is an indication of a sample extremely hard and no indentation took place (Fig. 15a). Otherwise, when the sample is soft, the shape of the force-distance curve is more parabolic than the previous one with a slope below 45° [74] (Fig. 15b).

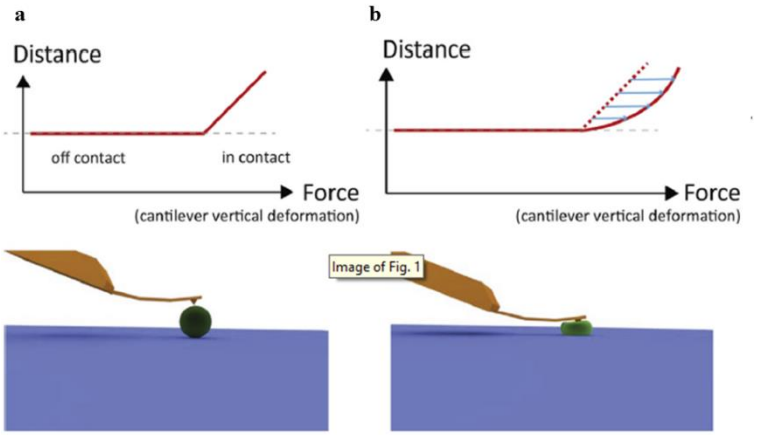

Figure 15: *Force-distance approach curves: (a)There is not deformation of the stiff sample; (b)Deformation of the soft sample* [74].

4.3.1 Force curve analysis

In order to effectively calculate in a quantitative way sample's Young's modulus, it is mandatory to proceed with the calibration of cantilever elastic modulus in order to make usable the data coming out from force curve *via* a force curve fitting procedure. Therefore, to calibrate the measurement we have to evaluate the optical sensitivity of the AFM system used and the cantilever spring constant must be calculated. The sensitivity value (S, mV/nm) is obtained by measuring the force-distance curve between a cantilever and a reference bare hard surface (considered not deformable). The repulsive contact region is linear for the interaction between a tip and a hard substrate, therefore the software can determine the converting factor to transform a deflection value expressed in millivolts (mV) into a usable deflection value x expressed in nanometers (nm):

$$x = \frac{V}{S} \tag{4.2}$$

When all the force curves performed on the sample of interest are done, this value will be used to calibrate the applied forces, in fact, cantilever deflection could be now expressed as a distance x

(in nanometers) and converted this into a quantitative value of force F by multiplying it by the cantilever spring constant (*k*, nN/nm) taking advantage of the Hooke's law (eq. 4.1):

$$F = kx \tag{4.3}$$

This force is clearly increasing as much as the cantilever is pushed towards the sample surface. The normal spring constant of a rectangular AFM cantilever can be determined using the Sader method [100]. Summarizing, only after having performed such calculations, it is possible to convert the deflection-displacement curve obtained by the AFM in a force-indentation curve analyzable by the software via opportune fitting model procedures (see next paragraph) [68,74].

Young's modulus numerical value estimation could be obtained by fitting force-indentation curves with opportune numerical models. Among all, fitting models such as Hertzian, Sneddon, Johnson–Kendall–Roberts (JKR) and Derjaguin–Muller–Toporov (DMT) are the most used and diffuse in cell biomechanic research (see a detail description later in this chapter). All models take into account the geometry of the AFM tip [74]. Therefore, in all our experiments, the Hertzian model was used to determine cell stiffness in terms of Young's modulus (E) [101].

4.3.2 Fitting models

As I have already introduced in the previous paragraph, different fitting models are available to researchers to analyze force spectroscopy data extrapolating, in this way, reliable information about cell stiffness. Among all these models, each of which is characterized by well-defined application conditions, limits and advantages, the most used (and accepted) by the biomechanical research community is the Hertz model (or Hertzian) applied taking into account all the necessary experimental conditions concerning, for example, the probe shape and the minimum thickness the sample under investigation has to have. In fact, nowadays, the Hertz model is the analytical approach to treat force-displacement data in the majority of indentation experiments involving cells or microscopic and macroscopic biomolecules. The Hertz formalism is founded on the theory of linear elasticity and must satisfy a Hookean relationship (eq. 4.1). This describes the elastic deformation of two sphere, where the relation between the applied force (F) and the resulting indentation is:

$$F = \frac{4ER^{\frac{1}{2}}}{3} \frac{\delta^{\frac{3}{2}}}{(1-\mu^2)} \quad (4.4)$$

where E is Young's modulus, μ is the Poisson's ratio of the indented material that is ranging from 0 to 0.5, in particular the larger value is used for living cells, and R is the radius of the rigid indenter. δ determines the contact radius (α) through the following relation [102]:

$$\alpha = R^{\frac{1}{2}}\delta^{\frac{1}{2}} \quad (4.5)$$

However, the Hertz model becomes invalid when the indentation depth is comparable to the cell dimension [103].

An alternative fitting model is the Sneddon's model. It considers the interaction between a conical or paraboloidal tip and a flat sample. The equation which calculates the indentation force for a conical tip is:

$$F = \frac{2\tan(\alpha)}{\pi} E\delta^2 \quad (4.6)$$

Whereas for the paraboloid is:

$$F = \frac{4\sqrt{R}}{3} E\delta^{1.5} \quad (4.7)$$

The variables are the same of the Hertz model (4.5) [74].

In JKR and DMT models the adhesion force between two (micro)spherical bodies is considered as well. In addition to that, JKR takes into account adhesive force inside the area of contact and is favored for large and compliant spheres (μ>5).

$$F = \frac{9}{4} E\sqrt{R}\delta^{\frac{3}{2}}\Delta\gamma\pi \quad (4.8)$$

On the other hand, DMT model evaluates the adhesive forces outside the contact area and holds for small and stiffer spheres (μ<0.1).

$$F = \frac{4}{3} E\sqrt{R}\delta^{\frac{3}{2}} - 2\pi R\gamma \quad (4.9)$$

Also for this two models, the variables are similar to Hertz model (4.5) expect for γ that it is the work of adhesion [104,105].

4.3.3 Finite element method

All methods explained until now hypothesize that all, the sample, the tip and the substrate under investigation are homogenous bodies with a well determined geometry. This hypothesis is far from reality, in particular when the analysis has to be conduct on living systems, as cells. Some authors have used finite element modeling to overcome these problems. Finite element modeling (FEM) converts a complex geometry into a finite number of elements with simple geometries all describable with and interconnected by simple mathematical relations. To do this, a system of equations is generated and solved for each element that is assembled to ensure continuity of the entire system. Data produces by FEM are complex and require heavy computational power to be carried on in a reasonable time-frame. Many different software packages are available as commercial software (e.g., COMSOL Multiphysics, Abaqus, etc.) or freeware. Anyhow, their complexity and the necessity to perfectly set the contour conditions of the used mathematical model make them a tool not generally used and diffused among AFM users studying cellular mechanobiology [74,106].

5 Relevance of mechanobiology and mechanotransduction in clinical research

Mechanobiology and mechanotransduction are become increasingly important research topics of the clinical scientific community due to evidences of their involvement in basically all the biological cell functions and regulations, from the development of a tissue to the onset of a disease [1,16]. For this reason, clinical interest in the study of biophysical processes is rising and is focusing on developing new (nano-technologic) tools able to improve common diagnostic techniques. In this part of my thesis I am going to present three examples of cellular systems in which biomechanics and mechanotransduction play a very relevant role.

5.1 Mechanobiology in the onset of calcific aortic valve disease

5.1.1 Aortic valve structure

The aortic valve (AOV) is situated inside the aortic root, between left ventricle and ascending aorta. It consists of three leaflets called left coronary, right coronary and not-coronary. These three leaflets are supported by a ring-shaped fibrous structure that is connected with the heart muscle [107]. They are less than 1 mm thick in humans, but may vary from individual to individual [108]. Every leaflet is formed by three distinct layers called: *fibrosa*, *spongiosa* and *ventricularis*. These three layers have different and characteristic fibrous composition directly related to their function [109] (Fig. 16). *Fibrosa* is on the aortic side and is mainly formed by collagen type I and collagen type III. It acts as the main load-bearing layer. *Spongiosa* has the main function of lubricate the adjacent *fibrosa*. It is primarily composed by proteoglycans embedded by collagen fibers [109]. *Ventricularis* is instead located on the opposite ventricular side and composed of a mixed network of collagen and elastin fibers. Elastin is responsible to the minimization of systole and diastole associated stresses [110]. The aortic valve includes two main cellular components, deeply described in the next paragraphs, playing an important role in all cardiomyopathy. The first cellular component resides in the more external party of the leaflet, and cells composing it are named valvular endothelial cells (VECs) assemble as a monolayer and contribute to valve homeostasis and permeability [111]. The second component is located in the inner layers of the leaflet, and is composed by cells named valvular interstitial cells (VICs). This

heterogeneous cell population is mainly composed by fibroblasts cells (Fib), smooth muscle cells (SMc) and by a small percentage of myofibroblasts (Mfib) (<5%). In the onset of calcific aortic valve disease the myofibroblast subpopulation increases up to 30% and, subsequently, differentiate in osteoblasts-like cells [112]. These cells, in terms of an increase in number or, more important, in terms of an increase in their cellular stiffness, will be the cellular indicators of a pathological evolution (or progression) occurring in the tissue.

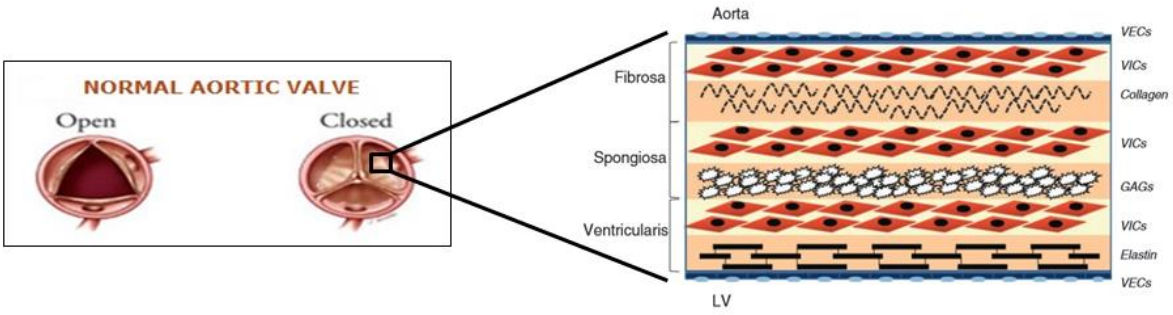

Figure 16: *Schematic representation of aortic valve leaflet structure*

5.1.2 The calcific aortic valve disease

The diseases affecting AOV are widely diffuse worldwide and the most common among them is the calcific aortic valve disease (CAVD), which could be considered the main cause of aortic stenosis [113]. This pathology could present in two forms: congenital disease or aging disease. In both cases CAVD is characterized by the thickening due to calcification of valve leaflets [114]. The starting process correlated to CAVD is the aortic stenosis, an abnormal narrowing of the valve diaphragm passage mainly due to the inflammation determined by the mechanical stress induced by the altered shear blood flow. This anomalous blood flow leads endothelial damage allowing the penetration of inflammatory cell infiltrates, lipoproteins and lipids [115]. This inflammation goes along with the phenotypic modification of the VICs, which are characterized by 5% of myofibroblasts population in an healthy valve, that undergo through an increase of myofibroblasts population to more than 30% in a no longer healthy valve [112]. Another characteristic feature of this disease is the significant change in the extracellular matrix (ECM) that appears to be not only the result of the dysfunction of the valve cells but also contributes to

the progression of the pathology altering the cellular and molecular signalling [112]. Both these factors determine the phenotypic differentiation of myofibroblast to osteoblast-like cells and the formation of calcium nodules inside the leaflet [116]. Therefore, it has been suggested that the mechanical heterogeneity of the tissue valve may affect the cellular sensitivity to pathological signals [117,118]. In VICs, isolated from porcine, it was also seen that the differentiation in myofibroblasts is induced by the transforming growth factor (TGF)-β1, but requires the presence of β-catenin, which increases its nuclear translocation proportionally to the rigidity of the ECM. Again, the critical role of cell and ECM stiffness is pointed out. It is also apparent that the increase in the stiffness of the substrate causes an increase in the global elastic modulus of the cells, which leads to a significant increase in expression of α-smooth muscle actin (α-SMA) in stress fibres [80]. In the ECM sustaining an healthy aortic valve, collagen fibres are well organized while in the onset of the disease this organization is partially lost [119,120]. This could explain the local variations in ECM mechanical properties associated to cell cultures developed on stiff substrates (e.g. glass) [121,122]. Other factors that determine the ECM mechanical variation by causing variations in VICs phenotype are stress relaxation and transvalvular pressure [123,124]. Based on observations on the role of collagen in the onset of the disease, Ma H. and co-workers demonstrated that variations in the matrix mechanical properties affect the phenotypic properties of VICs thought a YAP associated cascade signalling in porcine valvular interstitial cells (pVICs) [8,125]. As explained in Chapter 6 of this thesis work, I have found that the ECM mechanical properties affect the VICs phenotype thought a YAP signalling in both *in vitro* and *ex vivo* human model. In addition, I have identified a stiffness range for the substrate able to put cells in a state of quiescence where any pro-pathological drive took place. Thanks to this result I have been able to decouple the mechanical contribute from the substrate from the morphological contribute of the matrix identifying CNTs carpet as a nanostructured material that have a positive effect on VICs phenotype.

5.2 Mechanobiology in the cancer

5.2.1 Cancer

Cancer, being the second cause of death in worldwide, has attracted the attention of a large portion of biomedical research, mainly attempting to understand the disease very first seeding

conditions and, in parallel, to develop new tools able to reduce cancer progression [126]. Cancer is an extremely complex and multistep disease that during its progression transforms normal cells into their malignant derivatives. It not only determine a uncontrollable cell proliferation rate but it recruits also different cell types, such as endothelial cells, immune inflammatory cells or cancer associated fibroblasts, in order to facilitate tumorigenesis [127]. However in the onset of cancer disease, the cells obtain special properties like resistance to programmed cell death (PCD), ability to induce angiogenesis, invasion and metastatic formation [128]. In recent years, their invasiveness and metastatic capacity have attracted interest in studying the role of extracellular matrix mechanical properties in regulating these processes [129,130]. In fact, there is a continuous exchange of information between cells and the ECM that results in a bi-univocal change in cell behavior during the pathological processes [131,132]. Therefore, it has been demonstrated that the biophysical properties of ECM is very important in regulating and perturbing the invasiveness and migration rate processes during tumorigenesis [133–136]. Following, the interest in the cancer biophysics increase because can be used not only to discriminate between healthy and cancerous states [81,137] but, more importantly, to identify the degree of aggressiveness and invasiveness [93], giving to clinicians the possibility to understand tissue response to specific chemotherapists opening to a personalized medicine approach [138].

5.2.2 Tumor-associated p53 missense mutants

In these recent years, thanks to the identification of various somatic mutations in cancer, has been possible to develop several target genes therapy for cancer treatment. In particular, TP53 seems to be the most frequently altered gene in human various tumors [139]. These mutations are "missense mutations" which impact single residues in the core domain by determining in the inability to bind p53-consensus sites on DNA reducing their functionality [140]. It has been observed that this protein mutant is very stable [141], and not occurring in normal tissue [142], giving rise to the possibility that stability is given by oncogenic signals [143]. However, mutant p53 has been demonstrated to be spatially heterogeneous in individual tumors [144,145] hypothesizing that its protein stability may be influenced by local chemical or mechanical environmental signals. These proteins succeed in subverting a remarkable variety of pathways to promote cancer cell survival, proliferation, invasion, migration, stem cell expansion, chemoresistance, tissue remodeling, and chronic inflammation. The specificity of mutant p53 to

the tumor cells allowed to design specific therapies for tumors leaving intact the healthy tissue [146,147]. Mutant p53 leads to the reprogramming of cancer cell metabolism *via* induction of the mevalonate pathway and determines the nuclear localization of YAP-TAZ complex [148] that promotes tumor cell proliferation, disorganized polarity, and cancer stem cell attributes including chemoresistance [149]. In the last year was demonstrated that p53 mutant stabilization depends to mevalonate/RhoA signaling [150]. In addition, the variation of ECM stiffness determines actin polymerization or depolymerization by stabilizing mutant p53 and activating drug resistance, thus facilitating malignant progression.

5.3 Mechanobiology in myogenesis

Myogenesis is the process of muscle (re)generation. The process is divided in different steps: embryonic myogenesis, perinatal phase and adult myogenesis. These lead to the formation of skeletal muscles which are characterized by the expression of contractile, multinucleated fibers, characterized by a highly ordered assembly of sarcomeric myofibrils [151]. Another very important skeletal muscle feature is its capacity to regenerate. This process initiate with the activation of stem cells following usage, injury or disease [152]. The functional development and the regeneration of skeletal muscle is strongly regulated by the extracellular matrix for spatial organization, structural support and, more interestingly, mechanical regulation and support [153]. The ECM can affect cellular behavior through variations in the fiber composition by determining change in local stiffness [154]. Calve S. and Simon H. G. have shown that changes in both local stiffness and chemical/molecular composition of the ECM control and modulate skeletal muscle regeneration [155]. In particular ECM stiffness and macromolecular compositions are most important in two steps of skeletal muscle regeneration called repair phase and remodeling phase [156,157]. In the repair phase the ECM is responsible of the recruitment of stem cells at the point where the damage occurred and to stimulate them to proliferate and differentiate [156,158]. These evidences have generated great interest in the production of biomimetic scaffolds to direct skeletal muscle regeneration [159]. There are two different approaches to obtain scaffolds for skeletal muscle regeneration, *in vitro* and *in vivo* [160,161]. Skeletal muscle regeneration *in vitro* is carried out by seeding myoblasts onto scaffolds made by different materials [162] and that must guarantee, at the end of the regeneration process, all the muscular features [163]. The scaffolds can be formed by synthetic polymers, by decellularized ECM materials and/or by

natural polymers. In the last years, a new class of biomimetic materials was developed characterized by amazing features: as powerful tools in this framework are the Human Elastin-Like Polypeptides (HELPs). This polypeptide structure is formed by repetitive penta-or hexa-peptide motifs detected in human elastin [164,165]. In this thesis work three different peptides have been used and were called HELP, HELP1 and HELPc [166]. HELP and HELP1 are different for the presence of the cross-linking domains and have been tested as growing substrates for myoblastic cells demonstrating that they can stimulate cell proliferation and differentiation: a good indication as effective biomaterials for skeletal muscle regeneration [166]. HELPc differs from the other two peptides from fusing, at the C-terminal, a sequence the α2 isoform of a collagen type IV containing two Arg-Gly-Asp (RGD) motives [167]. I have tested HELPc as growing substrates for C2C12 myoblast cells by comparing with the HELP and HELP1 effect. Therefore, I had seen that HELPc improves the myoblasts adhesion, differentiation and fusion by combining several methods, as immunofluorescence, AFM for mechanobiology analysis and Ca^{2+} imaging [167]. Following, I have exploited a repeat hydrophilic sequence in HELPc, containing Gln and Lys residues, in order to obtain hydrogel matrices. Therefore C2C12 cells were cultured on HELPc hydrogels at different monomer concentration (resulting in different stiffness) to study the biochemical effect together with the mechanical contribution of the hydrogel substrates. Interestingly, comparing the behavior of C2C12cells seeded on glass coated by hydrogels made by different grades of crosslinked HELPc, I found some intriguing differences in cell adhesion, proliferation and differentiation. We concluded that HELPc hydrogels could have a potential application in muscular tissue engineering [168].

Aim of the Thesis

The aim of this thesis work it to demonstrate how a nano-technological tool, as the Atomic Force Microscope is, could be effectively used to study how cells respond to the physical properties of a natural or artificial niche, transducing them into biochemical signals which can alter the cellular system. Changes in the organization, composition and mechanical properties of the extracellular matrix (ECM) could determine significant changes in cell behavior and fate. In this context, the interest, by the clinical scientific community, in studying biomechanical properties is continuously rising due to the fact tissue mechanical properties could be used as a marker for very early diagnosis of pathologies or, likewise important, to develop new prosthetic materials able to stop, or at least slow down, disease progression. For this reason, many companies are focused on developing new (nano-technologic) tools, or simplifying existing ones, in order to improve common diagnostic techniques. Among the various nano-technologic tools available nowadays, the most advantageous in my opinion is the atomic force microscopy (AFM). This belongs to the family of scanning probe microscopes, so it can capture images with sub-nanometer resolution of surface morphology but, due to its extreme versatility, it has been extensively used as well in order to evaluate the interaction forces between single molecule, cell adhesion or, more interesting for my thesis work, the mechanical properties of single cells and/or tissues. In addition to its versatility, AFM does not require any particular sample preparation before characterization that could be perform, in principle, in both hydrated or dehydrated condition, on indifferently, fixed or native cellular samples.

Thus, in this thesis I demonstrated how the Atomic Force Microscopy could be considered the keystone technique able to extend, and be combined to, conventional diagnostic techniques in a clinical setting. To prove that, I described here three examples where AFM demonstrated to be a fundamental tool to study mechanobiology and mechanotransduction drive in the onset of calcific aortic valve disease, regulation of cancer associated p53 missense mutants and, finally, in myogenesis.

Results

6 Mechanobiology in the onset of CAVD

As previously reported, the calcific aortic valve disease (CAVD, hereafter) is strongly correlated with VICs phenotype and with variations in ECM morphological and mechanical properties. Therefore, in this part of my work, I focused my research on the last contribution investigating the changes of mechanical properties in human valve interstitial cells (hVIC) grown on the flat substrates but characterized by different surface stiffness (from 0.5 to 50 kPa). Moreover, I tried to point out, in strong collaboration with the group of Maurizio Pesce and Rosaria Santoro from the Monzino cardiologic center, if the YAP-TAZ complex was related to the onset of the disease. In particular, I took advantage of the Atomic Force Microcopy (AFM) to initially characterize polyacrylamide gel (PAAg) based substrates, evaluating their Young's moduli, and subsequently analyzing the stiffness of hVICs cultured above such supporting substrates. Immunofluorescence experiment and classic biomolecular technics were performed as well in order to follow cytoskeleton rearrangement and YAP-TAZ complex activation.

6.1 Characterization of polyacrylamide gels rigidity

As the first step, four polyacrylamide gels were synthetized by Monzino collaborators at different stiffness and deposited on supporting glass slides (Fig. 17a). These fabrication phase was based on the pioneering work published by A. Engler and co-workers [169]. In 2006 have demonstrated that ECM stiffness may strongly influence mesenchymal stem cells destiny. In particular, mesenchymal stem cells developed on rigid substrates (25-40 kPa) differentiate in osteoblasts, while, when grown on soft substrates (0.1-1 kPa) differentiate instead in neuroblasts [169]. Considering the strong contribution that substrate stiffness could have on cell (pro-patological) evolution or behavior, a perfect knowledge of such physical value is mandatory. As consequence of that we quantified the rigidity of PAA gels by means of Atomic Force Microscopy force spectroscopy (see Methods for technical details). PAA gels were subsequently named depending on their mechanical compliance as follow: Low stiffness [L, about 3.05±1.95 kPa in Young's modulus], Mid-Low stiffness [ML, 18.06±2.82 kPa], Mid-High stiffness [MH, 28.71±1.95 kPa] and High stiffness [H, 58 kPa, normalized value] (Fig. 17).

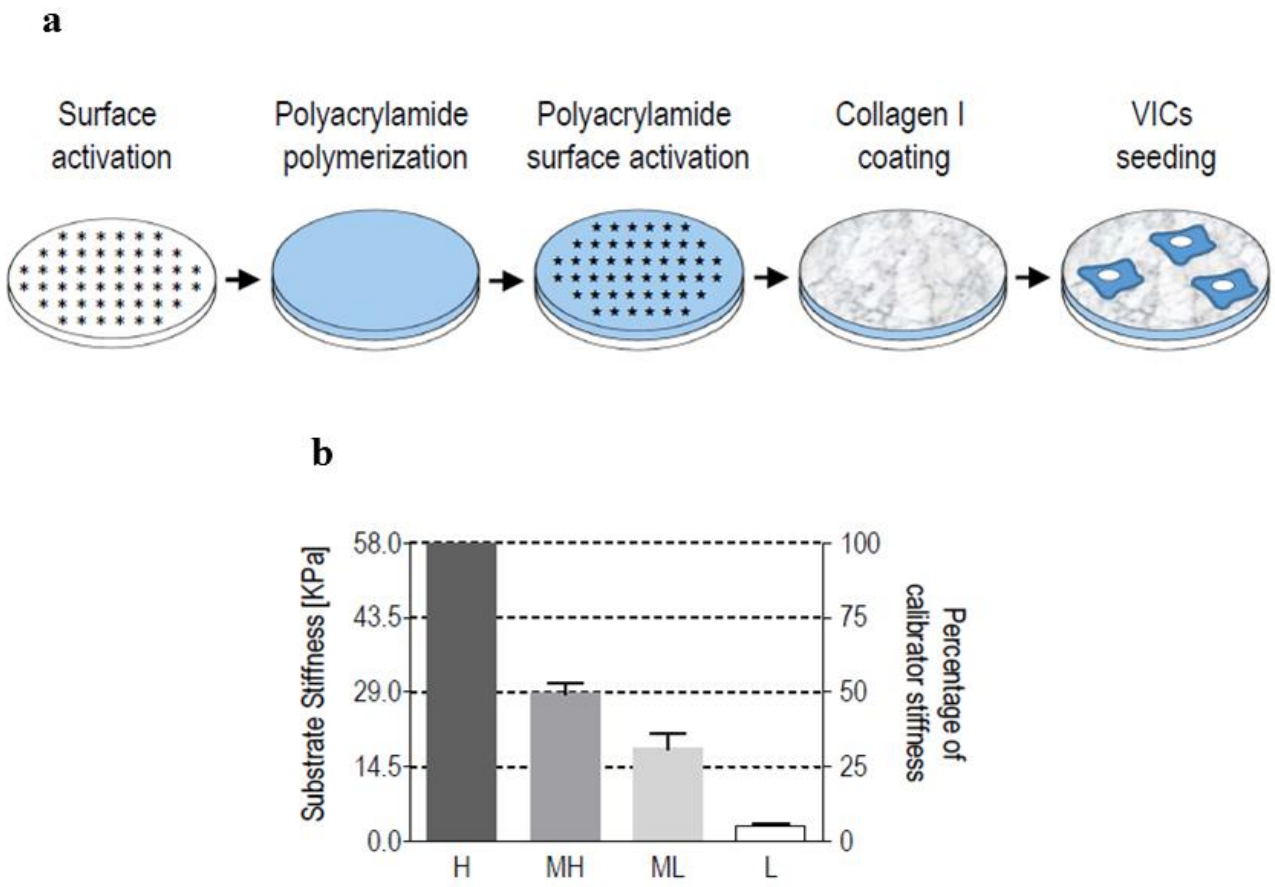

Figure 17: *Characterization of substrate: (a)Experimental design in order to obtain the PAA gels at different stiffness; (b)Substrates stiffness quantification (High (H),Medium High (MH), Medium Low (ML), Low (L); n=6).Image designed in collaboration with the Monzino Cardiologic Research Center.*

6.2 Cellular rigidity is determined by the rearrangement of the cytoskeleton

In real condition- inside an aortic valve, VICs phenotype is strongly affected by the mechanical heterogeneity of the tissue valve [117,118]. Therefore, understanding the contribution of substrate rigidity on VICs morphology has strong scientific and medical relevance (Fig. 18). In particular, the study of α-SMA and F-actin in hVICs grown on different substrates, pointed out a strong co-localization in cells developed on the stiffer substrates (on glass and High), allowing the identification of three different cell morphologies. On Medium High and Medium Low substrates, instead, the co-localization is statistically lower until the case of cells grown on the Low stiffness substrate where the alpha-SMA signature is totally lacking. In order to quantify

morphological differences in cells' morphology when interfaced with substrates of different stiffness, we carried out quantitative cell morphometric analysis (Fig 18b-d). From the data of cellular perimeter and area (Fig. 18b-d) it is very clear that an increase in substrate stiffness determines a significant increase in cellular spreading.

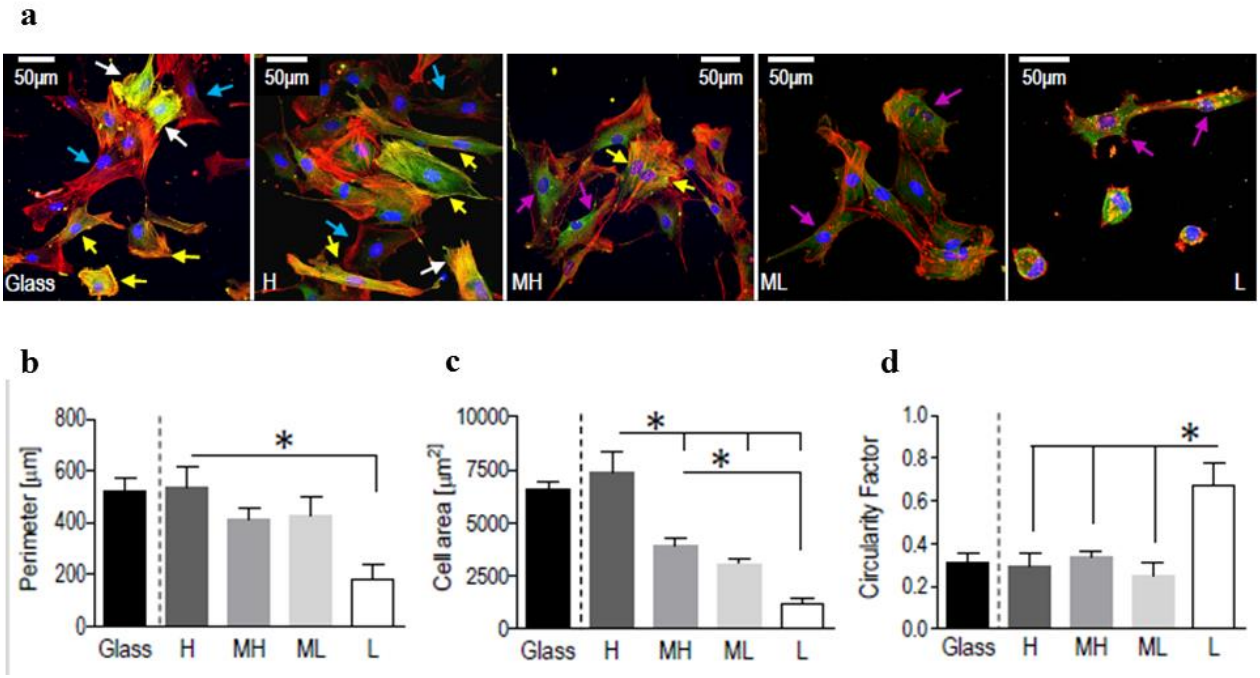

Figure 18: *hVICs shape depends to substrate stiffness: (a)Immunofluorescence images of hVICs grown on GLASS and on polyacrylamide gels at different stiffness(red: phalloidin; blue: DAPI; green: α-SMA; white arrow: high levels of α-SMA and co-localization; yellow arrow: intermediate levels of α-SMA and co-localization; blue: low levels of α-SMA and co-localization; purple arrow: no α-SMA; 60X); (b)Cell perimeter [µm]; (c)Cell area [µm^2]; (d)Circularity Factor; (p<0.05,1-way ANOVA; n=6). Image designed in collaboration with the Monzino Cardiologic Research Center.*

Following such analysis we evaluated, taking advantage of AFM force spectroscopy, if the cell stiffness changes as function of substrate rigidity. Figure 19b point out how VICs stiffness is strongly influenced by the rigidity of the underlying substrate. In order to try to explain molecular basis of such increase in cellular rigidity, we estimated the amount of focal adhesions (FAs) and the results of this analysis are summarized in Figure 19a. In particular, we carried out the immunofluorescence essay to Vinculin. This protein have an important role in mechatransduction and its accumulation inside FAs complexes is regulate by transmission of intracellular forces directly connected to cytoskeleton strain and, finally, by ECM stiffness [27]. In accordance with

such mechanism we found that on the glass the number of FAs is significantly higher and better-defined in shape than on softer substrates: consequently a reduction in substrate rigidity results in a reduction in FAs (Fig. 18a).

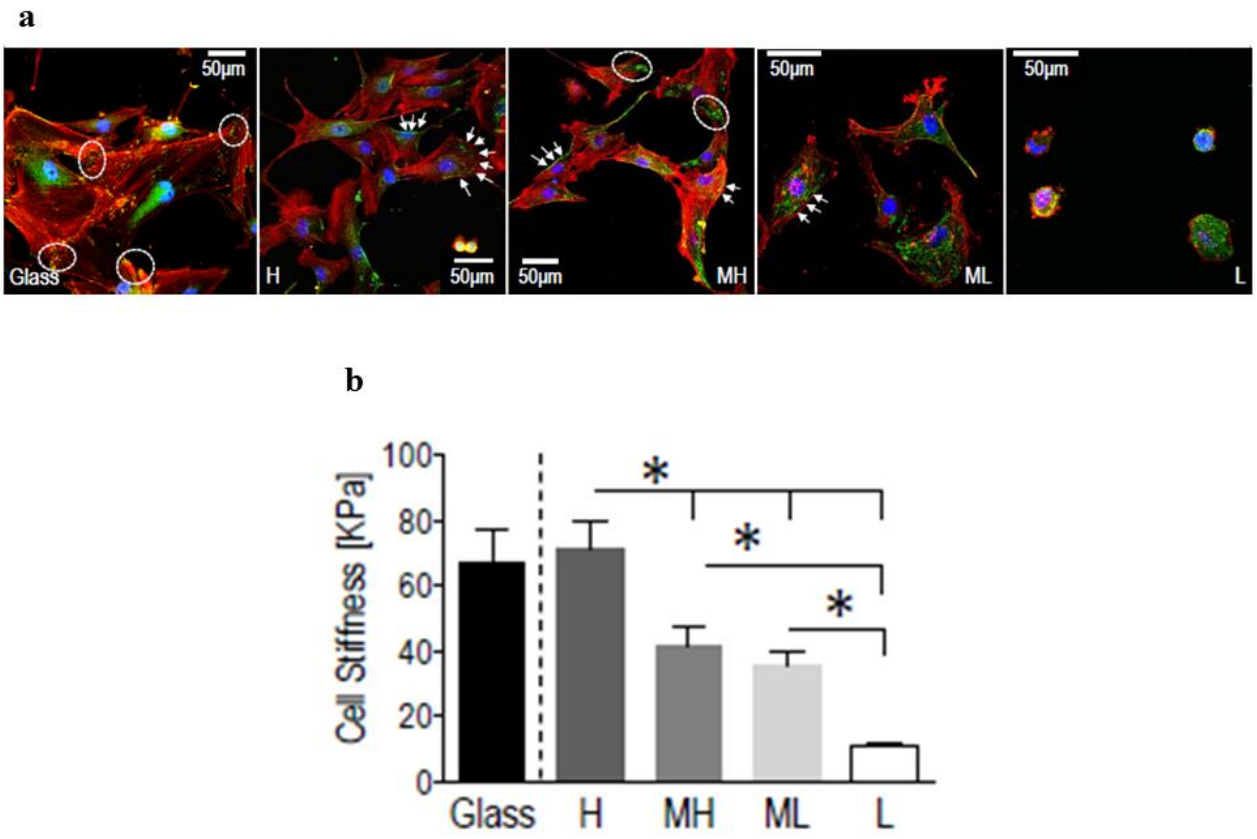

Figure 19: *hVICs stiffness depends to the substrate stiffness: (a)Immunofluorescence images of hVICs grown on GLASS and polyacrylamide gels at different stiffness(red: phalloidin; blue: DAPI; green: vinculin; 60X); (b)Cell stiffness; ($p<0.05$,1-way ANOVA; n=6). Image designed in collaboration with the Monzino Cardiologic Research Center.*

6.3 High cytoskeleton tensioning determines high levels of YAP nuclear localization

In the canonical Hippo pathway, the YAP-TAZ complex is inactive due to phosphorylation and localized in the cytoplasm. However, when the cells are subject to a mechanical stress, this complex is activated to the non-canonical Hippo pathway and translocated in the nucleus. This translocation determine the activation of specific genes transcription [57]. Relying on these concepts we evaluated nuclear localization of the YAP-TAZ complex in hVICs grown on gels at

different stiffness (Fig. 20). Accordingly, as pointed out by immunofluorescence analysis (Fig. 20a), we directly quantified the percentage of nuclear YAP localization (Fig. 20b). In Figure 20b is shown how an increase in substrate rigidity induce YAP activation in terms of nuclear translocation.

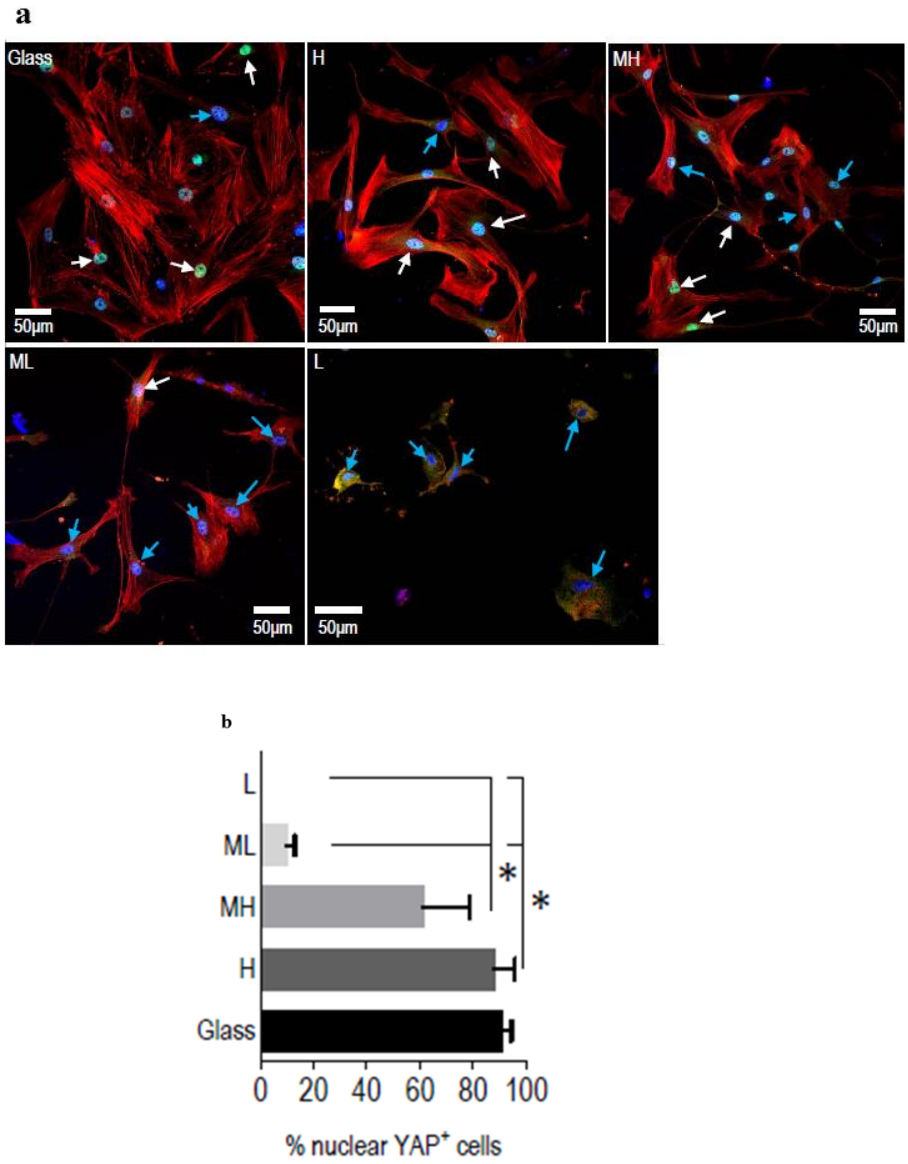

Figure 20: YAP nuclear localization depends to substrate stiffness: *(a)Immunofluorescence images of hVICs grown on GLASS and polyacrylamide gels at different stiffness(red: phalloidin; blue: DAPI; green: YAP; white arrow: Nuclear YAP localization; blue arrow: not nuclear YAP localization); (b)Percentage nuclear YAP localization;($p<0.05$,1-way ANOVA) Image designed in collaboration with the Monzino Cardiologic Research Center.*

In order to investigate which gene expression process is dependent upon YAP activation and, of course, the possible reversibility of such process, we initially pointed our attention on a condition of strong cellular stress by seeding hVICs on a glass substrate. It is important here to stress about the fact the cellular condition on the glass substrate is very similar from both molecular and mechanical aspects to the condition on the High stiffness PAAg substrate. In this framework, to simulate a low rigidity condition, we treated hVICs with the pharmacological inhibitor of rho-associated protein kinase (ROCK) signaling pathways Y27632 (Fig. 21a). The inhibitor, selectively interfering with p160ROCK [170], blocks the rho kinase and prevents actin polymerization by reducing cellular tensions [44]. Cellular treatment with Y27632 (see Methods for details) induces in hVICs a localization of YAP similar of what was observed plating cells on a soft surface, in fact, any observable nuclear localization of YAP was visible. Interestingly, the phenomena is completely reversed 24 hours after drug washout/removal (Fig. 21a). To support this immunofluorescence data, we carried out western blotting analysis confirming, once again, significant YAP phosphorylation (pYAP-ser127) in response to Y27632 cellular treatment (Fig. 21b).

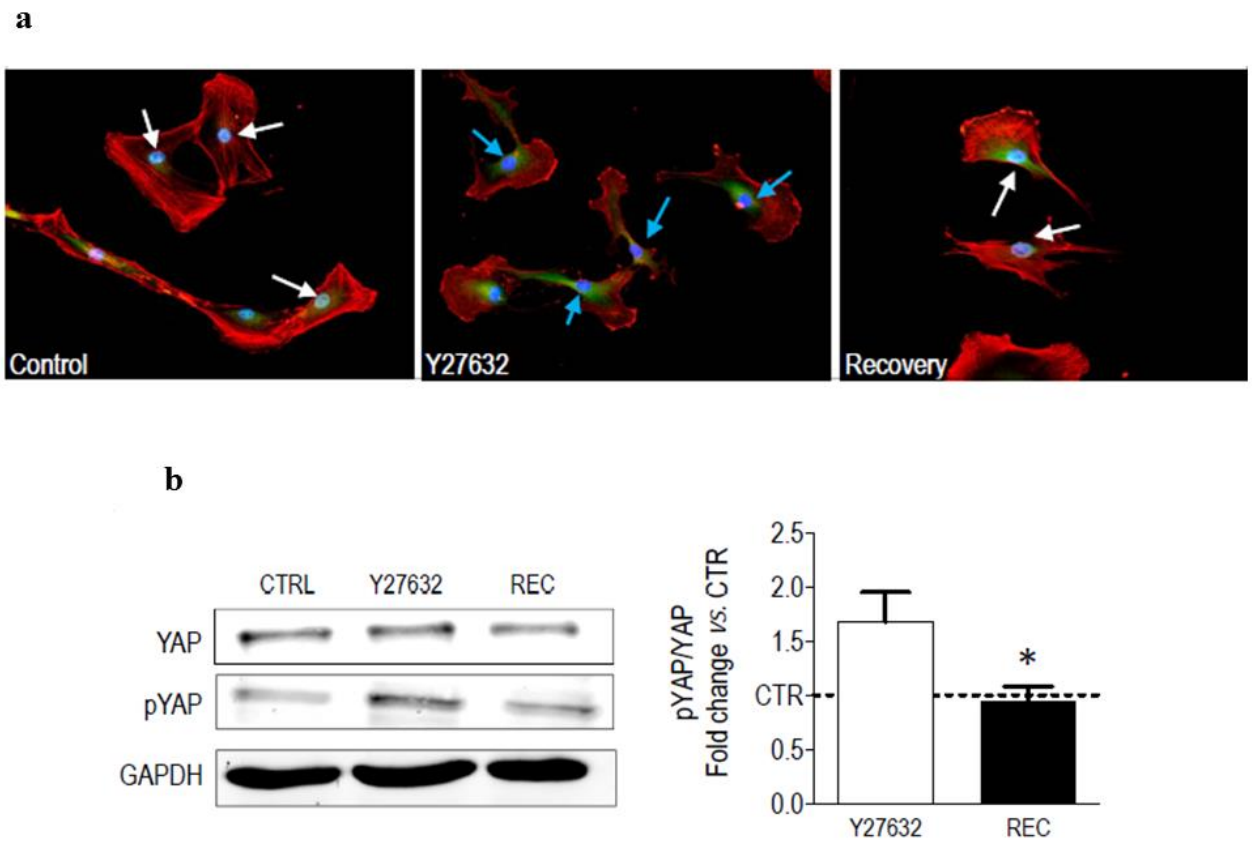

Figure 21: *Pharmacological inhibition of RHO kinase determine the YAP inactivation in hVICs grown on GLASS: (a)Immunofluorescence images of hVICs grown on GLASS treated with Y27632(red: phalloidin; blue: DAPI; green: YAP; white arrow: Nuclear YAP localization; blue arrow: not nuclear YAP localization); (b)Representative western blot with the indicated antibodies. pYAP is significantly upregulated in hVICs treated with Y27632 to CTRL while pYAP is significantly downregulated 24 hours after drug removal to CTRL ($p<0.05$,T-test). Image designed in collaboration with the Monzino Cardiologic Research Center.*

Following that, we start investigating the role and regulation of three YAP target genes, called ANKRD1, CTGF, CYR61. This point was assessed by reverse transcription polymerase chain reaction (Q-RT-PCR) on mRNA fragments extracted from hVICs when cultured in the same two conditions of previous experiments: cells on glass and cells on glass but treated with Y27632 (Fig. 22). Data in Figure 22 confirms us that a cytoskeleton fibers de-polymerization, associated with a downregulation of YAP target genes, took place as consequence of YAP phosphorylation.

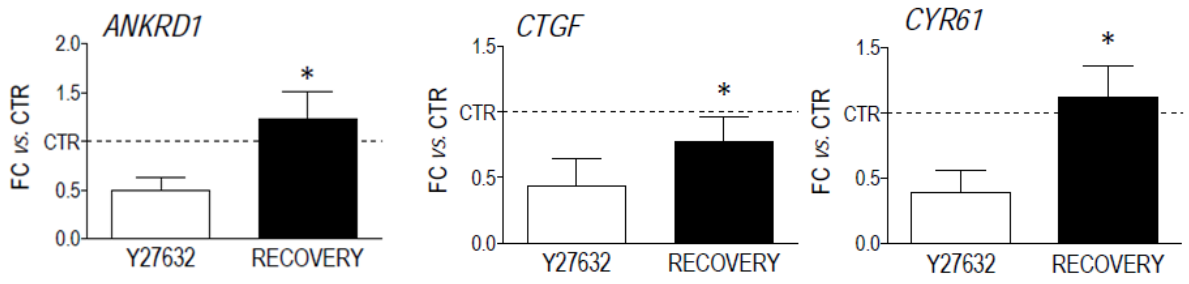

Figure 22: *gene expression regulation YAP-dependent: ANKRD1, CTGF, CYR61 are significantly downregulated in hVICs treated with Y27632 to CTRL while are significantly overexpressed 24 hours after inhibitor removal to CTRL (p<0.05,T-test). Image designed in collaboration with the Monzino Cardiologic Research Center.*

In the same manner as these results, we hypothesized that a similar inhibitory effect could be highlighted even on hVICs by cell stiffness evaluation via AFM. Therefore, we measured the cellular stiffness in control (non Y27632 treated) cells, after the pharmacological inhibitor treatment and after 24 hours from drug removal in order to study cell recovery (Fig. 23). Surprisingly, we observed that actually Y27632 has any significant effect in cell stiffness modulation immediately after treatment (see Methods) but, a significant (P<0.05) effect in terms of stiffness reduction was measured on hVICs 24 hours after inhibitor removal. Relying on this unexpected result, we decided to repeat the experiment evaluation cell stiffness after 48 hours too. In this last condition I observed effective cell stiffness recovery (Fig. 23).

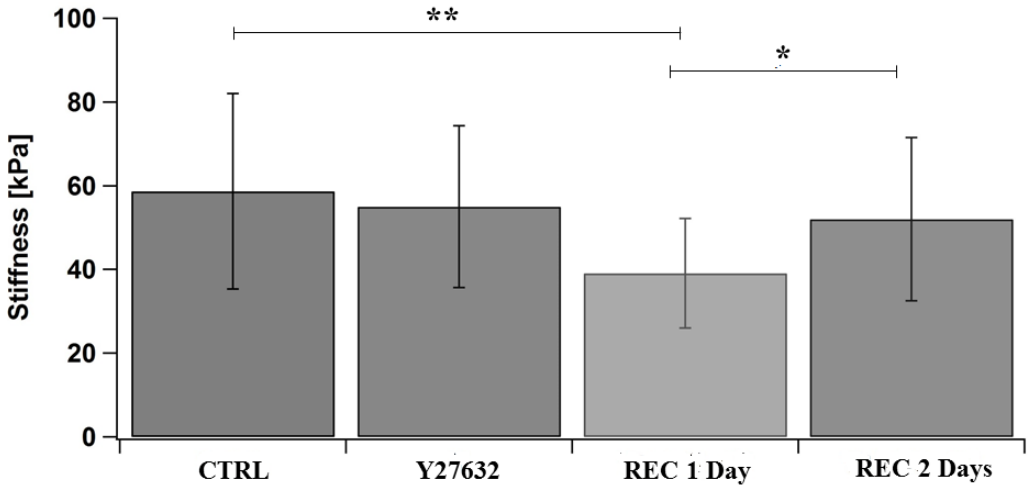

Figure 23: *Effect of treatment with Y27632 on hVICs stiffness (p<0.05=*; p<0.01=**, T-test; n=6). Figure designed in collaboration with the Monzino Cardiologic Research Center.*

We also evaluated ACTA2 gene expression, the α-SMA encoding gene in hVICs. We discovered that ACTA2 gene expression (Fig. 24) has a similar trend as the gene expression of YAP's target gene (Fig. 22). In point of fact, we observed a down-regulation in treated cells and an up-regulation 24 hours after drug removal (Fig. 24) suggesting a myofibroblast-like conversion of hVICs regulated by cytoskeleton tension, through the activation of a YAP-dependent pathway. Moreover, comparing ACTA2 gene expression (Fig. 24) and the inhibitory effect it has on hVICs stiffness (Fig. 23), allowed us to hypothesize that the effect induced by mechanical stress is reversible, but the mechanical recovery of cytoskeleton rearrangement occurs more slowly than the molecular recovery. However, this hypothesis needs to be supported by further experiments in order to be confirmed and this is the intriguing aspect I proposed to explore in the future.

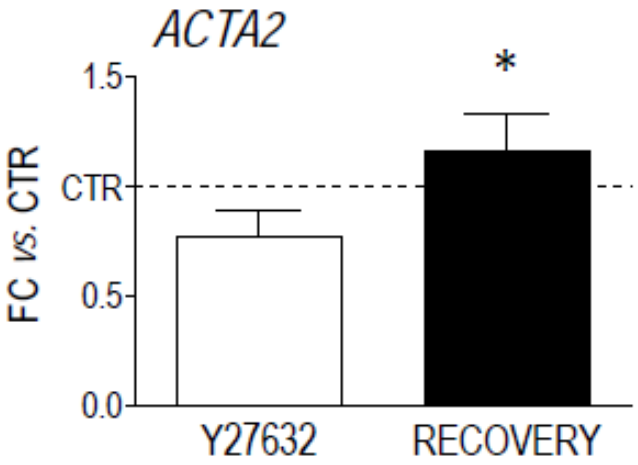

Figure 24: *ACTA2 gene expression regulation YAP-dependent: ACTA2 are significantly downregulated in hVICs treated with Y27632 to CTRL while are significantly overexpressed 24 hours after inhibitor removal to CTRL ($p<0.05$,T-test). Figure designed in collaboration with the Monzino Cardiologic Research Center.*

6.4 The stiffness modulated also in the ex-vivo tissue: Stiffness of the human leaflet

The next step of my research dealt with the translation the *in vitro* experimental procedures and observations described in previous paragraphs to an *ex vivo* model constituted by transversal thin sections of explanted stenotic calcific human valves, obtained from patients that underwent aortic valve replacement.

In order to study the variations in tissue stiffness in leaflet valve sections we performed AFM force mapping of all the sample (Fig. 25a). AFM force mapping measurements pointed out a clear stiffness distributions in the tissue. In order to identify reasons of such local differences in mechanical properties we compared such compliance map with a colored histological map of a contiguous section of tissue where hydroxyapatite (HA) aggregation areas were pointed out by Von Kossa staining and eosin (see Methods). In this way, I could correlate and quantify the rigidity of calcific and non-calcific areas (Fig. 25b). In particular, I observed an average value of tissue stiffness for non-calcific area of about 15.06±9.5 kPa while calcific areas were characterized by a value of Young's modulus of about 28.44±6.5 kPa (Fig. 25c).

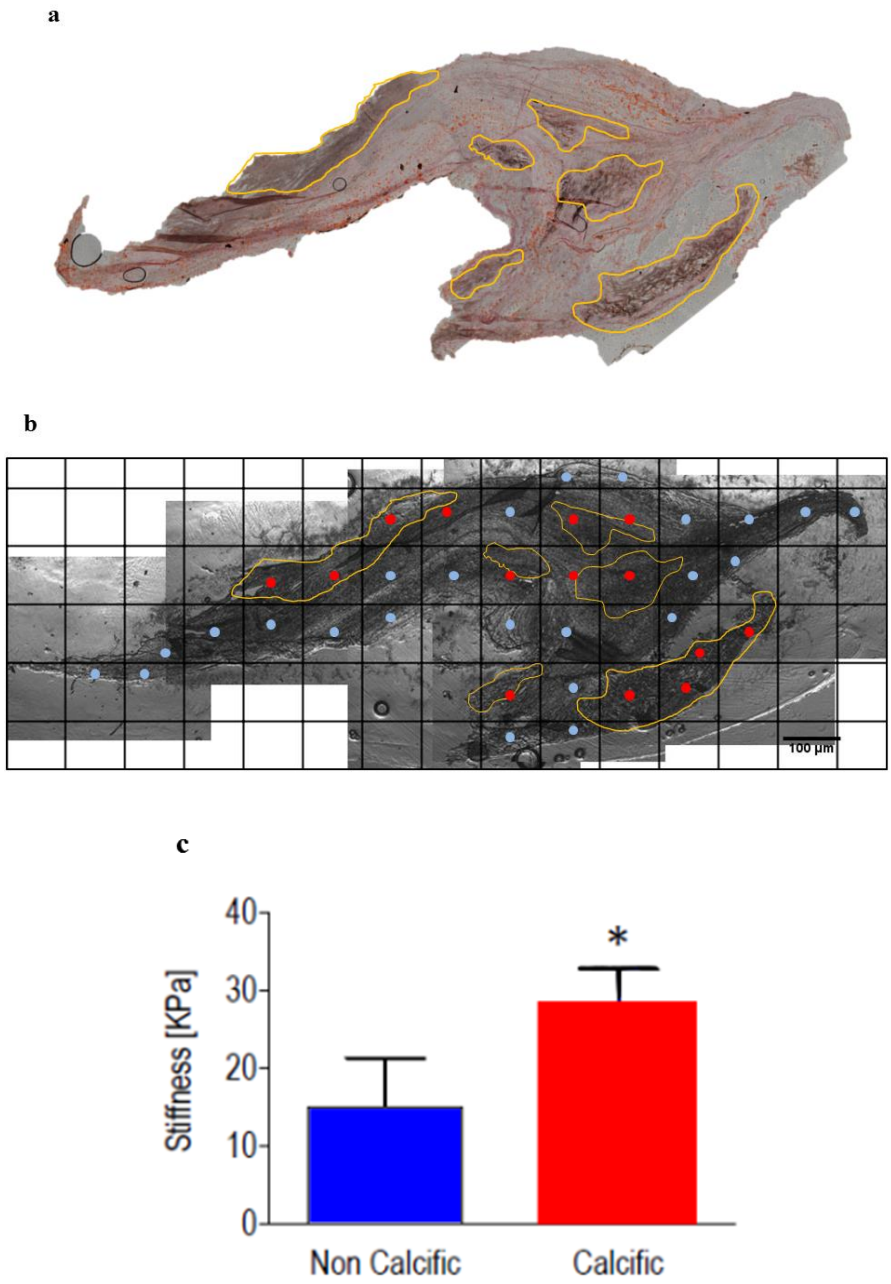

Figure 25: *AFM force mapping of human leaflet valve section: (a)example of human leaflet valve section stained by Von Kossa (calcific area highlighted in orange) and eosin; (b)Example of optical image of human leaflet valve section divided into squares 100 µm x 100 µm; the dots represent the positions where the force distance curves were acquired (red dots: calcific area; blue dots: non-calcific area); (c)Stiffness plot of calcific and non-calcific areas (p<0.05,T-test; n=3). Figure designed in collaboration with the Monzino Cardiologic Research Center.*

Following our standardized procedure, we evaluated as well the nuclear localization of YAP in hVICs performing an immunofluorescence staining on valve leaflets (see Methods). In Figure 26a a nuclear localization of YAP in the cells is shown in the calcific areas of the tissue. To further confirm our hypothesis of an *in vivo* mechanosensing driven regulation of hVICs through a pro-pathological differentiation, we studied and confirm the co-localization of YAP and α-SMA in stiffer areas of the sample (Fig. 26b). In fact, from Figure 26b, the co-accumulation of both stained regions in the calcific areas is clear (see white arrows).

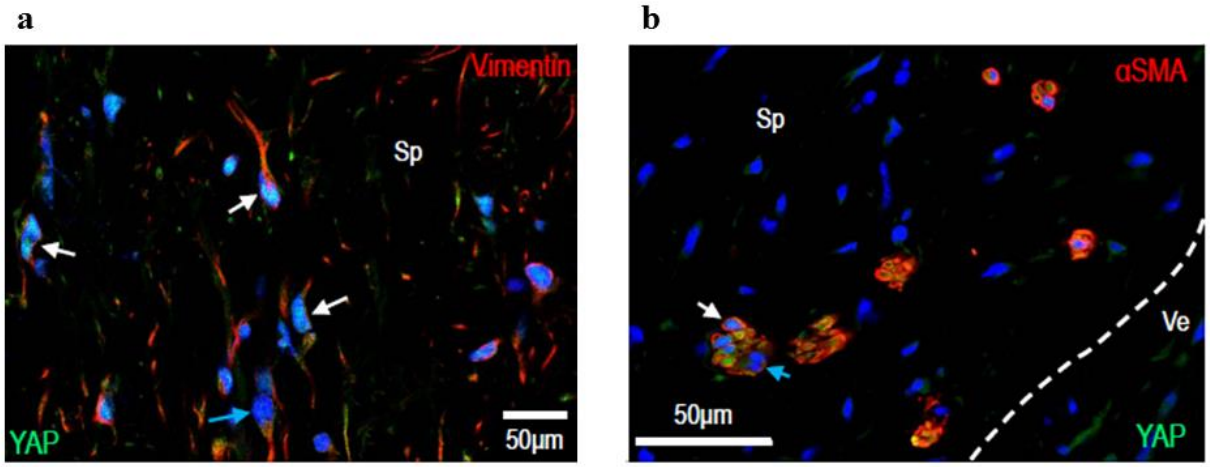

Figure 26: *Immunofluorescence staining of human leaflet valve section: (a)human leaflet valve section stained for YAP and Vimentin (red=vimentin; green=YAP; white arrow= nuclear YAP localization; blue= not nuclear YAP localization); (b)human leaflet valve section stained for YAP and α-SMA (red: α-SMA; green: YAP; white arrow: co-localization; blue arrow: not co-localization); (n=3). Figure designed in collaboration with the Monzino Cardiologic Research Center.*

7 Morphological and functional adaptation of porcine VICs when interfaced to a nanostructured substrate

As already introduced, VICs phenotype destiny could be driven by the interaction with a substrate of different compliance [171] as exhaustively described in the previous section, or by the chemical and/or morphological contribution of extra-cellular matrix (ECM) properties. In the following section I started investigating such aspect interfacing porcine valve interstitial cells (pVICs) to nanostructured substrates that mimic ECM morphology. I choose to move to an animal model, using primary porcine cells instead of continue using hVICs, by the fact that larger sets of experiments would have been necessary to accomplish all the programmed experiments and ease of availability of pVICs resulted to be the only reasonable option. In order to nanostructure surfaces used for these experiments I took advantage of multi-walled carbon nanotubes (MWNTs) carpets directly grown on supporting glass slides (see Methods). These well-studied and characterized nanostructured coatings mimic very well the ECM structure in terms of morphology [172]. To accomplish my experimental needs, together with Ilaria Rago and the group of Dr. Andrea Goldoni at ELETTRA, a novel strategy to grow via chemical vapor deposition (CVD) CNTs on a glass slide was developed (see Methods). Following this new procedure transparent CNT substrates have been obtained allowing, for the first time, to perform simultaneously immunofluorescence essays, to point out cell morphology and phenotype, and cell mechanic analysis via AFM, in order to determine pVICs stiffness when interfaced (or not) to the nanostructured substrate. Moreover, we discovered that CNTs carpets we used had a stiffness (Fig. 27) very close to the stiffness values characterizing Middle-High (NH) and Middle Low (ML) polyacrylamide gels (Fig. 17b). From what I discovered in my previous experiments, described in section 6, I know that this rigidity has the effect to keep cells in a quiescent state. This “neutral” condition is supported as well by the fact this stiffness value is very close to the one characterizing healthy valve inlets. Such condition will allow us to decouple cell behavior from substrate stiffness contribution but focus only to the effects related to substrate morphology.

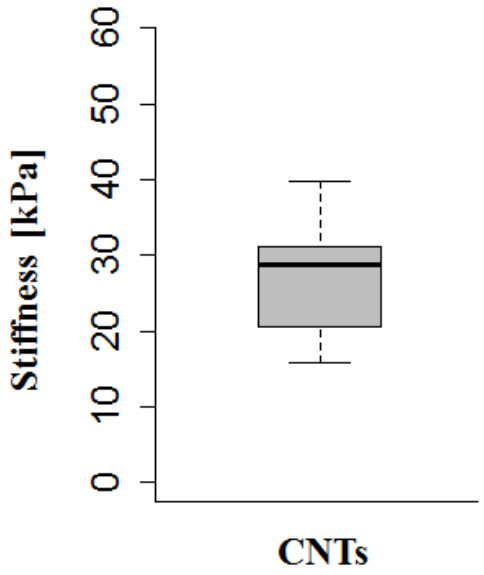

Figure 27: *Substrates stiffness quantification with AFM (Median: 28.80 kPa; Mean: 27.50 kPa; n=5)*

7.1 Characterization of the transparent carbon nanotubes substrates

CNTs were synthetized directly on supporting fused silica glass substrates via catalytic chemical vapor deposition (CCVD) using an ultra-thin iron film (0.2±1 nm in thickness) deposited without any adhesion layer via thermal evaporation (see Methods). In this process, catalyst film thickness plays an important role because CNTs grow from the iron nanoparticles forming during a subsequent thermal annealing process [173]. Size and density of the nanoparticles covering the glass surface are controlled by the annealing thermal treatment parameters (mainly temperature and time) and by the thickness and adhesion of the initial iron layer [174]. Other research groups have used intermediate metallic layers as adhesion and/or anti-diffusion layers between the catalyst and the underneath support surface in order to enhance CNT growth yield [175]. In our CCVD synthesis method any adhesion metal layer was employed and, even if the growth time was limited to few minutes, the obtained CNTs carpet covering the supporting substrate demonstrated to have the same characteristics of carbon nanostructures produced with adhesion-layer use or by using more time-consuming methods. These peculiarities of our laboratory-scale process, together with inexpensiveness and the fact final samples are transparent to visible light make it an extremely interesting substrate model for research purposes.

FE-SEM imaging was performed on CNTs mat in order to investigate the tubes' diameter, length, uniformity and density. In Figure 28a is showed vertical aligned CNTs, oriented perpendicularly to the surface substrate while the TOP view (Fig. 28b) revealed a random orientation. The parallel morphology is established by the proximity effect of densely distributed catalyst nanoparticles forcing the initially randomly oriented CNTs into a vertical alignment [176].

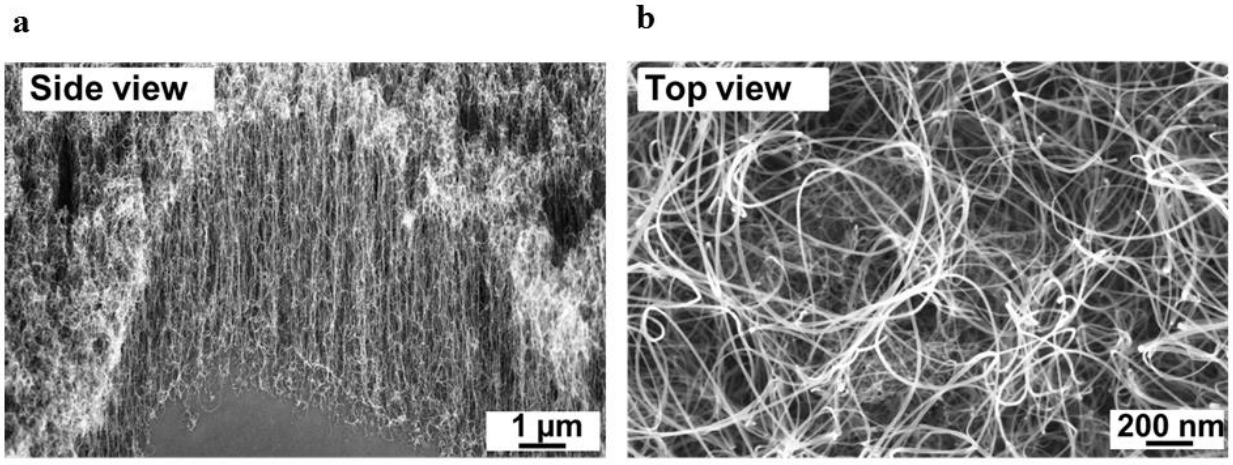

Figure 28: *(a)Top and (b)side SEM views of CNT substrates revealing a random orientation and a vertical alignment of nanotubes, respectively.*

In order to highlight the structure and crystallinity of CNTs, TEM characterization was conducted. Therefore, we have seen that CNTs consist of multi-walled nanotubes with different wall number. Specifically, Fig. 29a shows an isolated MWNT with an outer diameter (OD) of less than 20 nm and an inner diameter (ID) of approximately 10 nm. These measurements are consistent with 15 nanotube walls (Fig. 29b). However, TEM analysis points out the presence of structural defects (Fig. 29a), generally imperfections of conjugated sp_2 carbon along the tubes, such as breaks, sp_3 hybridized carbon atoms, Stone-Wales defects (i.e., two heptagons and two pentagons), probably ascribed to the temperature used to grow our CNTs compared to other methods (730 °C) [177,178].

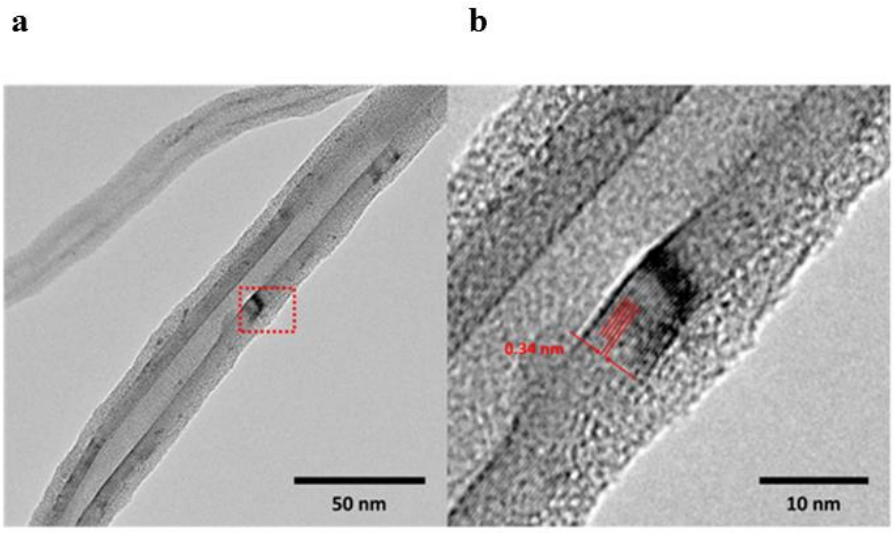

Figure 29: *(a)TEM image of multi-walled nanotubes with different wall number constituting the mat and a particular of an isolated MWCNT (b)showing well-resolved single walls.*

Raman spectroscopy analysis was performed in order to evaluate the degree of structural ordering and the quality of CVD-grown CNTs. The two main bands typical of all graphite-like materials, including MWCNTs, present in Raman spectra (Fig. 30c) correspond to: the G band at ~1583 cm^{-1} related to the in-plane tangential vibration of sp_2 carbon atoms resulting from the graphitic nature of CNTs and the D band at ~1330 cm^{-1} indicating the presence of amorphous and/or low ordered carbon structure (carbonaceous impurities with sp_3 bonding, and broken sp_2 bonds in the sidewalls) [179]. The quality of CNTs is generally expressed by the ratio between the D (ID) and G (IG) band integral intensities. Specifically, similar intensities of this bands [180], as in our case, suggested the presence of non-graphitic carbon in nanotubes, typical for low temperature CVD-grown CNTs [181]. Together with the G band, the second-order Raman peak G' is characteristic of graphitic sp_2 materials and is located at ~2700 cm-1. The G' band, an overtone mode of the D band [182], is associated with defect density, but not as crucially as the first order mode. It was also reported that the intensity of this peak depends significantly on the metallicity of CNTs [183]. Other peaks located at ~1698 cm^{-1} and at ~1759 cm^{-1} are related to νC=O vibration [184,185] and indicate a possible partial oxidation of MWCNTs. From the other hand, the XPS survey spectrum of CNTs (Fig. 30a) makes points out the presence of three elements clearly identifiable: carbon (C1s), oxygen (O1s) and silicon (Si2s, 2p). The amount of C and O are 87.6 % and 10 %, respectively while a small amount 2.4 % of Si was present. Fig. 30b

indicates the C1s core level for ~8 μm long CNTs. A Shirley background has been subtracted. The most intense peaks are located at 284.7 eV and 285.8 eV and can be assigned to sp_2-hybridized graphitic carbon atoms located on CNTs walls and to amorphous carbon (sp_3-hybridized carbon atoms), respectively [186,187]. The amorphous carbon is likely due to the CNTs synthesis process, as confirmed by the structural defects identified via TEM (Fig. 29a) and Raman spectroscopy (Fig. 30c); the peak at 290.8 eV corresponds to the electron energy loss peak due to π-plasmon excitations. These three peaks are characteristics of C1s core level from CNTs [188]. The additional small peaks at 287.15 eV and 288.4 eV are assigned to the presence of oxygen [189].

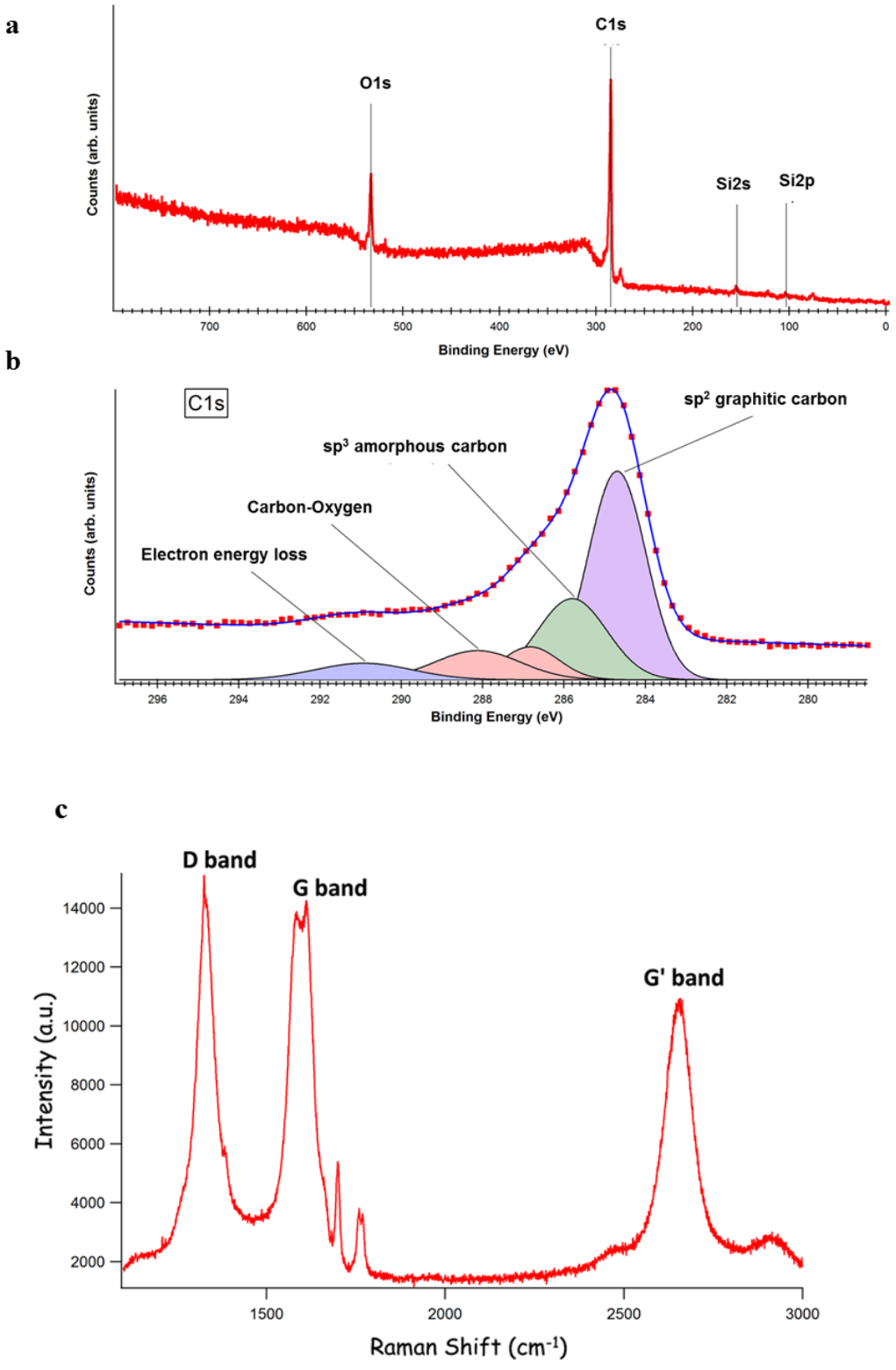

Figure 30: *(a) XPS survey; (b) spectra exhibiting characteristic peaks of CVD grown MWCNTs; (c) Raman and C1s core level.*

7.2 Substrate (nano)structuration contribution in changing cell morphology

CNTs were interfaced in many studies with cell cultures [190,191] revealing, in some cases, to have a toxic effect on cells. In particular, solution-floating single-walled carbon nanotubes (SWCNTs) seem to induce changes in cell morphology associable to reduced cell viability, induction of necrosis, reduced phagocytic ability, increased ROS levels, induction of regulation of gene expression and cytokine release [190]. In another set of publications were demonstrated that water dispersions of MWCNTs can be cytotoxic, genotoxic too and, moreover, could induce cellular apoptosis if present in solution at high concentrations [191]. In CNTs decorated glass surfaces produced in our laboratory nanotubes are strongly attached to the underneath glass support and, as previously demonstrated [192], in this condition they usually do not show to have cytotoxic effects, or any negative effect, on cells cultured above them (toxic effects from CNTs contaminants or pollutions has, anyhow, to be always considered). Despite these evidences from literature, preliminarily to any experiment, an evaluation of toxic effect of CNTs on my cell cultures were done. Therefore, I verified the efficiency of cell adhesion and any possible toxicity of CNTs by immunofluorescence essays after 12 and 72 hours by seeding (Fig. 31a-d, see Methods for more details). In Figure 31e it is possible to see that there is any significant difference between cell densities from both cultures developed on control glass substrates or on CNTs providing evidence not only about the fact that our nanostructured surface, mimicking a real ECM, is not toxic for the cells but points out VICs' good adhesion on CNTs substrates.

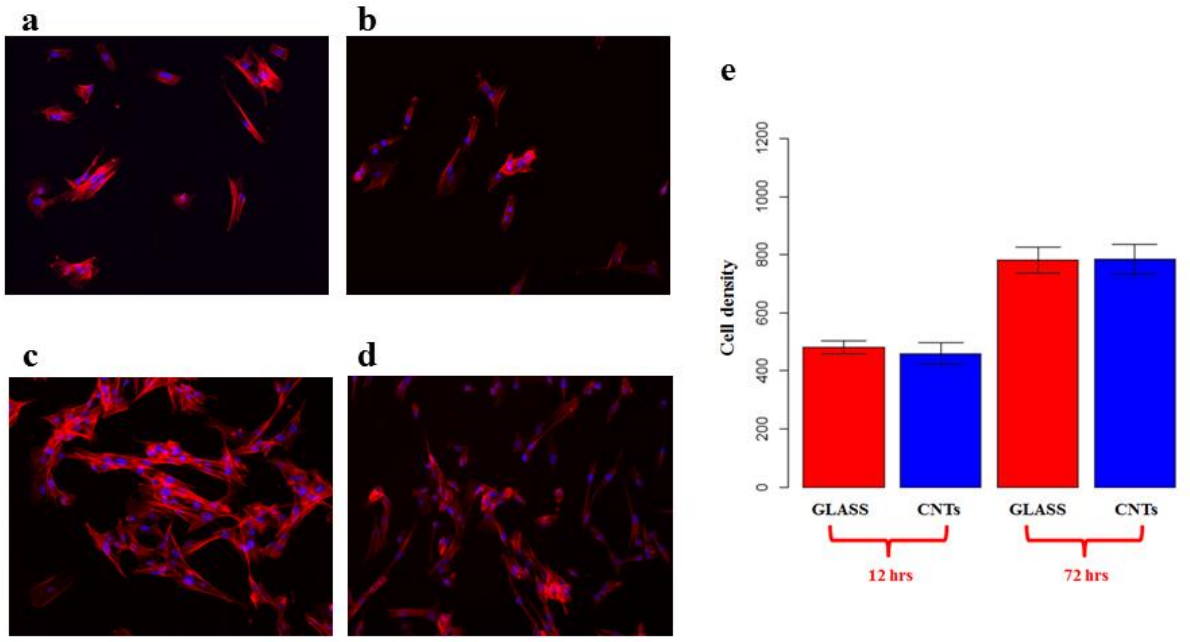

Figure 31: *adhesion and density of VICs grown on glass and CNTs: a-b)Immunofluorescence images of cells grown on glass (a)and CNTs (b)after 12 hrs from seeding. (c-d)Immunofluorescence images of cells grown on glass (c)and CNTs (d)after 72 hrs from seeding (red: Phalloidin; blue: DAPI; 20×). (e)Histograms comparing cell densities on the two different substrates at 12h and 72h time points (T-test p>0.05; 5 sets, 25 fields for set).* Bar-scales in a-d is 50 μm

After confirmation of CNTs safeness in terms of cell survival, we exploited the knowledge that ECM morphology could induce phenotypic variation in VICs during the onset of the CAVD [112,116], I started studying how the our nano-structured surface made by CNTs affects the morphology and phenotype of the pVICs. Regarding the first aspect, after having marked cells with a fluorescent probe targeting actin (see Methods), I evaluate the area (Fig. 32a) and the area *vs*. perimeter ratio (Fig. 32b) for cells grown on both substrates (control and CNTs). From Figures 32a-b it is evident that cells grown on glass appear more spread on the substrate than those grown on CNTs and, moreover, this effect is clearly not time dependent.

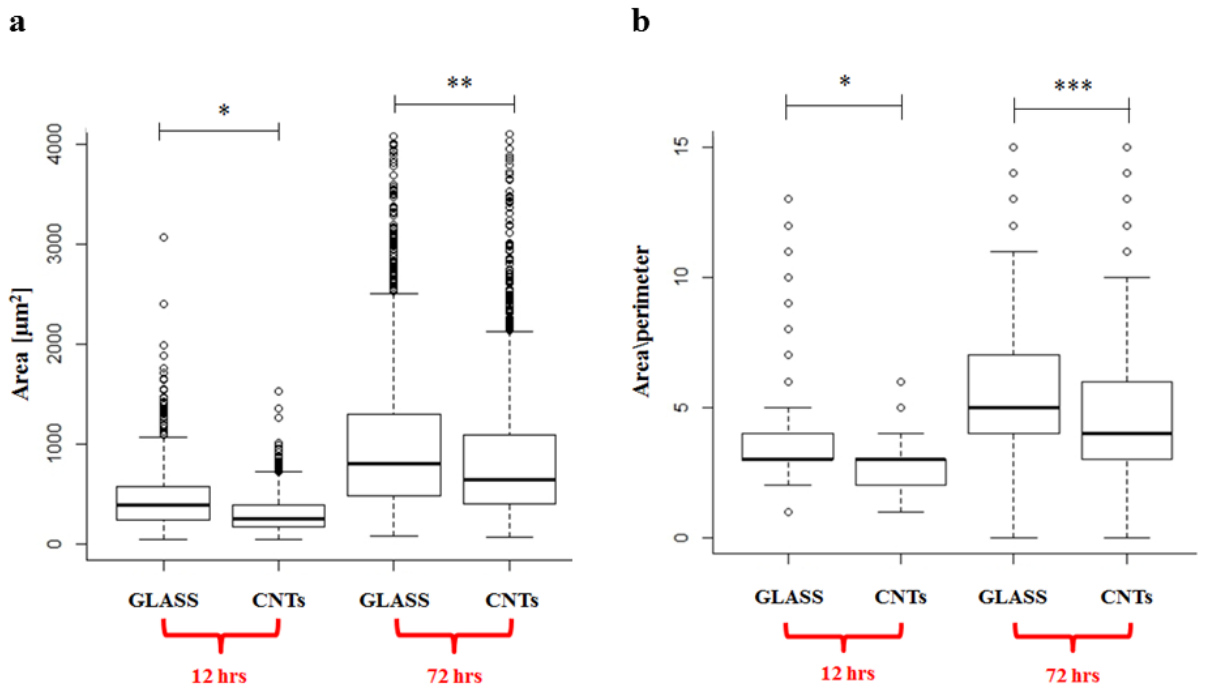

Figure 32: *Morphological characterization of VICs grown on glass and CNTs. a)Quantification of the cells area after 12-72 hours by seeding. b)Quantification of the ratio area vs perimeter after 12-72 hours by seeding (T-test p<0.05=*, p<0.01=**, p<0.001=***, set=3, 25 fields for sets).*

Regarding instead the later aspect, in Figure 33 I direct my attention to the specific shape of cells identifying three different cell morphology that I subsequently associate to three different cell phenotypes: i) myofibroblasts (Mfib), characterized by a relatively spread shape and large area; ii) fibroblasts (Fib), characterized by a strongly elongated shape and, iii) smooth muscles cells (SMc), characterized by small areas and narrow shapes. By the fact there are any good markers allowing discrimination between these three phenotypes I based my classification only on morphology as already done in literature [193,194]. From pie chart in Figure 33 it is very clear that myofibroblast percentage rises on glass substrates than on CNTs (respectively 50% of total on glass controls and 10% on CNTs). It has to be noted that the amount of myofibroblasts I observed on glass controls is similar to the percentage of such kind of cells in unhealthy valves (e.g. calcific heart valve syndromes), while their percentage when interfaced with CNTs has a resemblance in quantity to the healthy valve [116].

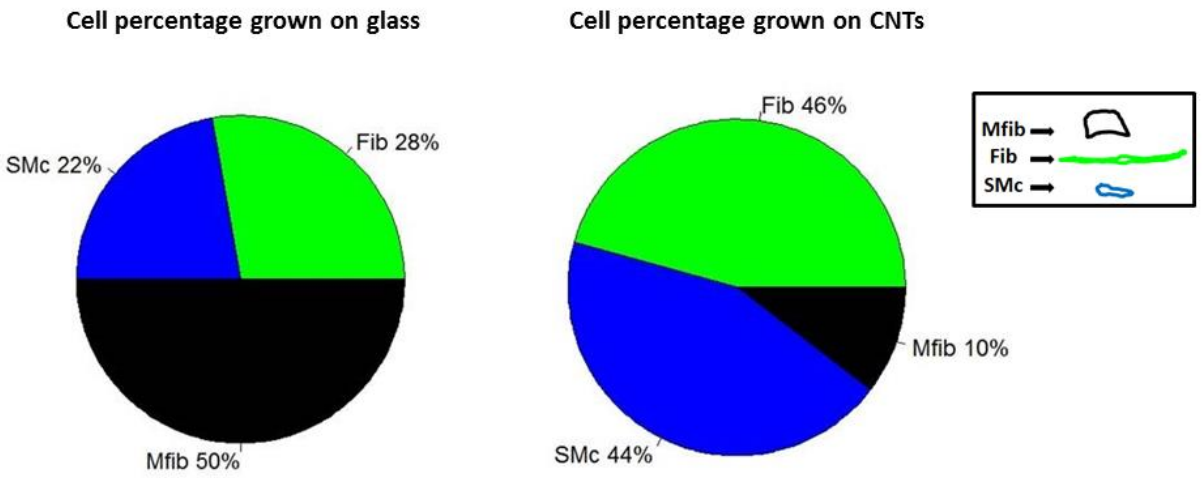

Figure 33: : *Morphological characterization of VICs phenotypes grown on control glass and CNTs substrates. Percentage of the three cell phenotypes (N=180) where evaluated.*

I tried to associate cell phenotypic variations, in terms of fibroblast percentage, to an evaluation of cell branching too (see Methods). Also in this case cell branching was quantified after 12 and 72 hours on both control and CNTs substrates. After 12 hours, there were any difference in cell branching between the two conditions, but after 72 hours on CNTs substrate cells appear more branched than on glass controls (Fig. 34). This result contributes to say that on CNTs there are more fibroblasts that on controls but the effect appears in a time dependent manner.

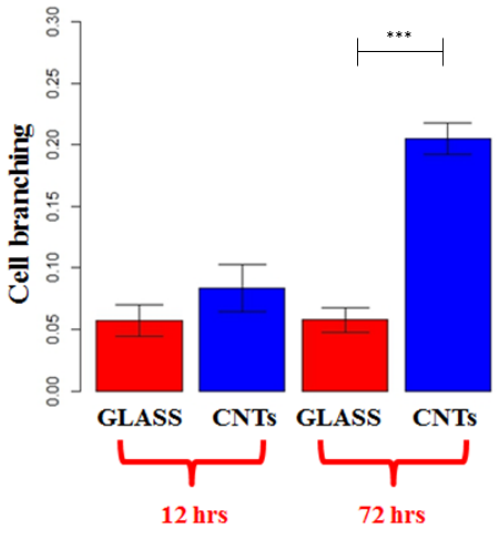

Figure 34: *Cell branching after 12-72 hours by seeding (T-test p<0.05=*, p<0.01=**,p<0.001=***, set=3, 25 fields for sets).*

7.3 Cell stiffness and role of focal adhesion points

As already introduced, aortic valve leaflets are characterized by a huge level of mechanical heterogeneity that is given to them by their peculiar layered structure [117,118]. As result of that, mechanical cross-talking between different regions of the leaflet could be one of the key factors in the onset of CAVD [117,118]. As an example of that, it has been shown that tissutal VICs elastic moduli are strongly influenced by the mechanical properties of surrounding ECM [8,80,125]. Intrigued by this consideration I wondered if a CNTs substrate have the ability to influence the mechanical properties of VICs in terms of cellular stiffness. I performed AFM force spectroscopy experiments on cells cultured on control glass and on CNTs after having immunohistochemically marked them with fluorescent dyes. This kind of measurements was possible thanks to the fact CNTs substrates we used were transparent and, consequently, fluorescent cells were easily recognizable by means of the inverted optical microscope above which our home-assembled AFM is mounted. In particular, in Figure 35, it is possible to see that the fibroblasts present on CNTs substrates are significantly stiffer than those grown on control glass substrates. Surprisingly, myofibroblasts grown on CNTs are, instead, softer than those grown on glass controls. Any difference is rather between smooth muscle cells grown on both substrates.

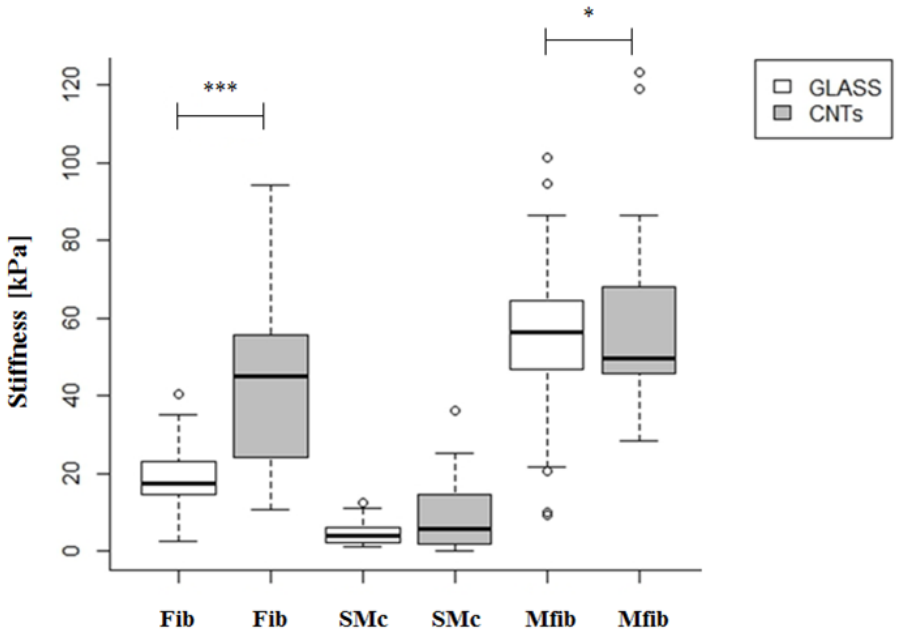

Figure 35: *Mechanical properties analysis of all the three pVICs phenotypes identified when grown on glass substrates and CNTs substrates (U-test p<0.05=*, p<0.01=**, p<0.001=***, set=5).*

The observed variations in the mechanical properties of fibroblasts and myofibroblasts were partially confirmed by literature from which these two phenotypes of cells result differently influenced by ECM variations [112]. In particular, I can speculate that more elongated is the shape (or lower is the surface exposed area), higher is the contribution of the carbonius nano-filaments composing CNTs substrates in perturbing, in particular increasing, pVICs stiffness. Following these surprising results from mechanical analysis, I evaluated whether there were variations in the number of focal adhesion points (FAs). FAs could be thought as the interaction points, through the plasma membrane, between the cell and the extracellular matrix components. It is well assured that their number and distribution is directly connected to the intracellular tensional state [195,196]. In order to quantify FAs, we carried out the immunofluorescence essays by labeling the vinculin (Fig. 36a-b, see Methods) on both control and CNTs substrates. Figure 36c shows the data summarizing our observations related to the analysis of the number of FAs. The evaluated number of FAs (Fig. 36c) confirms the cellular rigidity data (Fig. 35) pointing out a similar trend: the number of FAs in SMc and Mfib is not altered by CNTs, while Fib grown on CNTs present a larger number of FAs, presumably connected to a more effective transmission of load from the nanostructured substrate to the cell. Interestingly, if we consider

cell areas in both conditions (on tCNTs and on glass controls) we can see that any change is appreciable between Fib and SMc on both substrates while, from the other hand, a significant reduction in cell surface is appreciable in the case of Mfib grown on tCNTs (see Figure 36d). As consequence of that, we evaluated the density of FAs for every cell phenotype when interfaced or not to tCNTs (see Methods) (Figure 36e). Also in this case an extremely significant overexpression of FAs is observable on Fib while, from the other hand, Mfib when interfaced to CNTs shown just a slight, not significative, increase in FAs density. As consequence of such data, we can see that Fib cell phenotypes is strongly influenced in its mechanobiology by the underneath CNT carpet while Mfib cells not. Anyhow, in order to understand the exact mechanism subtending to this peculiar behavior more experiments are necessary.

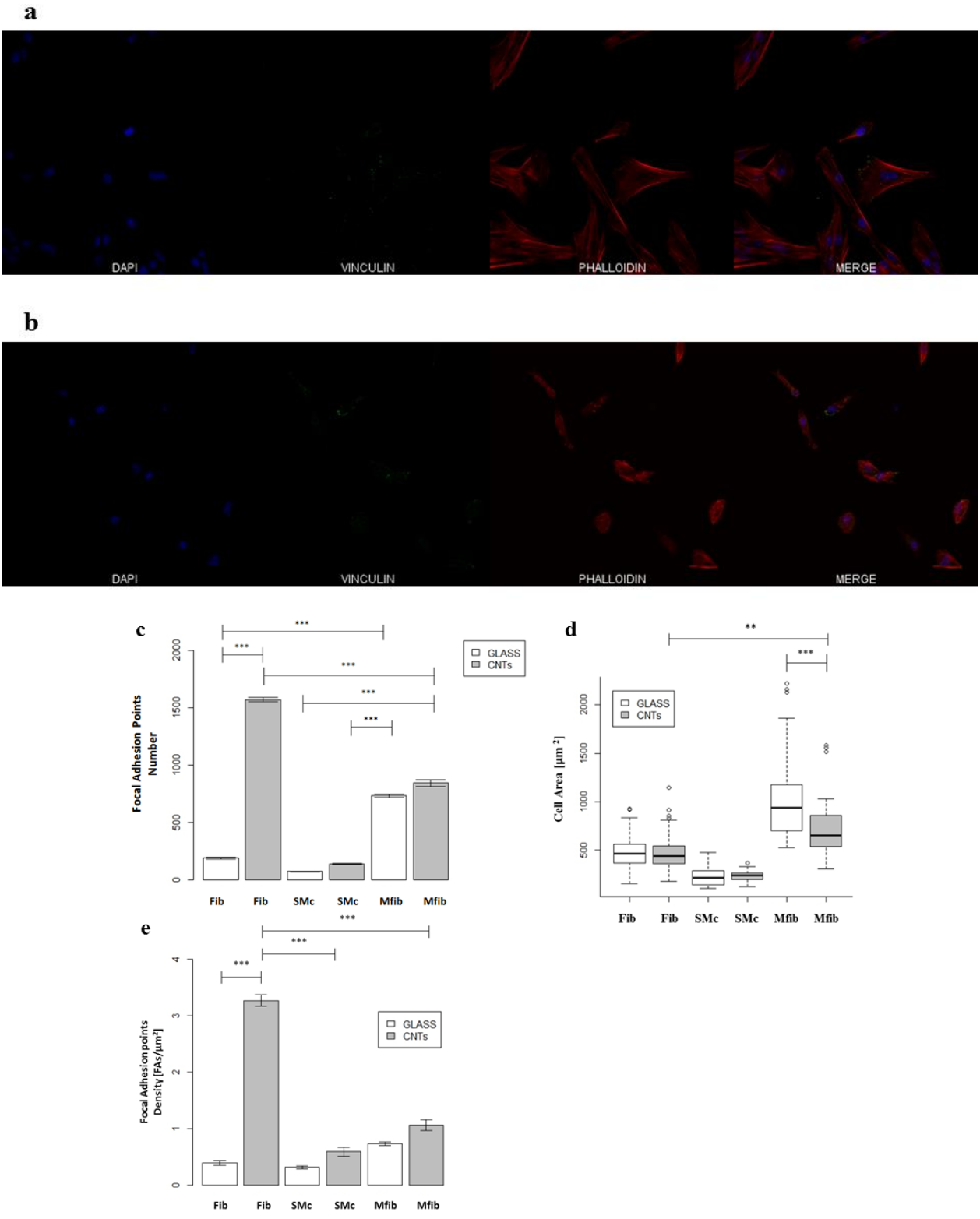

Figure 36: *Immunofluorescence images of VICs grown (a)on glass and (b)on CNTs (40X); (c)Focal adhesion points numbers; (d)Cell Area [µm^2]; (e)Focal adhesion points density. (T-test p<0.05=*, p<0.01=**,p<0.001=***, set=3, 25 fields for sets)*

7.4 A preliminary attempt to highlight the intimate interaction between a nanostructured CNTs substrate and the cell membrane

All the above findings could be, in principle, explained supposing a direct and intimate contribution of CNTs in regulating cell membrane processes and properties. In this scenario, I wondered which is, end eventually how could take place, the real interaction between cell plasma membrane and CNTs. Previous work by the group of Ballerini L. and co-workers had already hypothesized that a pinching phenomenon took place between plasma membrane and CNTs decorated substrates when neuronal cells are plated above them. In these experiments an increase in the electrophysiological activity of neuronal cells was explained in terms of cell-to-cell electrical shortcutting made by CNTs [172]. In order to evaluate if a similar phenomenon characterized my system too, we performed some preliminary study aiming in the visualization of the inner side of pVICs grown on flat glass controls or on nanostructured CNTs substrates. Cells were characterized on both substrates by means of AFM imaging performed in liquid environment after cells have been broken by osmotic shock [197] in order to expose the cytosolic side of the membrane (Fig. 37, refer to Methods for more details). In order to facilitate subsequent optical identification of cell membrane patches, we labeled the plasma membrane using the lipophilic membrane stain Dil (data not shown, but refer to Methods for more details about the procedure). Taking advantage of such staining we performed the AFM images on patches attached on both substrates (Fig. 37a-d). From line profiles shown in Figure 37c-f it is possible to see that the basal membrane patches lying on glass appear, as easily predictable, totally flat without any appreciable protrusion through it while the basal membrane adhering to the CNTs follows the nanostructured substrate morphology (Fig. 37d).

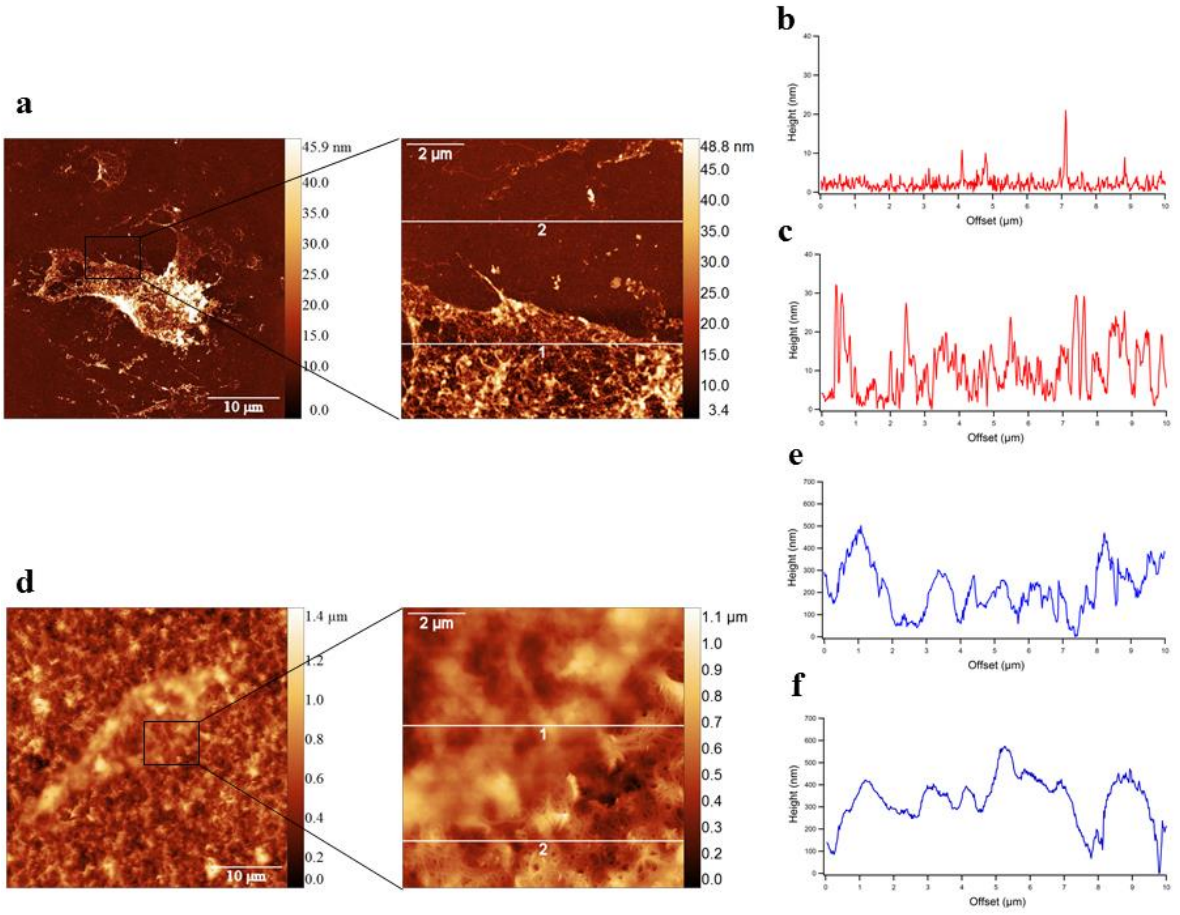

Figure 37: *Characterization of interaction between basal membrane and CNTs of VICs. AFM images of VICs basal membrane (a)on glass and (d)on CNTs with their respective line profile (c-f); (b)glass line profile; (e)CNTs line profile*

In order to highlight possible membrane piercing by the underneath substrate we prepared the same samples for electron microscopy investigation (see Methods). Figures 38a-b shows SEM images of pVICs basal membrane patches stuck on both substrates. In the enlarged image of Figure 38b, right, it is clearly visible how a CNT below the plasma membrane cross it completely (red arrow). Therefore, I can speculate that CNTs, piercing and pinching the cell membrane, could not only stabilize the bilayer [198] but, in some not yet clear way, promote the formation and/or clustering of focal adhesion points in pVICs grown on them (Fig. 36). Presumably as a consequence of that, a change in cell mechanical properties is observable too, in particular in terms of an increase in cell stiffness as pointed out by AFM force spectroscopy investigation I performed (Fig. 35).

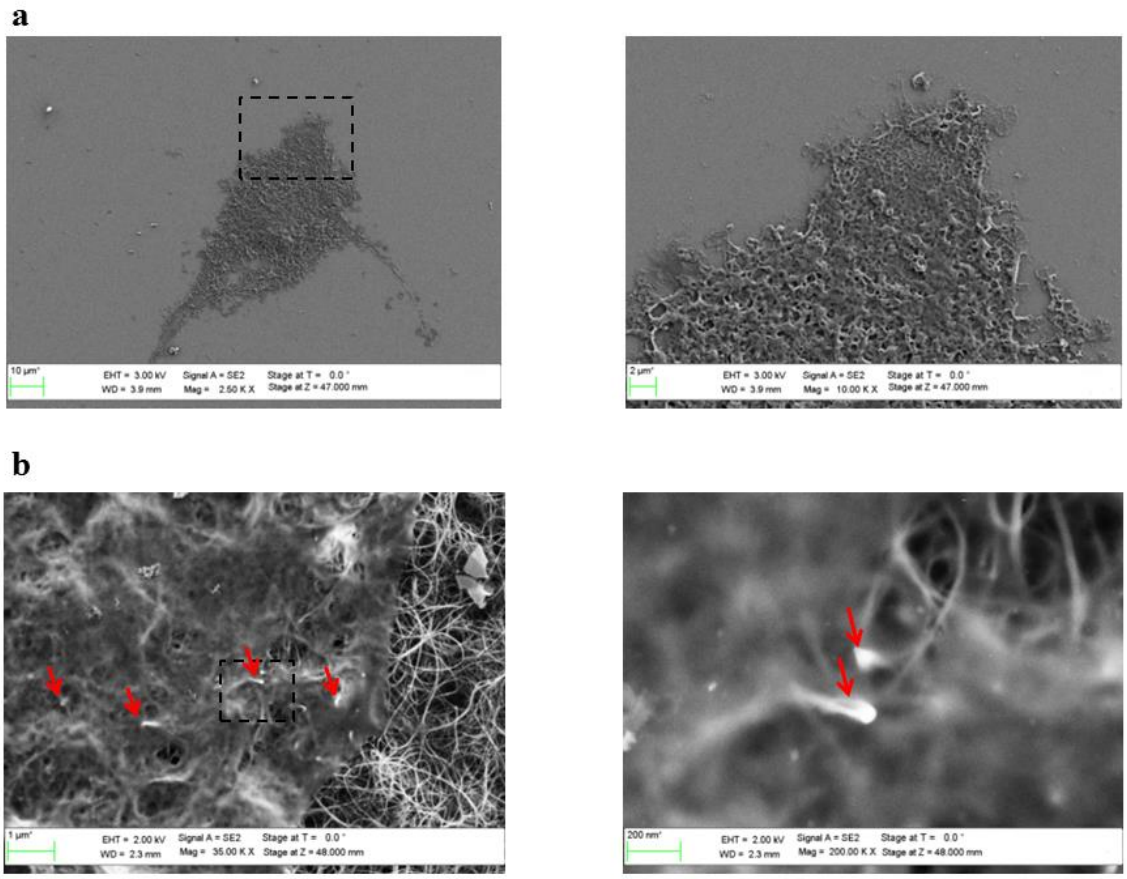

Figure 38: *Characterization of interaction between basal membrane and CNTs of VICs. SEM images of VICs basal membrane grown (a)on the glass and (b)on CNTs.*

8 Tumor associated p53 missense mutants

As previously reported, in last years, there was an increased interest in studying all ECM-connected biophysical processes in the onset and progression of cancer disease. In particular, it has been shown that the aggressiveness, invasiveness and the answer to chemotherapy treatments is strongly dependent on the biophysical properties of the extracellular matrix [81,137]. In this framework, I studied in collaboration with the Molecular Oncology Unit of Prof. G. Del Sal at the Laboratorio Nazionale CIB (LN-CIB) in Trieste, the tumor-associated p53 missense mutation focusing, in particular, on its effect on cellular processes and biochemical pathway involved in its mechanobiology. Has to be here noted that mutated p53 proteins become highly expressed in human cancers, reaching levels far above those observed in normal cells expressing wild-type p53 [199].The study, in particular, proposed to investigate the biochemical and molecular processes regulating the interaction between cells and the ECM pointing out cell mechanobiological perturbations.

8.1 *In vitro* cytoskeleton rearrangement of tumor associated p53 missense mutants

Initially, at the CIB laboratory, researchers have identified a class of drugs, called Statins, which proved to be able to reduce mutant p53 levels in MDA-MB231 cellular line. This class of drugs has already been clinically used to treat patients with cardiovascular disease lowering cholesterol plasma levels by mevalonate pathway inhibition [200]. Researchers proved that Statins, by inhibiting mevalonate pathway, reduce as well mutant p53 protein levels through post-transcriptional mechanisms. They have also demonstrated that protein geranylgeranylation is required for mutant p53 accumulation in cancer cells. In general, this process is responsible of the proteins anchorage in membranes [201].

RhoGTPases is the major geranylgaranyl transferase targets and the Statins have been found to inhibit the enzymatic activity of RhoA [202]. However, RhoA is involved in the antitumor activity of Statins and a target of mutant p53 in controlling cellular metabolism [200,202,203]. RhoA is also a regulator of actin cytoskeleton rearrangement and its activity is fundamental for the transmission of mechanical stimuli from (or through) the ECM to the cell [204]. Therefore we

hypothesized that mechanical perturbations, through the formation of stress fibers, could have an effect on mutant p53 levels by means of mevalonate/RhoA signaling. In order to confirm this hypothesis, I evaluated the stiffness of cells treated with different drugs. In particular, I evaluated mechanobiological properties of cells treated with Zoledronate (ZOL – a bisphosphonate that plays an important role in the treatment of breast cancer, mainly in patients with bone metastasis [205]), Cerivastatin (CER – a synthetic member of the class of statins used to lower cholesterol and prevent cardiovascular diseases), CER in combination with geranylgeranyl pyrophosphate (CER+GGPP), Blebbistatin (BLEB – a myosin inhibitor mostly specific for myosin II) and Y27632 (Y – a Rho-associated kinase ROCK inhibitor). All these conditions were compared to the stiffness of not-treated control cells (NT). In Figure 39a it is shown that zoledronate (in red) and statin (in green) treatment induce a significant reduction in cell stiffness. This reduction in stiffness could be associated to an actin cytoskeleton de-structuration. In fact, a similar effect could be observed in cells treated with Blebbistatin (in orange) or with a the ROCK inhibitor Y27632 (in violet) (Fig. 39a). Interestingly, geranylgeranyl pyrophosphate (GGPP, in blue) revealed to be able to reverse CER statin treatment by inducing a cellular mechanoresponse comparable to untreated cell stiffness. In parallel to my mechanobiological investigation, at CIB laboratory researchers have evaluated whether the disruption of the actin cytoskeleton could have an impact on mutant p53 levels. They treated cells with Latrunculin A, a bioactive 2-thiazolidinone macrolide derived from sponges that, sequestering G-actin and preventing F-actin assembly, induces actin cytoskeletal filaments disruption and is used to study cell functions in vitro (e.g., migration, endocytosis) and in vivo (e.g., tumor cell invasion). After Latrunculin A treatment cells were stained for F-actin and p53 (Fig. 39b). As shown in Figure 39b Latrunculin A determines a reduction of stress fibers (red channel) and a concomitant reduction of mutant p53 levels (green channel). These results suggest that RhoA-dependent acto-myosin dynamics impact mutant p53 levels in the tumor cells.

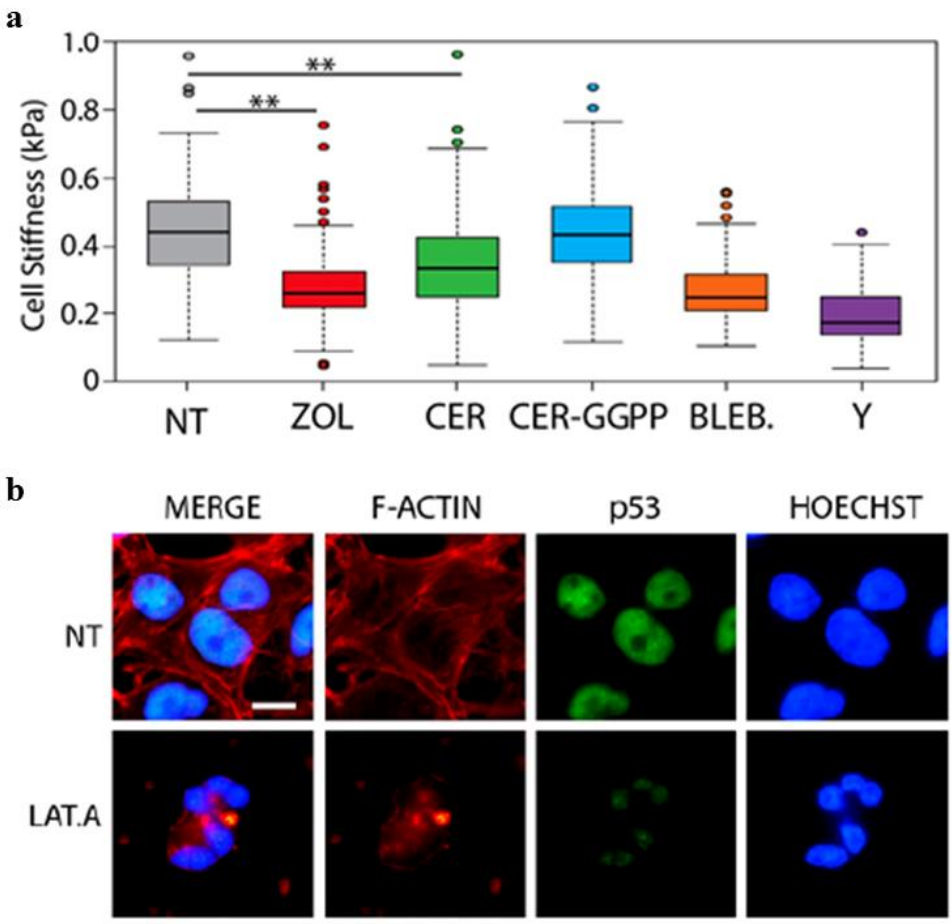

Figure 39: *Variations of mechanical properties control mutant p53 levels and activity via RhoA/actin cytoskeleton in vitro: (a)Cell stiffness, quantified by means of AFM force spectroscopy, relative to not-treated (NT), cell treated with zoledronic acid (ZOL) 50 μM, cerivastatin (CER) 10 μM alone, CER in combination with geranylgeranyl pyrophosphate (CER+GGPP) 20 μM for 48 hrs. Blebbistatin (BLEB.) 50 μM and Y27632 (Y) 50 μM were used as control (**p<0.001, Mann–Whitney U test); (b)Immunofluorescence analysis of MDA-MB 231 cells treated with Lantrinculin A 0.5 μM (LAT_A) for 48 hrs was performed with indicated antibodies. Scale bar 15 μm*

8.2 *Ex vivo* cytoskeleton rearrangement of tumor associated p53 missense mutants

As natural evolution of the characterization I performed *in vitro*, I extended the methodology to ex-vivo systems taking advantage of AFM force-spectroscopy capability to estimating the role of the mevalonate pathway in tumor mechano-signaling and, consequently, to have an idea of the potential effects of a perturbation of this pathway on mutant p53 accumulation *in vivo*. In order to

investigate this effects, tumor tissue slices were carved out from mice breasts after orthotopically injection of zoledronic acid. Slices were subsequently mounted on the AFM and characterized. From AFM analysis, shown in Figure 40a, the Zoledonic acid treatment reduces the stiffness of both cancer cells and of the ECM within the tumor. These results were confirmed by the molecular analysis carried out at CIB laboratories. They, in fact, demonstrated of phosphorylation of focal adhesion kinase (pFAK residue Tyr397) and of myosin light chain 2 (pMLC2 residue Ser19), mutant p53 levels. As shown in Figure 40b there is a reduction of both mechano-signaling markers and p53 mutant levels. These data confirm that the mevalonate pathway is strongly involved in tumor mechanosensing and provides an evidence of its possible role in regulating mutant p53 levels also *in vivo*.

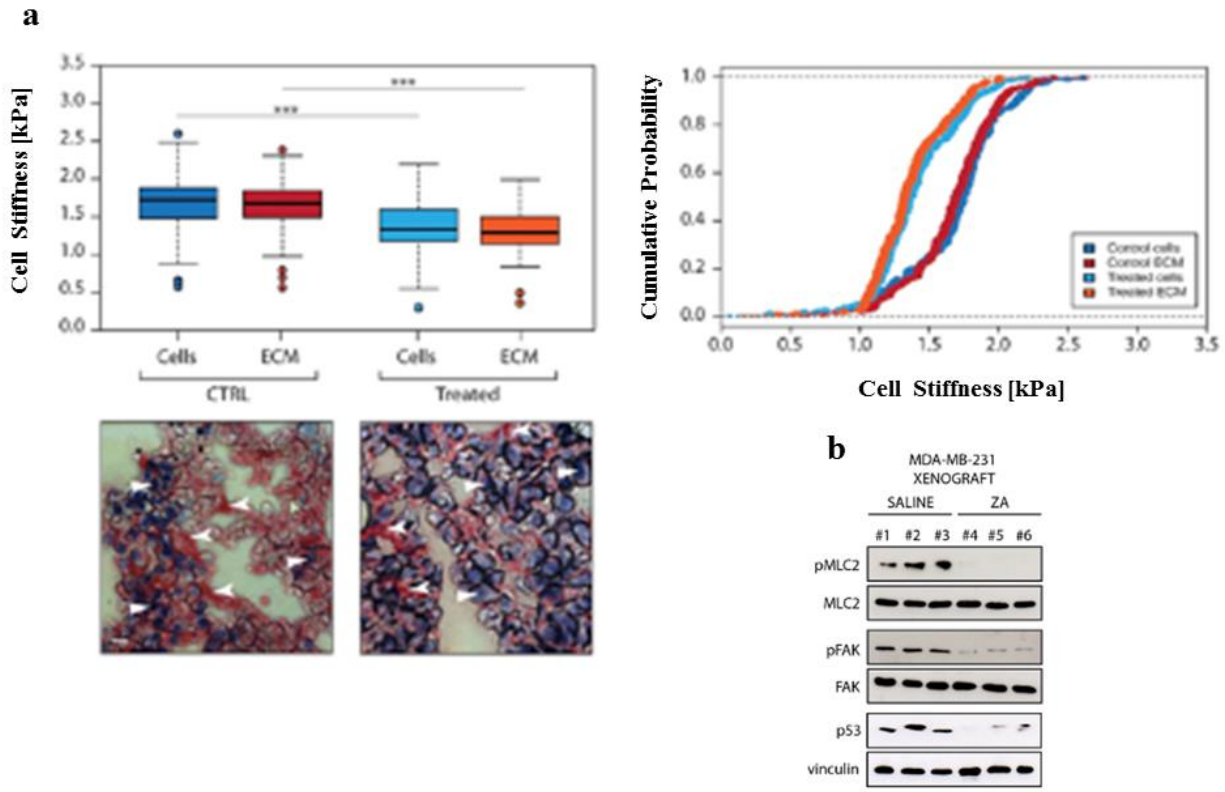

Figure 40: *Variations of mechanical properties control mutant p53 levels and activity via RhoA/actin cytoskeleton in vivo: (a)Tumor tissue stiffness was evaluated in control (CTRL) and zoledronic acid treated (Treated) samples. On the left panel: Box-plot of stiffness values from the cells and the extracellular matrix (ECM) composing the CTRL and the treated samples. On the right panel: cumulative probability of cell and ECM stiffness of CTRL and Treated samples ($p<0.001$ in bothcases, Kolmogorov-Smirnov test; n=4). Bottom: Representative image of tumor samples used to measure cell and ECM stiffness. Hematoxylin and PicroSirius staining were used to discriminate between cellular and ECM phase for atomic force microscopy (AFM) on both controls (left image) and treated samples (right image). Straight arrows indicate cells, while concave arrows indicate the ECM phase. Four mice per group were used. Scale bar 15 μm; (b)Lysates of MDA-MB 231 derived xenograft tumors from control (saline) or zoledronic acid (ZA) treated mice were analyzed by western blot with the indicated antibodies.*

9 In vitro myogenesis induced by Human Recombinant Elastin-Like Proteins

The vertebrate skeletal musculature is an extremely complex organ system, composed of functionally discrete units generated by a series of specific morphogenetic events during embryogenesis [151]. Myogenesis, the process of generating muscle, was highly studied over the last decades and particular effort was made in order to design and fabricate materials able to induce or facilitate skeletal muscle regeneration [159]. In this framework, I was involved by the groups of Dr. P. D'Andrea and Dr. A. Bandiera from the University of Trieste, in the characterization of a new class of biomimetic peptide-based materials called Human Elastin-Like Polypeptides (HELPs) [84,168]. In particular, the team at the University engineered and synthesized different polypeptide that were subsequently deposited on common cell-culture glass slides in order to add new myogenetic functionalities to the substrates. Before cell plating I characterized the different substrates in terms of morphology at the nanoscale and in terms of stiffness by means of atomic force microscopy. The same technique was subsequently used as well to evaluate the morphology and the stiffness of the cells developed above the different materials.

9.1 Characterization of Human Recombinant Elastin-Like Proteins coating

For this study, a novel polypeptide named HELPc was synthesized by fusing, at its C-terminal, a sequence from the a2 isoform of collagen type IV, containing two Arg-Gly-Asp (RGD) motives. We employed HELPc, as well as two poly-peptides of the same HELP family (HELP and HELP1) [166], as adhesion substrates for C2C12 myoblasts, cells widely employed in differentiation studies, and able to sum-up, in vitro, most of the molecular events leading to the development of contractile myofibers [206]. To characterize the effects induced by the different HELP substrates, cell adhesion, survival, proliferation and cell differentiation were compared by combining several experimental approaches, among which immunofluorescence, calcium imaging and, concerning me more closely, atomic force microscopy for imaging and mechanical characterization. In Figure 41 schematic of HELP family polypeptide structure and synthesis (carried out at the University of Trieste) is shown. HELPs coatings were obtained by depositing 0.1 mg/mL. About 0.1 mL of coating solution was used per 1 cm^2 surface area, thus resulting in

10 mg polypeptide/cm^2. Coating solution was allowed to dry in a tissue culture hood and cells were seeded directly on the polypeptide surface. After 48 hours at 37 °C in a CO_2 incubator cells were processed for subsequent characterization.

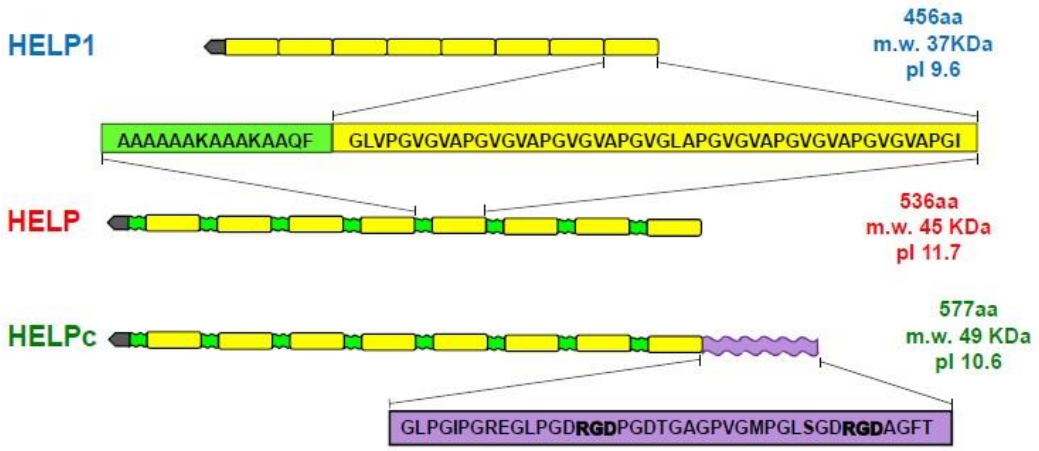

Figure 41: *HELP biopolymer structures: At N-terminal portion of each polypeptides is positioned a His-tag sequence (dark gray). HELP1 is formed by eight repetitions of hydrophobic domains (yellow). HELP backbone is composed of cross-linking (green) and hydrophobic domains repeated eight times. HELPc is formed by fusing of HELP structure with a sequence of α2 chain of the type IV collagen (purple) at the C-terminal.*

Morphological data about HELP and HELP1 were in agreement with previous AFM topographic images acquired by Bandiera A. and co-workers in previous works [207]. In this work they shown surfaces characterized by regions with fibrillar-like formations in HELP samples and areas with amorphous topology in HELP1 samples [207]. A similar approach was followed by me in order to characterize the topography of HELPc surface. In Figure 42a it is evident the existence above the flat glass substrate of an amorphous topology associable to the protein assembles [208,209].In order to determine the thickness of HELPc coating, I removed the polypeptide film on a 1×1 μm^2 portion of the sample doing a high force scan with the AFM tip (Fig. 42b). The so obtained square hole has allowed us to carry out height distribution analysis of all the image obtaining data representative of the upper part of the film and data representative of the underling glass substrate: these data were in agreement with a coating thickness calculated previously as the height difference between the film upper surface and the underneath glass surface after a scratch done with a scalpel (15.7±1.1nm).

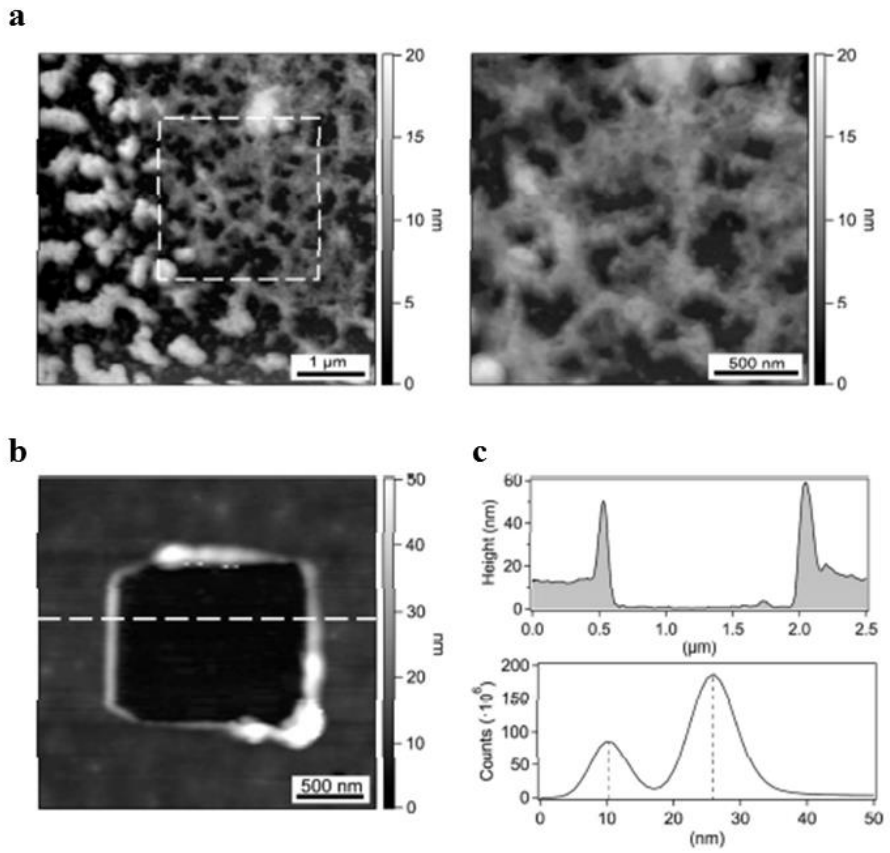

Figure 42: *AFM characterization of HELPc coating: (a)topographic images of HELPc surface measured in air. At the right the magnification of the image portion; (b)AFM topography image of a portion of HELPc film which was removed shaving it away with the AFM tip. The shaving and the scanning image were realized with same tip, this reduced the resolution. (c)at the top, the line profile corresponding to the line pointed out in (b) while, at the bottom, the height distribution of the same image which allows precise film height determination (15.7±1.1 nm in the shown example).*

9.2 Myotubes stiffness and cytoskeleton rearrangement on HELP coatings

After the morphological characterization and thickness determination of HELP coatings, in strong collaboration with the research team of the University of Trieste, I evaluated the adhesion, differentiation and metabolic properties of C2C12 cell lines when developed above such different films. The results obtained indicate that HELPc improves myoblasts adhesion, differentiation and fusion, without stimulating human polymorphonuclear (PMN) leukocytes activation when compared to the other two polypeptides (HELP and HELP1). As an example, Figure 43 shows an immunofluorescence experiment where a different number and distribution of focal adhesion

points (via a Vinculin staining) and actin organization (via a Phalloidin staining) was observed in C2C12 cells grown on glass controls and on the three different HELP substrates.

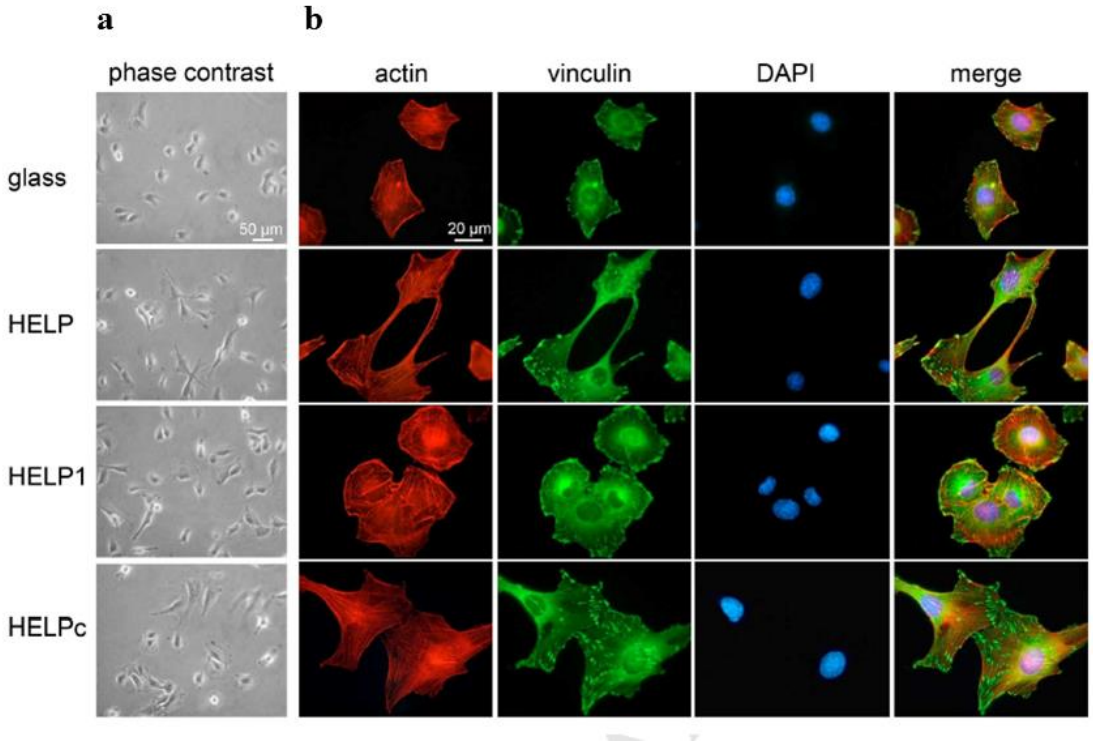

Figure 43: *Phase contrast and immunofluorescence study of cells adhesion and morphology: (a)Phase contrast images of C2C12 cells; (b)Immunofluorescence images of actin cytoskeleton and focal adhesion points (red= Phalloidin; green= vinculin; blue= DAPI; n=3). Images acquired in collaboration with Dr. Paola D'Andrea, University of Trieste, Italy.*

Starting from our knowledge that *in vitro* a phenotypic changes of C2C12 myoblasts could be accompanied by a progressive increase in cell stiffness coupled to an increased expression of contractile proteins [210] we hypothesized that also in our system variations of cell mechanical properties could be determined by the cell-supporting microenvironment. To verify this assumption I exploited AFM force-spectroscopy capabilities to compare the mechanical properties, in terms of cellular stiffness, of myotubes grown on the three different HELP substrates. I performed the measurements after 3 days of differentiation (see Methods), and the elastic modulus of myotubes developed on glass resulted to be 49.69 ± 4.19 kPa (68 force-indentation curves, n = 4) resulting stiffer than those grown on HELP (16.49 ± 1.12 kPa, 69 force-indentation curves, n = 4) and on HELP1 (27.93 ± 2.24 kPa, 61 force-indentation curves, n

= 4). Interestingly, any significant difference was measured between the myotubes grown on glass and those grown on HELPc (47.06 ± 2.34 kPa, 66 force-indentation curves, n = 4) as pointed out in Figure 44b.

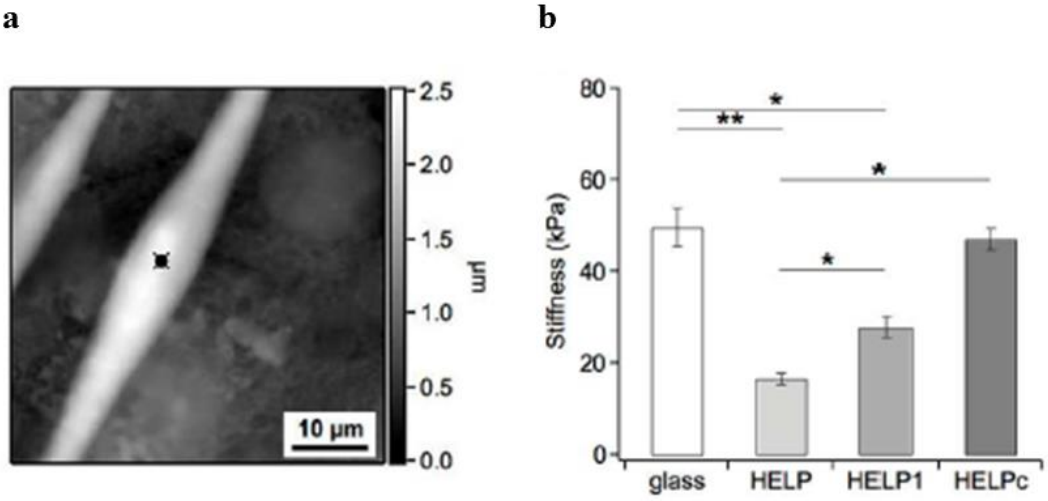

Figure 44: *AFM mechanical characterization of myotubes cells: (a)Example of AFM 3D reconstruction of myotube cell. The black spot on the enlarged cellular portion represents the location where force spectroscopy curves were acquired; (b)Elastic moduli of cells grown on glass and HELP substrates. (* = p< 0.05; ** = p<0.01; T-test).*

In parallel to the AFM mechanobiological investigation of myotube cells, in collaboration with Dr. P. D'Andrea from the University of Trieste, I evaluated as well the contraction activity of C2C1s cells when grown on HELPs substrates.

Video microscopy and Ca^{2+} measurements were carried out at room temperature. Fura-2 loaded coverslips were mounted on the stage of an inverted microscope and visualized with an oil immersion 40× objective (1.3 NA). Cells were excited at wavelengths between 340 and 380 nm with a monochromator device and fluorescence signal at wavelengths larger than 510 nm collected at 1 Hz. Ratiometric Ca^{2+} maps were obtained by computing the ratio of 340/380 nm excitation wavelength values. Cell depolarization was obtained by perfusing the cells with a solution 60 mM KCl. Intracellular Ca2þ transients were considered significant if they exceeded five times the SD of the baseline noise. The frequency distribution of spontaneous Ca^{2+} sparks in C2C12 cells adhering to HELP polypeptides are reported in Figure 45. Although variable (histograms represent means ± standard error), the onset of sparks was time-dependently

stimulated by cell adhesion on HELP and HELPc. The latter polypeptide, in particular, stimulated sparks appearance more than two-fold with respect to HELP (days 4 and 5). Interestingly, Ca^{2+} sparks could be observed very infrequently in cells adhering on HELP1.

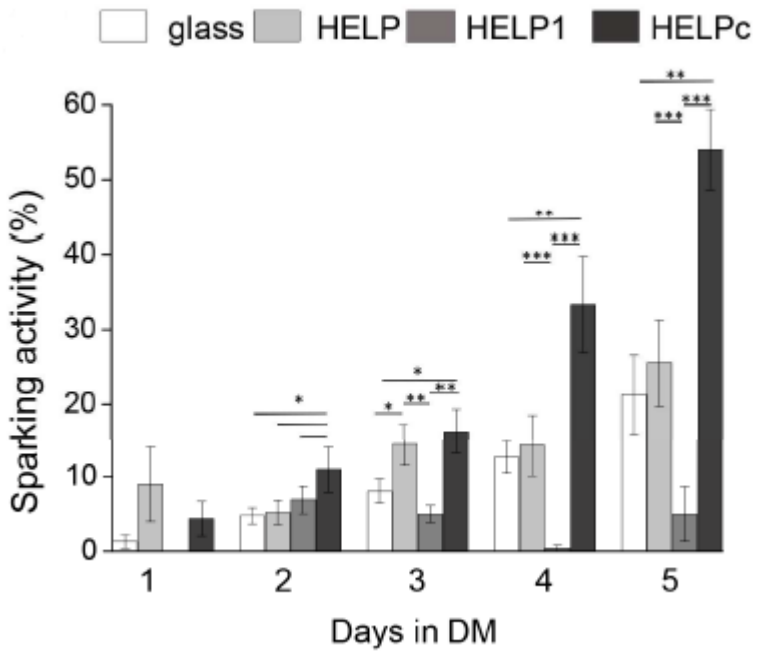

Figure 45: *Calcium imaging of spontaneous Ca^{2+} sparks: Frequency distribution of spontaneous Ca^{2+} sparks recorded at different days of differentiation (* = p< 0.05; ** = p<0.01; ***=p<0.001; T-test).*

These results demonstrate that cells grown on HELPc contract more than those grown on HELP and HELP1. Thus, summarizing, HELP family of polypeptides, but in particular the HELPc member, represents an emerging tool for studies probing the functional consequences of cell-biomaterial interactions and a promising starting point to develop new biomaterials for muscle regeneration.

9.3 Characterization of Human Recombinant Elastin-Like Protein gel

The biochemical, mechanical and topographic properties of the extracellular matrix are crucially involved in determining skeletal muscle cell morphogenesis, proliferation and differentiation. The human elastin-like polypeptides (HELPs) described in the previous section are recombinant biomimetic proteins specifically designed to mimic the properties of the native matrix protein and, when employed as myoblast adhesion substrates, they seem able to stimulate in vitro myogenesis. Given that we started investigating the effect of HELP hydrogels on myoblasts viability and functionality. To exploit this aspect C2C12 cells were cultured on HELPc hydrogels at different monomer concentration, with the aim of coupling the biochemical properties of HELPc polypeptide with the mechanical features of hydrogels. By comparing the responses of C2C12 cells seeded on HELPc hydrogels or on non-cross-linked HELPc glass coatings, some intriguing differences in cell adhesion, morphology, proliferation and differentiation were pointed out, indicating that HELPc hydrogels can be employed as tools for testing the physiological consequences of cell–biomaterial interactions. To obtain hydrogels, the enzymatic cross-linking of the HELPc was obtained by transglutaminase thanks to the Gln and Lys residues of HELP hydrophilic sequence. Both non-cross-linked HELPc glass coatings and cross-linked HELPc hydrogels were used as adhesion substrates for C2C12 cells. At the University of Trieste were obtained hydrogels starting from polypeptide solutions of, respectively, 5% and 7% w/v in 10 mM Tris/HCl. These concentrations were selected due to the fact lower concentrations systematically failed in generating a stable hydrogel, while concentrations higher than 7% w/v have the tendency to give solubility problem. Inside this framework I carried out the AFM surface characterization of both 5% and 7% substrates (Fig. 46a-b). AFM imaging reveals similar morphology for the two samples but, surprisingly, different from the previously data I obtained for HELPc coatings. This could be presumably due to some different synthesis mechanism involved in HELPc hydrogel glass layering. I quantify the roughness of the 5% HELPc hydrogel (R_a= 60.8±3.2 nm) and 7% hydrogel (R_a= 32.5±2.4 nm). As already described, in order to measure hydrogel thickness, I made a scratch in it exposing the underneath supporting glass surface. Height evaluation reveals that the 7% samples were significantly thicker than the 5% (3.702 ± 1.431 μm vs. 1.583 ± 0.446 μm) (Fig. 46c).

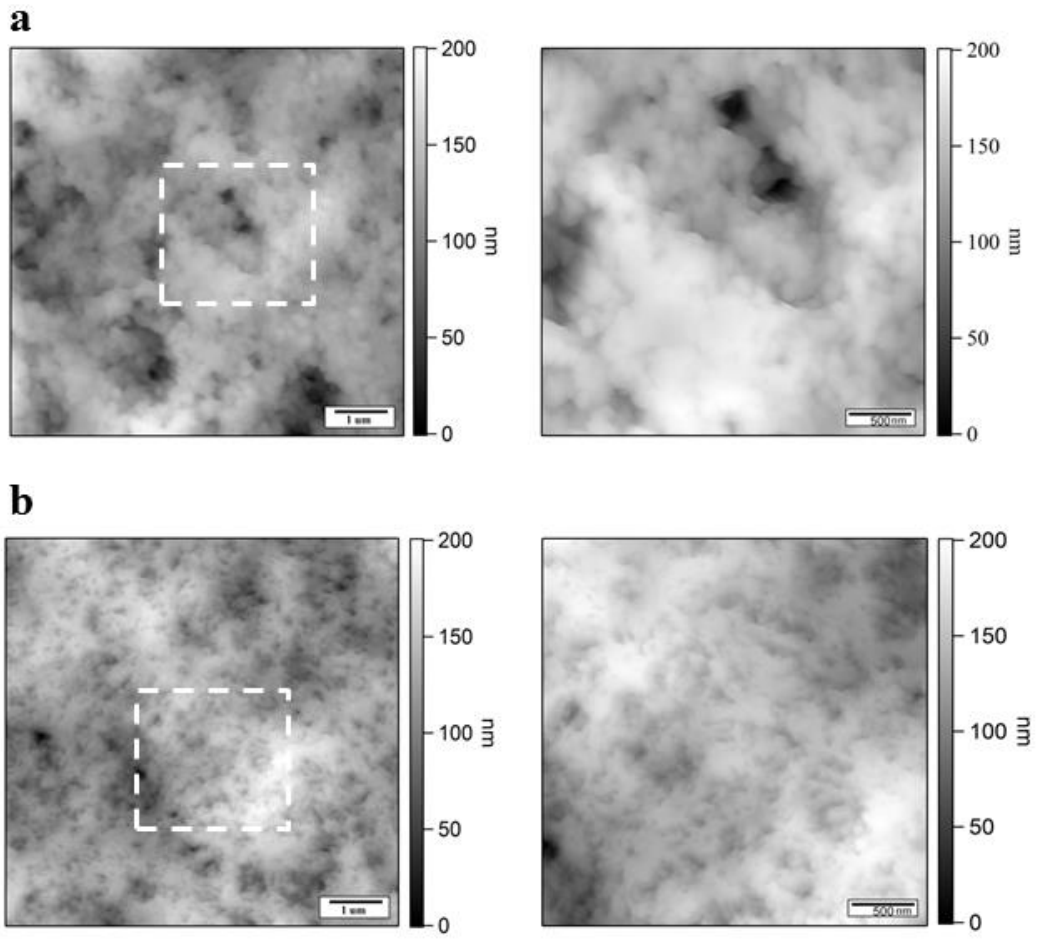

Sample	Height (um)
HELPc 5%	1.583 ± 0.446
HELPc 7%	3.702 ± 1.431

Figure 46: *AFM characterization of HELPc hydrogels: (a) topographic images of 5% HELPc hydrogel surface measured in air. At the right the magnification of the image portion; (b) topographic images of 7% HELPc hydrogel surface measured in air. At the right the magnification of the image portion (c) Height of HELPc hydrogels.*

In parallel to this surface characterization, by comparing cell adhesion, proliferation and differentiation, several striking differences were pointed out between the different HELP compositions tested. In fact, depending on support rigidity, measured by means of rheological

measurements, adhesion to HELPc substrates dictated cell morphology, spreading, focal adhesion formation and cytoskeletal organization.

Summarizing, hydrogels show to greatly stimulate cell proliferation, in particular in low-serum medium conditions, and partially inhibit myogenic differentiation. On the whole, the results underline the potential of HELP family polypeptides as a tool for dissecting crucial steps in myogenesis.

Discussion

In the last decades, it has been shown a strong correlation between cell biomechanics and variations in the mechanical properties of the extracellular matrix. Mechanical stimuli mutually exchanged between adjacent cells or between a cell and the surrounding extra-cellular environment activate specific biochemical and biological functions which, finally, could result in a change of the mechanobiological properties of the cell [42]. These variations could be studied in a biomedical context *via* the determination of the Young's modulus characterizing single cells or an entire tissue portion, with the final purpose to correlate them to human diseases or abnormalities. The increased interest in quantify the mechanical properties of biological species, has encouraged the exploitation of flexible nanotechnological tools and techniques such as the Atomic Force Microscope (AFM). In this thesis work I have took advantage of AFM versatility either to acquire high-resolution topographic images of the sample three-dimensional morphology or to quantify the mechanical properties of cells, tissues and substrates performing force-spectroscopy investigations. As has been described in previous paragraphs of my thesis, the AFM-based technique to investigate sample compliance has the great advantage of being able to apply a very broad range of forces (from 1 pN to 1 μN) allowing to study and compare substrates characterized by a wide spectrum of rigidities. Moreover, AFM is able to work in both liquid or air conditions and, very important when dealing with cells and tissues, samples do not require any special treatments before the measurement. Herein, along this thesis, AFM has been used to study mechanobiology and mechanotransduction in three different cellular system: calcific aortic valve disease, tumor associated p53 missense mutant and myogenesis.

Calcific Aortic Valve Disease

Calcific Aortic Valve Disease is the most common form of valve disease in Western world and represents a major healthcare burden. The progression of this disease is influenced by the mechanical forces to which are exposed valvular interstitial cells embedded within the valve matrix and, importantly, by the significant changes in morphology, composition and mechanical properties of the surrounding extra-cellular matrix [122]. VICs have been extensively described in the framework of the thesis as valve mechanosensors, able to respond to different matrix stiffness and/or cyclic elongation either in 2D or 3D culture conditions in numerous studies

[122,211]. Here, in particular, I studied the mechanical, morphological and molecular properties of VICs grown on substrate characterized by different surface chemistry, morphological and/or mechanical properties, which will at the end mimic a condition similar to the valve ECM structure, this in order to highlight matrix contribution and role on regulating VICs cellular fate in the onset of calcified tissue formation.

Initially I was focused on the changes of mechanical properties in human valve interstitial cells grown on the flat elastomeric substrates characterized by different stiffness. To this aim, we manufactured simple 2D polyacrylamide gels [212,213] with four, AFM-validated, stiffness values in the kPa range (Fig. 17). Therefore, I evaluated the contribution of substrate rigidity on hVICs morphology pointed out that α-SMA and F-actin co-localization is function of cell rigidity and, moreover, from a morphological point of view, cellular perimeter, area and shape were all affected by substrates rigidity (Fig. 18). Having well in mind the strong relationship existing between loads exerted on cells, polymerization dynamics of the F-actin cytoskeleton component and focal adhesion points formation [24], I had the intuition that there could be a variation in cellular rigidity determined by the substrate stiffness. Interestingly, when I measured the cell stiffness by means of AFM, cell stiffness raised as direct function of cell substrate rigidity. This hypothesis was also supported by the significant increase in number and density of focal adhesion points characterized by well-defined shapes on the more rigid substrates than on the softer ones (Fig. 19). Moreover, It has been found, in many other different cellular system as well, that the mechanical stress regulates YAP nuclear localization through the Hippo kinase pathway [44]. Therefore, when cells are plated and left to develop onto stiff substrates, the mechanical engagement of the cellular cytoskeleton determines in the cell a tension-dependent inactivation of the kinase responsible of YAP phosphorylation, thereby causing its nuclear sequestering [57] and an upregulation of its target genes [214]. Based on this knowledge I evaluated an eventual YAP localization in the nucleus of our cells trying to understand if a dependence on the rigidity of the substrate was present (Fig. 20). What I discovered is that the trend in the percentage of YAP nuclear location (Fig. 20b) is perfectly in agreement with cellular rigidity (Fig. 19b), area and perimeter (Fig. 18b-c) trends. This let me to hypothesize that, regarding the mechanical response of human VICs in the natural matrix environment, could be that: i) we can associate undetectable, or at least very low, levels of YAP activation in cells developed on substrates of stiffness values lower than ~18 kPa; ii) a rapid increase in the YAP activation level in cells developed above a

compliance range of substrate stiffness between ~18 kPa and ~28 kPa; iii) a saturation of the mechanical-dependent machinery promoting YAP nuclear shuttling starting from stiffness values around ~60 kPa. In order to evaluate if, effectively, the YAP-dependent gene expression takes place and if this process is reversible, I moved my attention (and studies) on a condition inducing a high cellular stress by seeding hVICs on a glass substrate which revealed to be very similar, from the molecular and the mechanical aspects, to the condition I found on the High stiffness PAAg substrate. Therefore, I simulated the low rigidity condition taking advantage of pharmacological inhibition of rho-associated protein kinase ROCK signaling pathway using the Y27632 drug. This treatment induced in cells a localization of YAP (Fig. 21a) similar of what was observed seeding cells on a soft surface (Fig. 20a) and YAP nuclear translocation is due to YAPSer127 phosphorylation inhibition [215]. Interestingly, I have demonstrated that the process is completely reversible (Fig. 21b) and reflects into reversible inhibition of canonical targets (Fig. 22). Actin filaments response to the external forces seems, through a filaments rearrangement process, to determine and regulate the variation in the cell mechanical properties I observed [18]. In this direction, integrity of the actin cytoskeleton and the amount of stress fibers play an important role in the activation and nuclear translocation of YAP-TAZ complex [8]. The Y27632 inhibitor inactivates the rho kinase impeding, in this way, actin polymerization by reducing cellular tension [44]. Therefore, I hypothesized that the pharmacological inhibitor treatment induced an inhibitory effect also on hVICs stiffness. Surprisingly, when I measured the cellular stiffness *via* AFM, I could observe that the Y27632 inhibiting effect did not take place immediately after the molecular/chemical treatment but, instead, the reduction in cellular stiffness on hVICs appeared just after 24 hours. Interestingly, if I removed the inhibitor *via* washing out, an effective stiffness recovery in cell took place just after 48 hours (Fig. 23). In this context, it was interesting to note that the ACTA-2 gene, encoding for the αSMA gene product, and known to contain a promoter sequences available for multiple binding of transcription factors including the YAP/TAZ complex-binding TEAD [216,217], was also reversibly inhibited by the Y27632 treatment (Fig. 24) with a trend very similar to the amount of YAP's target genes (Fig. 22). These last results allowed me to say that the effect induced by mechanical stress is effectively reversible, but the mechanical recovery of cytoskeleton rearrangement takes place more slowly than the molecular recovery. This hypothesis needs to be supported by further experiments also in the light of recent results showing that Rho/ROCK role in actin dynamics is independent of YAP

activity but, form the other hand, a Rho/ROCK transcription factor downstream is necessary to regulate FAs formation and cell–matrix interaction [218]. Matrix stiffening is a hallmark of pathology progression in various diseases such mammary and liver tumor development [219,220]. A typical example in the cardiovascular system is the matrix stiffening that occurs, in parallel to YAP transcriptional activation, in cardiac fibrosis [221]. Since pathologic evolution of the valve tissue occurs likely through a progressive change in the compliance of the matrix [122], variation of VICs stiffness sensitivity may lead to pathologic activation of the cells that may, at first, progress into myofibroblast differentiation and then evolve into mineralized matrix depositing cells [116]. On the basis of this, I sought to translate to an *ex vivo* experimental model the evidences described until now for *in vitro* systems. To achieve this goal, I used a thin transversal sections of explanted stenotic calcific human valves, obtained from patients that underwent aortic valve replacement. Therefore, I evaluated the expression of YAP into Vimentin+ and αSMA+ cells (Fig. 26) and investigated the leaflets stiffness via AFM (Fig. 25). It was interesting to note that the stiffness values characterizing non-calcific portions (Fig. 25c) were in line with the reported literature on healthy valve matrix compliance [222] while, form the other hand, calcified regions showed a preferential YAP-nuclear localization coupled to an increase of tissue-realted stiffness (Fig. 26).

As I have already stated, Calcific Aortic Valve Disease induction and progression are influenced, not only by changes in the mechanical properties of the ECM, but also by its micro-and nano-morphology and chemical7molecular composition [122]. In recent years, the quest for biocompatible materials capable of mimicking the natural ECM for tissue regeneration has increased. Of particular interest are nano-and micro-structured three-dimensional porous scaffolds which could favor cell adhesion, proliferation and migration and are capable, at the end, to regulate cellular network functionality [223,224]. In this scenario, CNTs are optimal candidates, showing dimensions and morphology comparable to fibril ECM constituents, *in vitro* and *in vivo* cellular biocompatibility, outstanding electrical conductivity and ease of chemical functionalization to add any required functionality [225,226]. Based on this information, in order to study as these interface with porcine valve interstitial cells (pVICs), I choose to take advantage of the multi-walled carbon nanotubes carpets directly grown on supporting glass slides that were developed in our laboratory. In short, a novel strategy to grow via chemical vapor deposition (CVD) CNTs on a glass slide was developed and optimized. Thanks to the final transparency of

such CNT substrates, for the first time, I could carry out togheter immunofluorescence experiments and cell stiffness analysis via AFM. In addition, from the mechanical analysis of CNTs carpets I used (Fig. 27), I discovered that my CNTs carpet were characterized by a stiffness very close to that found on Middle-High and Middle Low polyacrylamide gels (Fig. 17b). This was an important point because, as already described, this stiffness has demonstrated to have any effect on cells, maintaining them in a sort of "quiescent state". The relevance of this "neutral" compliance condition is supported, as well, by the fact it is the same stiffness value characterizing healthy valve inlets. Such condition have given me the possibility to focus my analysis only on changes in cell behavior determined by substrate morphology and not surface rigidity. AN important point I want to stress about is the fact that many studies you can find in literature where CNTs-cell interaction is studied, have shown that CNTs in solution can be toxic to cells [190,191]. From the other hand, CNTs strongly attached or embedded to a support surface do not show to have any cytotoxic effects. Being directly grown, and consequently attached, on a supporting glass surface, our CNTs demonstrated to have any kind of toxic effect on cells, in particular on pVICs (Fig. 30). One of the effects determined by ECM morphology in the onset of CAVD is the pro-pathological phenotypic modification that could be induced. In particular we have to consider that VICs composition in a healthy valve is about 5% represented by myofibroblasts while a no-longer healthy valve have more than 30% of VICs population formed by myofibroblasts [112]. My results have shown that a totally different morphological and phenotypic effect is induced on pVICs by the two substrates I tested: nanostructured tCNTs carpets and flat glass controls (Fig. 32-33-34). Surprisingly, I have found that the percentage of myofibroblasts characterizing cell cultures developed above CNTs was very similar to that in a healthy valve [112]. This suggests that the morphology of CNTs seems able to prevent the pro-pathologic phenotypic modification of VICs. Has to be considered anyhow that inside a real tissue leaflet a strong mechanical heterogeneity is present [118,227] and it has already been shown that tissutal VICs elastic moduli are strongly influenced by the mechanical properties of surrounding ECM [8,80,125]. Therefore, I evaluated the stiffness of the cells grown on the two substrates (glass and CNTs) and what I found is that the fibroblasts present on CNTs are significantly stiffer than those grown on glass substrate while, and this is the more intriguing point, the myofibroblasts grown on CNTs are softer than those grown on glass (any difference is instead visible between smooth muscle cells grown on both substrates) (Fig. 35). It is well known

that mechanical stimuli are transmitted from ECM to actin cytoskeleton through the Focal Adhesion points [20] and their number, shape and distribution is directly correlated to the intracellular tensional state [195,196]. In this context, I evaluated the FAs of pVICs grown on both substrates by vinculin staining (Fig. 36 a-b). The same trend I observed in cell stiffness (Fig. 35) is confirmed as well by the number of FAs (Fig. 36c). Surprisingly, myofibroblasts FAs density when grown on CNTs is significantly lower than FAs density determined for fibroblast in the same condition (Fig. 36d). This result confirms the stiffness data measured with the AFM that pointed out a stiffer value for fibroblast grown on CNTs than for myofibroblast developed on CNTs (Fig. 32 a-b). My results have led us to hypothesize a strong interaction between the CNTs and pVICs. In 2009 Ballerini L. it has already been hypothesized that a pinching phenomenon happens during the interaction between neuronal cells plasma membrane and CNTs increasing, in this way, network electrophysiological activity [172]. Coherently to this observation, I observed as well that CNTs below the plasma membrane are able to completely cross it (Fig. 38). In this context, I can speculate that this phenomena, could not only stabilize the bilayer [198], but promote the formation and clustering of FAs in pVICs grown on CNTs (Fig. 36) contributing, in this way, to increase the cells stiffness (Fig. 35).

Concluding, I can confirm that in the onset of CAVD both the rigidity and the morphology of the substrate (or matrix) greatly affect the VICs behavior. In particular, I identified a stiffness range between the cells are in a state of quiescence and a nano-structured material that have a positive effect on VICs phenotype fate/evolution. This opens a new perspective to understand the relationships between valve-resident cells in both physiologic *vs*. pathologic contexts [228] and, moreover, a specification criteria to designing scaffolds with mechanically and morphologically controlled characteristics able to assure human-derived VICs development and colonization with a quiescent phenotype [8,229] for valve tissue engineering applications [230].

Tumor associated p53 missense mutants

It is well known that many biophysical processes are involved in the onset and progression of cancer disease. In particular, there is an increasing interest in the study of TP53 missense mutants because it is the most frequent genetic mark in human cancers. These mutants have demonstrated to have a strong impact on cancer progression, metastatic potential and drug resistance [140].

This last effect is a prerequisite for mutant p53 protein stabilization [231]. Aiming to study cellular processes and biochemical pathways responsible for mutant p53 stabilization in the cancer, a drug screening on MDA-MB 231 cell line was performed and one class of drugs which associated with mutant p53 level decrease called Statin was identified. Statins are well known drugs, commonly used in clinical and medical applications to lower cholesterol plasma levels in patients with cardiovascular disease by limiting the function mevalonate pathway [200]. The statin have been found to inhibit the enzymatic activity of RhoA [148] which is a target of mutant p53 in controlling cellular metabolism [148,203]. However, RhoA is also a regulator of actin cytoskeleton rearrangement and its activity is fundamental for the transmission of mechanical stimuli from ECM to cells [204]. These observations have allowed us to hypothesize that mechanical cell variations may have an effect on p53 levels through mevalonate/RhoA signaling. Therefore, I have tested the cellular stiffness of cells treated with different drugs confirming a stiffness reduction when drug molecules determine actin cytoskeleton de-structuration (Fig. 39a). At the same time, the results coming out form cells treated with Latrunculin A proved that a reduction of stress fibers happens in conjunction with a reduction of mutant p53 levels (Fig. 39b). This demonstrates that RhoA-dependent acto-myosin dynamic impacts mutant p53 levels in tumoral cells. Based on the results obtained *in vitro,* I took advantage of my AFM nanoindentation procedure to evaluate the role of mevalonate pathway in tumor mechano-signaling and potential effects on mutant p53 level in an *ex vivo* model. From my results it was evident that the rigidity of both cancer cells and ECM was reduced after a Zoledronic acid treatment (Fig. 40a) and a subsequent molecular analysis demonstrated a reduction of the phosphorylation of focal adhesion points, of myosin light chain 2 and of mutant p53 levels (Fig. 40b). Therefore, it seems that, *in vivo* as *in vitro,* the mevalonate pathway is strongly involved in tumor mechanosensing and regulate mutant p53 levels.

In this framework, I have proved that the ECM rigidity, by controlling RhoA activation and actin polymerization, indirectly regulates the mutant p53 level and its activation. In addition, these mechanical variations in ECM could induce stabilization of mutant p53 and activation of drug resistance.

Myogenesis

In the last decades, many strategies have been exploited to develop new materials for skeletal muscle regeneration applications [151]. Key features these materials have to have are improved cell adhesion, proliferation, differentiation and ability to induce contractile activity in resulting myotubes. In this context, I have characterized a new polypeptide of the HELP family [167], called HELPc, that has been employed as a growing substrate for C2C12 myoblasts together with HELP and HELP1 controls. As has been already observed in several synthetic scaffolds for tissue engineering, the presence of the RGD sequence increases cell adhesion [232]. In fact, the peculiarity of HELPc was the addition at its C-terminal of a sequence from the α2 isoform of collagen type IV, containing two RGD motives (Fig. 41). RGD motives are a physiological ligand of membrane integrins regulating the cytoskeleton rearrangement, cell shape and locomotion. My morphological characterization, via AFM imaging, revealed an amorphous topology for both the protein assembles (Fig. 42a). Consequently is not surprising that, in C2C12 grown on HELPc, a greater adhesion was observed than on other substrates and, as well, a larger number of lamellopodia , a common indicator of a higher degree of cell motility [233] that could result in an increased cellular alignment and fusion capacity. It is now clear that many cellular processes are regulated by the forces that are generated by the ECM-cell interaction [234]. Therefore, I have measured the cellular stiffness, *via* AFM force spectroscopy and, as expected, C2C12 myotubes on HELPc are stiffer than HELP and HELP1 (Fig. 44). It is believed that cellular rigidity is related to cellular contraction [234,235], in our case, myotubes grown on HELPc have a higher contraction activity than those grown on the other two polypeptides (Fig. 45). Following, we considered that also the mechanical properties of the ECM could be involved in skeletal muscle cell development. Therefore, I have characterized hydrogels of different stiffness made with the same polypeptides, fabricated exploiting the presence of residues GLn and Lys in the HELP hydrophilic sequence in order to obtain a HELPc hydrogels at two different percentage of monomer (5% and 7% w/v). My AFM surface characterization has revealed similar morphologies for the two samples (Fig. 46) but significantly different from bi-dimensional layer made by HELPc glass slide coating (Fig. 42a). These differences in morphology could be attributed to the different mechanism of synthesis taking place in HELPc hydrogel. As was

previously done for HELPc coating, C2C12 myotubes were pleated on the HELPc hydrogel and cell adhesion was evaluated as well proliferation and differentiation. Surprisingly, several striking differences has been found between the different HELP compositions tested, in particular hydrogels show a high proliferation and partially inhibit myogenic differentiation than bi-dimensional counterparts.

My results allowed us to understand that HELP family of polypeptides could be a precious bio-engineering tool to study the functional consequence of cell-biomaterial interactions. In particular, the addition of C-terminal a sequence from the α2 isoform of collagen type IV to HELPc structure increases its applicability as a new biomaterial for muscle regeneration.

Final remarks

During the last decades, the general interest on cell and tissue biophysical properties has significantly increased. These properties, in fact, determine cell behavior modifications and, more interestingly, have the potential to be used to discriminate between the physiological or the pathological condition of a tissue. For this reason, clinical research community is particularly interested and focused in identifying new (nano)technological tools that can diagnose the onset, progression and aggression of a disease in its very early stage.

Herein, I have exploited the great versatility of the AFM to highlight the importance of mechanobiology and mechanotransduction in the framework of three different cellular systems. Thanks to the combination of AFM nano-indentation analysis to conventional biomolecular techniques, I could confirm that the variations in ECM mechanical properties determine changes in cellular stiffness in calcific aortic valve tissues. In addition, I could hypothesize that in the human healthy valve exist three range of stiffness, presumably associated to the natural extracellular matrix, which guide the onset of the disease. These results were also validated on an *ex vivo* system, via AFM force mapping of transversal thin sections of explanted stenotic calcific human valves, obtained from patients that underwent aortic valve replacement. Furthermore, I interfaced porcine Valve Interstitial Cells with transparent carbon nanotubes substrates in order to investigated any possible berturbation in cellular properties induced by a nanomaterial that mimics an ECM morphology. Even in this case the AFM revealed to be an extremely powerful technique allowing the mechanical characterization of cells grown above such nanostructured substrates as, as well, the characterization of the tCNTs carpet itself pointing out for it a “neutral” value of stiffness. In this way I was able to decouple the substrate morphological contribution to the cell behavior from its compliance contribution. That thanks to the fact its stiffness value is very close to the one characterizing healthy valve inlets. Moreover, I observed that CNTs induce a positive effect on pVICs differentiation respect to a flat and rigid glass control. In fact, from our results, I could say that the amount of myofibroblasts on glass and tCNTs substrate are comparable to those reported in literature for pathological and healthy valves, respectively. In a second cellular system I studied, I demonstrated, *via* AFM, that in tumor associated p53 missense mutants, the ECM rigidity indirectly regulates level and activation of mutant p53 and could determine the drug resistance in both *in vivo* and *in vitro* conditions. Finally, in the last cellular

system I had the possibility to study, AFM was initially used to perform a morphological characterization of a new polymer, HELPc, in order to evaluated its possible application in the field of skeletal muscle regeneration. Furthermore, nanoindentation experiments were performed to characterize the rigidity of C2C12 myotubes grown on such HELPc 2D and 3D scaffolds and I discover that substrate stiffness is closely related to cell adhesion and contractile activity of myotubes: an essential feature for muscle tissue regeneration.

My results show that atomic force microscopy is an excellent tool to study the mechanical properties, and not only, of different cellular system. For this reason, the development of a simplified version of this tool could be a great candidate tool for medical and clinical diagnostics.

Materials and methods

10. Valve interstitial cells grown on different substrates

Tunable stiffness substrates preparation and functionalization

Substrates of known stiffness were produced according to the protocol described by Pelham R.J. and Wang J. [1,236]. Briefly, 33 μL of polyacrylamide (PAA) solution are deposited onto a glass slides. The PAA solution contains 0.15% tetramethylethylenediamine, 0.075% ammonium persulfate and acrylamide and bisacrylamide in varius ratios (Low= 3.0% acrylamide, 0.06% bisacrylamide, Medium Low= 7.5% acrylamide, 0.03% bislacrylamide; Medium High= 7.5% acrylamide, 0.05% bisacrylamide; High= 7.5% acrylamide, 0.12% bisacrylamide), thus allowing the polymerization of gels with tuned stiffness. A glass coverslip (18 mm x 18 mm), previously treated by Surfacil (Pierce) to prevent adhesion to the gel, is placed on the top of the un-polymerized gel solution and kept under nitrogen flow, until a thin attachment and proliferation onto the gel, the acrylamide surface is activated by treatment with sulfosuccinimidyl 6(49-azido-29-nitrophenyl-amino) hexanoate (Sulfo-SANPAH; Pierce) 0.2 mg/mL in Hepes 50 mM (pH 8.5), exposed to UV light (365 nm, 20 minutes), and coated by overnight incubation at 4 °C with 0.2 mg/mL type I collagen from rat tail (Worthington) in Hepes 50 mM. Substrate sterilization was performed by UV (250 nm) light exposure (30 minutes). AFM measurements served to find an accurate correlation between gel composition and stiffness, as described in the dedicated paragraph.

CNTs synthesis

Multi-walled carbon nanotubes were synthesized by the catalytic decomposition of acetylene (carbon source) over an iron catalyst thin layer using fused silica (SiO_2) wafer chips as supporting substrates [237]. The wafers were manually cleaved into 15x15 mm^2 samples using a diamond scribe and cleaned by Radio Corporation of America (RCA) method [238]. This was followed by the deposition of a thin iron layer (0.2–1 nm in thickness) directly on the SiO_2 chips using electron beam (e-beam) evaporation. Iron film thickness was monitored with an *in-situ* quartz crystal microbalance. Since the uniformity of the catalyst layer is crucial for CNTs growth, an

average deposition rate of 0.2 Å/sec was adopted. Subsequently, the as-evaporated substrates were located on the heating element inside the high vacuum reaction chamber. An annealing treatment (4 min at 650–670 °C in H_2 atmosphere) was performed to reduce iron oxides possibly present on film surface, as a result of the exposition to atmospheric air conditions during transfer from the metal deposition system to the CCVD reactor, and to break down the continuous iron layer into nanoparticles which subsequently act as nucleation sites for CNTs growth. Once the pre-treatment process was over, the carbon source was immediately introduced in the reaction chamber up to a partial pressure of 10–20 mbar. Sample temperature was increased to 730 °C and reaction time was limited to 90 seconds, resulting in the formation of a uniform carpet of vertically aligned CNTs of less than 10 μm in length. After that, samples were cooled down to room temperature and employed as removed from the reaction chamber.

CNTs images perform by Field Emission Scanning Electron Microscopy

Field Emission Scanning Electron Microscopy (FE-SEM) imaging was performed on the as-produced CNTs using a Gemini SUPRA 40 SEM (Carl Zeiss NTS GmbH, Oberkochen, Germany) operating at an accelerating voltage of 5 keV.

Transmission electron microscopy of CNTs

Transmission electron microscopy (TEM) of CNT carpets was performed using an EM 208-Philips TEM system equipped with Quemesa (Olympus Soft Imaging Solutions) camera. Before TEM imaging, samples were released from the substrates, dispersed in ethanol and a drop of the solution was deposited onto a commercial lacey-carbon grid.

Raman spectroscopy of CNTs

Raman spectroscopy was conducted on the as-produced CNTs at room temperature employing a Renishaw inVia Raman microscope with a 60x objective lens at 632.8 nm laser excitation and a laser power of 2 mW.

X-ray Photoelectron Spectroscopy of CNTs

In order to evaluate the CNTs surface composition, X-ray Photoelectron Spectroscopy (XPS) was carried out using a commercial Xray photoelectron spectrometer (VG-ESCALAB-II) equipped with a monochromatic Al Kα X-ray source (1486.6 eV) and a hemispherical energy analyzer with

a base pressure below 1×10-10 mbar. Core-level XPS data analysis was performed after the removal of nonlinear Shirley background and deconvolution into Gaussian/Lorentzian components using Casa-XPS software**.**

Cell isolation and cell culture

Primary human VICs were isolated by enzymatic dissociation of non-calcific portion of pathologic aortic valve leaflet, derived as discard material from surgical valve replacement. Whereas pig VICs were obtained using aortic valves of pigs of 6–9 months of age. Both cell lines were isolated using a protocol described previously by Santoro R. et al. [239] Briefly, a first incubation for 5 min on shaker at 37 °C in Collagenase Type II (Worthington) solution (1000 U mL^{-1}), to remove the endothelial layer was performed. In order to isolate the pVICs, a second 2h incubation under the same conditions was carry out. Following cells were seeded for *ex vivo* amplification on 1% gelatin coated plastic cell culture dishes (10 cm diameter). The cells were grown in DMEM (Thermofisher Scientific, OR, USA) containing 150 U mL^{-1} penicillin/streptomycin (Sigma–Aldrich) and 2 mM L-glutamine (Sigma–Aldrich), and 10% Fetal bovine serum (Sigma-Aldrich, St. Louis, MO, USA).

hVICs culture onto PAA gels

hVICs were seeded onto substrates of controlled rigidity (PAA gels or glass coverslip), at a density of $2.0x10^3$ cells, and cultured for 48 hours before fixation in paraformaldehyde (PFA 4%) for either immunofluorescence staining or AFM spectroscopy.

pVICs culture above CNTs carpets

pVICs were seeded onto substrates (CNTs or glass coverslip) at a density $1.0x10^5$ cells, and cultured for 72 hours before fixation in paraformaldehyde (PFA 4%) for either immunofluorescence staining or AFM spectroscopy. Whereas pVICs were seeded onto both substrates at a density $5.0x10^5$ cells for squirting essay. Before seeding all the samples are washed with ethanol and plasma cleaned

Pharmacological inhibition of cytoskeleton polymerization of hVICs

hVICs were seeded at low density (see paragraph hVICs culture onto PAA gels) onto either PAA gels and glass coverslip supplementing, after 24 hours, the culture medium with 10 μM Rho-Kinase activated ROCK phosphorylation inhibitor (Y27632, Sigma Aldrich), for 2 hrs. Recovery of cell morphology and cytoskeleton rearrangement from inhibition treatment was evaluated 24 hours after substitution with fresh medium, while the recovery of cell stiffness was estimated after 24 and 48 hours after change with fresh medium. Effect of inhibition on cell morphology, cytoskeleton organization and stiffness was performed after fixation after cell fixation (PFA 4%). Effect of pharmacological treatment on gene expression was evaluated by total RNA extraction from cells culture onto glass slides.

Gene expression of hVICs

Total RNA was extracted from cells using Tripure reagent (Roche Diagnostics), using a in column method (Zymo Research), including a DNAse treatment, and retrotranscribed into cDNA with Superscript II (Thermo Fisher Scientific). Quantitative real-time PCR (qRT-PCR) amplification were performed for GAPDH, ANKRD1, CTGF, CYR61, ACTA2 (Primers details in Table 1), using Power Syber Green PCR Master Mix (Applied Biosystem) on a 7900 Fast Real-Time PCR System (Applied Biosystem). Gene expression levels were normalized to GAPDH expression data. The $2^{-\Delta\Delta Ct}$ method was employed to calculate the fold change of the genes in Y27632 treated *vs.* control samples.

Gene	Direction	Sequence (5'→3')
hACTA2	Forward	AGA GTT ACG AGT TGC CTG ATG
hACTA2	Reverse	CTG TTG TAG GTG GTT TCA TGG A
hANKRD1	Forward	AGT GAG GAA CTG GTC ACT GG
hANKRD1	Reverse	TGG GCT AGA AGT GCT TTC AGA T
hCTGF	Forward	AGG AGT GGG TGT GTG ACG A
hCTGF	Reverse	CCA GGC AGT TGG CTC TAA TC
hCYR61	Forward	CCT TGT GGA CGAGTG TA
hCYR61	Reverse	ACT TGG TCC GGT ATT TCT TC
hGAPDH	Forward	AAT CCC ATC ACC ATC TTC CAG
hGAPDH	Reverse	AAA TGA GCC CCA GCC TCC

Table 1: *List the primers employed in qRT-PCR experiments*

Antibodies and fluorophores

Anti-vinculin antibody (mouse monoclonal, VIIF9 (7F9); Sigma-Aldrich, St. Louis, MO, USA) was employed at 1:20 dilution. Alexa Fluor 594 phalloidin (Thermofisher Scientific, OR, USA) was employed at 1:10 dilution. 1,1'-Dioctadecyl-3,3,3',3'-Tetramethylindocarbocyanine Perchlorate (DIL, ThermoFisher Scientific, OR, USA) was employed at 1:100 dilution. Anti-α-SMA antibody (Monoclonal Mouse Anti-Human, Clone 1A4, Agilent Technologies, Santa Clara, USA) was employed at 1:50 dilution. Anti-YAP antibody (Santa Cruz) was employed at 1:200 dilution. Anti-Vimentin antibody (Cell Signaling) was employed at 1:200 dilution. Goat anti-Mouse IgG Secondary Antibody, Alexa Fluor 594 (Thermofisher Scientific, OR, USA) was employed at 1:500 dilution. Goat anti-Mouse IgG Secondary Antibody, Alexa Fluor 488 (Thermofisher Scientific, OR, USA) was employed at 1:500 dilution.

Western analysis

Cellular proteins were collected from cells before and after Y27632 and recovery using RIPA buffer (10 mM Tris-Cl, pH 7.4, 150 mM NaCl, 5 mM EDTA, 1% v/v triton X-100, 1 % w/v sodium deoxycholate, 0.1% w/v sodium dodecyl sulfate and 1% v/v protease and phosphatase

inhibitor). Following protein concentration determination (Pierce™ BCA Protein Assay Kit, Thermo scientific), 30 μg of total protein solution were diluted into Laemli buffer. After heating at 95 °C proteins were run into SDS-PAGE. Proteins were transferred to a nitrocellulose membrane by wet transfer protocol (25 mM Tris, 190 mM Glycine, 20% Methanol, SDS 0.02%) for 2h at 100V. Before western analysis, non-specific binding was blocked by incubating filters with 5% non-fat dried milk in PBS. Overnight incubation at 4 °C with primary antibodies listed in paragraph 10.1.12 was followed by incubation for 20 minutes at room temperature with secondary antibodies. Protein bands were acquired by Odissie (LI-COR), and quantified using ImageJ. Data quantification was performed by normalizing protein bands intensity to the intensity of GAPDH internal control.

Immunofluorescence assay on pVICs grown on CNTs

Coverslips and CNTs were washed 3 times with PBS and then fixed with 4% paraformaldehyde (PFA) for 30 minutes at RT. After fixation, samples were permeabilized with a solution containing 0.5% Tween in PBS for 10 minutes and were washed 3 times with a solution containing 0.1% Tween in PBS. After permeabilization, samples were blocked with a solution containing 5% fetal bovine serum (FBS) in PBS for 1 hour. Samples were incubated for 30 hours at RT with aN Alexa Fluor 594 phalloidin at the appropriate dilution in a blocking solution (5% FBS in PBS). After 3 washes of 5 minutes with PBS, coverslips were incubated with the Anti-vinculin antibody for 2 hours at RT at the appropriate dilution in a blocking solution (5% FBS in PBS). Samples, washed 3 times for 5 minutes with PBS, were incubated with secondary antibody for 2 hours at RT at the appropriate dilution in a blocking solution (5% FBS in PBS). After 3 washes of 5 minutes with PBS, the nuclei are stained by incubation with DAPI (Sigma Aldrich) in PBS (1:3000) for 5 minutes. The samples were washed two times in PBS and once in H_2O mQ. The Samples were then mounted onto slides and visualized under a Inverted Research Microscope Eclipse TiU, Nikon (Nikon Corporation). The analysis of image was conducted using the program ImageJ.

Immunofluorescence assay on hVICs grown on PAA gels

The protocol for immunofluorescence experiments is the same as described above. Images acquired by fluorescence microscopy (Apotome; Carl Zeiss, Jena, Germany) were also used to perform automated cell counting and morphological evaluations (ImageJ).

Cell density and branching assay

Cells were plated on both substrates at a confluence of $1.0x10^5$ cells. After 12-72 hours, the cells were fixed and labeled with phalloidin and DAPI according to the immunofluorescence protocol. For each sample 25 fields were acquired. Cell density was generated calculating the ratio between the number of nuclei and area of the image:

$$\text{Number of nuclei/area of image } [mm^2]$$

Cell branching was generated calculating the ratio between the number of processes and number of cells:

$$\text{Processes number/cells number}$$

The analysis of image was conducted using the program ImageJ.

Identification pVICs phenotypes grown on CNTs substrates

Cells were plated on both substrates at a confluence of $1.0x10^5$ cells. After 12-72 hours, the cells were fixed and labeled with phalloidin and DAPI according to the immunofluorescence protocol. For each sample 25 fields were acquired and cells for phenotypes were evaluated. In order to identify the cell phenotype was calculating the ratio between long side and short side identifying three phenotypes smoot muscle cells [from 1 to 1.5], myofibroblasts [from 1.5 to 3.0] and fibroblasts [larger than 3.0]. The analysis of image was conducted using the program ImageJ.

pVICs Squirting assay

Cells were plated on both substrates at a confluence of $5.0x10^5$ cells. Before seeding all the samples are washed with ethanol and plasma cleaned. After 72 hours, the cells were subjected to

osmotic shock to obtain the basal cell membrane using a protocol described previously by Ziegler U. et al. [197]. Briefly, cells were washed with ice cold 20 mM PIPES, 150 mM KCl, pH 6.2, incubated in hypotonic buffer (4 mM PIPES, 30 mM KCl, pH 6.2) for 3 min on ice and subsequently squirted using 5 mL of the same buffer through a 25- gauge needle. Incubation in high salt was done in 2 M NaCl, 2.7 mM KCl, 1.5 mM KH2PO4, 1 mM Na2HPO4, pH 7.2 for 30 min at room temperature. After the samples were fixed in 4% PFA and were washed 3 times in PBS.

SEM image on pVIC basal membrane

Before Field Emission Scanning Electron Microscopy (FE-SEM), a lightweight gold evaporation at control (Glass) was performed, while no pretreatment was carried out to CNTs because they were already conductive. FE-SEM imaging was performed on the as-produced CNTs using a Gemini SUPRA 40 SEM (Carl Zeiss NTS GmbH, Oberkochen, Germany) operating at an accelerating voltage of 3 keV.

Atomic Force Microscopy characterization

The basal cell membranes were stained with DIL at the appropriate dilution in H_2O mQ (1:100) for 15 minutes and the nuclei were stained by incubation with DAPI (Sigma Aldrich) in H_2O mQ (1:3000) for 5 minutes. After 3 washes in H_2O mQ, the samples were dried. AFM was used to characterize in thickness and morphology of basal cell membrane. The AFM image was acquire using a commercially available microscopy, NT-MDT Smena (NT-MDT, Russia) mounted on Inverted Research Microscope Eclipse TiU, Nikon (Nikon Corporation). All AFM measurements were carried out at room temperature working in dynamic mode in air. The samples were imaged using cantilevers characterized by a resonance frequency of about 65 kHz and a force constant of about 0.6 nN/nm (HQ:NSC36/C from MikroMasch Co. - Tallinn – Estonia). 512×512 pixels images were acquired at 0.3 lines/second scan speed. Gwyddion software (www.gwyddion.net) was used to analyze AFM images.

Atomic force Microscopy force spectroscopy on pVICs grown on CNTs

For AFM force spectroscopy, cells were seeded on both substrates at a confluence of $1.0x10^5$ cells. Before seeding all the samples are washed with ethanol and plasma cleaned. After 72 hours,

samples were fixed in 4% PFA and were washed 3 times in PBS. Before the AFM force spectroscopy measurement, the nuclei were stained by incubation with DAPI (Sigma Aldrich) in PBS (1:3000) for 5 minutes and the samples were washed 3 times in PBS. All AFM measurements were carried out at room temperature working in contact mode in PBS 1X. AFM elastic assessment of stiffness was done taking advantage of the distinctive force spectroscopy capabilities of the NT-MDT Smena. In brief, force spectroscopy measures the deflection of an AFM cantilever while it is pushed to a surface. These data were subsequently converted in a force/indentation curve via cantilever spring constant and displacement knowledge [240]. Compliance of the material under the tip may be determined fitting the data with a Hertzian model of surface indentation [241]. Indentation measures were performed positioning the tip on the cell nucleus. A cantilever with a sphere of 20 μm in diameter, manually glued, with an elastic constant of about 0.03 N/m and a resonance frequency of about 10 kHz (CSG11B- from NT-MDT) was used. Force spectroscopy measurements were performed at constant speed (2.5 μm/s) and triggered to a maximum sample indentation of 500 nm. For each sample, 1 cell curve was acquired on a total of 60 cells. Elastic modulus values, expressed in kPa, were determined by interpolating with the Hertzian model. The analysis was done using the Nova-Px 3.4 Smena software.

Atomic force Microscopy force spectroscopy on hVICs grown on PAA gels.

The rigidity of elastomeric substrates and cells was quantified through AFM force spectroscopy (Smena, NT-MDT, RU). Briefly force spectroscopy measures the deflection of an AFM cantilever while it is pushed to a surface. These data were subsequently converted in a force/indentation curve via cantilever spring constant and displacement knowledge [240]. Compliance of the material under the tip may be determined fitting the data with a Hertzian model of surface indentation [242]. Indentation measures were performed positioning the tip on the cell nucleus. A cantilever with a sphere of 20 μm in diameter, manually glued, with an elastic constant of about 0.03 N/m and a resonance frequency of about 10 kHz (CSG11B- from NT-MDT) was used. Force spectroscopy measurements were performed indentation speeds between 2.5 μm/s and 10 μm/s and with a maximum value of indentation set at 500 nm in order to measure the mechanical characteristics of the cytoskeletal component by reducing the contribution of the nucleus and of the underlying surface. For each sample, 1 cell curve was

acquired on a total of 30 cells (5 measurements each cell) while the stiffness of the substrate was determined as an average of 15 curves at different positions of the sample. Elastic modulus values, expressed in kPa, were determined by interpolating with the Hertzian model. The analysis was done using the Nova-Px 3.4 Smena software.

Ex vivo VAO histological preparation

AOV leaflets were fixed in 4% PFA overnight at 4 °C. Samples were washed in PBS and incubated first for nine hours in 15% sucrose-PBS solution, then overnight in 30% sucrose-PBS solution, before inclusion in OCT compound at –20 °C. Cryosectioning was performed at –20 °C with a HM525NX cryostat (Thermo Scientific). Transversal sections (10 µm thickness) were collected onto glass slides (SuperFrost Plus, Thermo Scientific) and air-dried (20 min, 37 °C in ventilated oven) before performing either staining or local rigidity mapping. The protocol for immunofluorescence experiments is the same as described above and the reagents listed in Table 1. Images were acquired using fluorescence (Apotome or LSM710; Carl Zeiss, Jena, Germany).

Ex vivo Aortic Valve leaflet AFM force spectroscopy map

The *Ex vivo* VAO histological preparation is the same as described above. Before the AFM force spectroscopy map measures, the leaflet slice was left at room temperature for 10 minutes. After the sample was washed gently 3 times with PBS 1X and air-dried (20 min, 37 ° C in ventilated oven). Following, the optical image with Inverted Research Microscope Eclipse Ti, Nikon (Nikon Corporation) was acquired and it was divided into squares 100 µm x 100 µm though ImageJ. In general AFM force spectroscopy map was performed with the same protocol described in the paragraph "Atomic force Microscopy force spectroscopy on pVICs grown on CNTs". A cantilever with a sphere of 20 µm in diameter, manually glued, with an elastic constant of about 5.5 N/m and a resonance frequency of about 150 kHz (NSG11- from NT-MDT) was used. For leaflet slice mapping, 1 curve was acquired in the center of each squares for 3 different donors. Elastic modulus values, expressed in kPa, were determined by interpolating with the Hertzian model. The analysis was done using the Nova-Px 3.4 Smena software. After the force mapping image was compared with histological image after Von Kossa and eosin staining in order to identify the calcific and non-calcific portions of AOV.

Statistical analysis

The statistical analysis and data processing were performed with R program. The Shapiro Wilk test was applied to the data to understand if they had a normal distribution or not. When the data distribution was normal, then parametric, the T-test or test-student was applied. While when the distribution is not normal, then it is not parametric, U-test or Wilcoxon-Mann-Whitney test was applied. In some cases, 1-way ANOVA was applied.

11 Tumor associated p53 missense mutants

Cell lines

MDA-MB-231 cells were cultured in DMEM (LONZA) supplemented with 10% Fetal Bovine Serum (FBS) and with 1% penicillin 100 U/mL and streptomycin 10 μg/mL.

Reagents

The following compounds were purchased from Sigma Aldrich: Cerivastatin (SML0005), Geranylgeranyl Pyrophosphate (#G6025), Zoledronic Acid (SML0223), Blebbistatin (B0560), Y-27632 dihydrochloride (Y0503). Latrunculin-A (sc-202691) was purchased from Santa Cruz Biotechnology. Picro Sirus Red Stain Kit (Connective Stain) (ab 150681) was purchased from Abcam.

Antibodies

Antibodies used for western blot and immunofluorescence were: anti-p53 (1:1000; DO-1; Santa Cruz Biotechnology), anti-Actin (1:5000; C11; Sigma), Anti-Vinculin (1:5000; V4505; Sigma), anti-MLC2 (1:1000; 3672; Cell Signaling), anti-pMLC2 (phospho Ser19) (1:1000; 3672S; Cell Signaling), anti-FAK (C-20) (1:1000; sc-15407; Santa Cruz Biotechnology), anti-pFAK (phospho Y397) (1:1000; ab81298; abcam).

Immunofluorescence and Western Blot essays

Immunofluorescence staining was carried out as previously described [202]. Briefly, cells were fixed in 4% paraformaldehyde for 10 minutes, washed in PBS, permebilized with Triton 0.1% for 10 minutes and blocked in PBS FBS 3 % for 30 minutes. The primary antibody was incubated for 1 hour at 37 °C and the secondary antibody, Goat anti-mouse Alexa Fluor 568 (Life Technologies) was incubated for 30 minutes at 37 °C. Nuclei were stained with Hoechst 33342 (Life Technologies). Western Blot analysis was carried out as previously described [202]. The protein stability measurement as previously described [243]. Immunoblots were quantified with ImageJ program. The integrated density of bands was corrected for background. Two-tail Student's t-Test was performed to determine statistical significance.

Mice and animal care

For *in vivo* studies, one million of MDA-MB-231 cells were resuspended in100 μL of DMEM, injected into the mammary fat of previously anesthetized 7 weeks old SCID female mice (1-3% isoflurane, Merial Italia S.p.A, Italy) as previously described [202]. At day 12 after cell injection, mice were subjected to intravenous injection of zoledronic acid ([1-hydroxy-2-(1H-imidazoledronic acid-1-y1) ethylidene]) (200 μg/Kg body weight), every 4 days until the end of the experiment (day 40). The mice were used and housed in a specific pathogen-free (SPF) animal facility. Procedures involving animals and their care were and their care were performed in conformity with institutional guidelines (D.L. 116/92 and subsequent complementing circulars) and all experimental protocols were approved by the ethical Committee of the University of Padua (CEASA). At day 40 the animals were sacrificed and the primary tumors were extracted and directly frozen in liquid nitrogen. Tissues were lysed for immunoblot analysis or sectioned at 5 μm, fixed, and stained either with hematoxylin and eosin (H&E) for histological analysis or with Picro Sirius and hematoxylin to performed AFM analysis. For tumors per group were used.

Atomic Force Microscopy analysis

Atomic force microscopy was used to investigate cell mechanical properties. In particular, elastic assessment of stiffness was done taking advantage of force spectroscopy capabilities of a Smena AFM (NT-MDT Co., Moscow, Russia) mounted on an inverted fluorescence microscope (Nikon Eclipse Ti-U). AFM force spectroscopy on single cells was performed as described previously for pVIC grown on CNTs.

Tissue section's stiffness was studied evaluating the stiffness of the cells inside the tissue, marking their nuclei via Hematoxylin staining, and ECM stiffness, pointing it out by the collagen and amyloid specific dye Picro Sirius Red Stain. AFM force curves were obtained on each sample (4 control, not treated, samples and 4 zoledronate treated ones) randomly acquiring about 60 curves on blue, Hematoxylin positive, areas and about 60 curves on red, Picro Sirius Red positive, areas (see Fig. 39a). A total number of 210 and 245 stiffness values were obtained for controls and treated cells, respectively. 240 and 239 curves were instead acquired for controls and treated ECMs. During AFM characterization sections were maintained immersed in 1X PBS

buffer at room temperature. Cantilever used was a tip-less probe characterized by a spring constant of about 0.03 nN/nm (HQ:CSC38 cantilevers from MikroMAsch Co.- Tallin, Estonia) at the end of which a 18 μm in diameter silica bead (Thermo Fisher Scientific, CA, USA) was glued using UV curable glue (Norland Products Inc., NJ, USA). Force spectroscopy measurements were performed at constant speed (2.5 μm/s) and triggered to a maximum force applied to the sample of 5 nN. Elastic modulus values (E), in kPa, were determined by fitting obtained force-displacement curves with an Hertzian model for the tip used taking advantage of the NOVA (NT-MDT Co., Moscow, Russia) control and analysis software.

Statistics and data processing were performed using Igor Pro software (www.wavematrics.com) and R statistical computing software (www.R-Project.org). Significance of data differences was established as equality of probability distributions via Kolmogorov-Smirnov test.

12 Myogenesis induced by Human Elastin-Like Polypeptides

HELPc synthesis

HELP and HELP1 was synthesized as previously described [244,245]. HELPc was synthesized starting from the function the synthetic gene of HELP polypeptides with the 41aa coding sequence corresponding to the 854-895 region of the collagen IV α2 chain (NP_001837.2). The final construct was evaluated by sequencing and the product in the C3037 *Escherichia coli* strain was expressed (New England Biolabs, Ipswich, MA). Expression and purification were performed as described previously [245]. The polypeptides obtained were analyzed by SDS-PAGE and the purified products were lyophilized for long term storage.

HELP polypeptides coating

The lyophilized polypeptides were resuspunded in water and sterilized by filtration (0.22 μm). Protein concentration was evaluated by the Bradford method. HELPs coating were carried out by depositing 0.1 mg/mL of aqueous protein solution onto glass coverslips. Coating solution was dried in a tissue culture hood and cells were seeded on the polypeptides surface. Coated coverslips were incubated with Dulbecco's modified Eagle's medium (DMEM) added with 20% fetal calf serum, at 37 °C in CO_2 incubator for 48 hours.

HELPc synthesis and preparation of HELPc hydrogels

HELPc synthesis was performed as described in the previously paragraph. The enzymatic cross-linking was carried out in a tissue culture hood under sterile conditions. In order to obtain HELPc hydrogels, polypeptides were cross-linked with bacterial TGase. The recombinant protein was dissolved in 10 mM Tris/HCl, pH 8, in order to obtain a concentration of 5% and 7% w/v. Solutions (100 μL each) were stored in an ice bath for 30 minutes to promote solubilization. Afterward, 0.53 U of TGase (133 U/mL) was added, and the reaction mixture was quickly mixed. Then 15 μL of each polypeptide solution was dropped on round glass coverslips (13 mm) and incubated at 10 °C for 2 hours. Cross-linking reaction was finished after overnight incubation at 4 °C. Hydrogels were washed with 70% ethanol and then rinsed thoroughly with ultrapure water. Before cell seeding, hydrogel were washed with 1X PBS.

Cell culture

The mouse myogenic C2C12 cells were maintained as exponentially growing myoblasts in a Growth Medium consisting of Dulbecco's Modified Eagle's Medium (DMEM) supplemented with 20% heat-inactivated fetal calf serum, 4 mM $_{L}$-glutamine, 100 IU/mL penicillin and 100 μg/mL streptomycin. Cells were seeded at a density of 10^4 cells/cm^2.

To obtain cell differentiation and myotube fusion, cells were seeded at a density of $5x10^3$ cells/cm^2. 48 hours after seeding, cells were shifted to Differentiation Medium, consisting of DMEM supplemented with 2% heat-inactivated horse serum, 4mM glutamine, 100 IU/mL penicillin and 100 μg/mL streptomycin. Due to myotube contraction, after 7-8 days in Differentiation Medium, cells started to peel and detach from coverslips.

Antibodies and fluorochromes

Anti-vinculin antibody (mouse monoclonal anti-vinculin, V9131, Sigma-Aldrich, St. Louis, MQ) at 1:200 dilution. Goat anti-mouse fluorescein isothiocyanate (FITC) antibody, F0257 (Sigma-Aldrich) at 1:50 dilution. DAPI (4',6-diamidino-2-phenylindole, Sigma-Aldrich) was employed at 100 ng/mL. Alexa Fluor 594 phalloidin (Molecular Probes, Eugene, OR) was employed at 0.008 U/coverslip.

Immunofluorescence

Samples were washed three times with 1X PBS and then fixed with 4% PFA for 30 minutes at 4 °C. After fixing, samples were blocked with a solution including 1-5% normal goat serum, 0.1% Triton-X 100 in 1X PBS for 10 minutes. Samples were incubated overnight at 4 °C with a primary antibody at the appropriate dilution. After three washes of 10 minutes with a washing solution (0.1% Triton-X 100 in 1X PBS), coverslips were incubated with secondary antibody (or other fluorochromes) for 2 hour at 4 °C. Samples was washed again with washing solution. After they were mouted onto slides and visualized under a Leica DMLS fluorescence microscope (Leica Microsystems, Wetzlar, German).

Ca^{2+} imaging

Cells were seeded at $5x10^3$ cells/cm^2 onto control and HELPs-coated coverslips. 48 hours after seeding, the medium was substituted to Differentiation Medium. At various days of differentiation (from 1 to 5 days), samples were bathed three times with a Normal Extracellular Saline (NES, 140 NaCl, 2.8KCl, 2 $CaCl_2$, 5 $MgCl_2$, 10 glucose, 10 HEPES in mM, pH 7.4). For fura2-AM loading, NES was added with 1% BSA and cells were loaded at RT with a mixture (1:2, vol:vol) of 2 μM, final concentration, fura2-AM (Sigma-Aldrich) and 20% Pluronic gel (Molecular probes, Eugene, OR; 0.04%, final concentration). After 30 minutes, the loading solution was removed and cells were washed in NES for 15 minutes to allow complete de-esterification of the dye. Video microscopy and Ca^{2+} measured was performed at RT. The fura-2 loaded coverslips were set on the inverted microscope (Zeiss Axiovert 35, Carl Zeiss, Jena, German). Wavelengths between 340 and 380 nm were used in order to excite the cells with a monochromatic device equipped with integrated light source (Polychrome IV, Till Photonics, Gräfelfing,Germany). Recordings were carried out at a frequency of one image per second using an IMAGO CCD camera (Till Photonics) and at the same time displayed on a 24 inch Samsung color monitor. The imaging system was controlled by an integrating imaging software package (TILLvisION, Till Photonics) using a personal computer. Therefore, video frames were the digitized, integrated and processed offline to convert fluorescence data into Ca^{2+} maps by computing a ratio of 340/380 nm excitation wavelength values. Temporal plots, representing the mean value of the fluorescence signal in areas of interest, were evaluated from ratio images, thus providing quantitative temporal analysis of spontaneous or evoked signals. Stimulations were carried out under continuous fluid flow of 2 mL/min. The stimulation protocol begun by perfusing cells with ethylene glycol tetra-acetic acid (EGTA) at a 2 mM concentration, dissolved in Ca^{2+}-free NES: under these condition Ca^{2+} influx from the extracellular fluid is totally prevented. Cell depolarization was obtained by perfusing the cells with 60 mM KCl-NES, isosmotic for NaCl substitution. Opening of the ryanodine receptor channel was induced with 20 mM caffeine. All drugs where diluted with recording solution to final concentrations. The inflow pipette was placed in the proximity (100 μm) of the stimulated cells, and an outflow port was positioned 1 cm apart, along the direction of the flow. Intracellular Ca^{2+} transients were considered significant if they exceeded five times the SD of the baseline noise.

Atomic force spectroscopy imaging and force spectroscopy of HELPs coating

AFM was used to characterize in thickness and morphology HELPs coating before cell seeding, to acquire three-dimensional reconstruction of myotubes grown on different HELPs substrates and to perform cell mechanic characterization. AFM images were acquired using a commercially available microscope (Asylum Research MFP-3D^{TM} Stand Alone AFM from Oxford Instruments, Santa Barbara, CA – U.S.) endowed with 90 x 90 x 15 μm closed loop metrological scanner. All AFM measurements were carried out at room temperature working in dynamic mode in air. HELPc coated glasses were imaged using cantilevers characterized by a resonance frequency of about 65 kHz and a force constant of about 0.6 nN/nm (HQ:NSC36/C from MikroMasch Co. – Tallinn- Estonia). 512 x 512 pixels images were acquired at 0.7 lines/second scan speed to asses HELPc film morphology. The thickness of HELPs coatings was calculated as height difference between the film upper surface and the underneath glass surface previously exposed by scratching away the coating with a scalpel. Single heights were evaluated as average of 6/8 measurements along a single scratch line. For a more accurate measure of HELPc coating, films thickness was determined by removing the polypeptide film on a 1x1 μm^2 portion of the sample, with the purpose to expose the flat underlying glass support. Holes in the film were realized using the same cantilever in static mode (constant force) with a set point of about 100 nN (256 x 256 pixels images at 2 lines/second speed). Line profiling and height distribution analysis were subsequently performed on a larger image including the so obtained hole to extrapolate film thickness information.

For cellular characterization, myotubes developed on the different substrates were washed three times with PBS, fixed with 4% PFA for 30 minutes at 4 °C. After fixing, PFA was removed by three more washes with 1X PBS and samples were stored at 4 °C. Before AFM characterization, samples were rinsed with deionized water, dehydrated in absolute ethanol and gently dried in a nitrogen box. In control (glass substrate) and HELPs samples (HELP, HELP1, HELPc), single cells were imaged via AFM in order to determine their height relatively to the supporting substrate. Cantilevers, characterized by a resonance frequency of about 90 kHz (NSG30 tips from NT-MDT Co. –Moscow-Russia) were used working at low oscillation amplitudes with half free-amplitude set-point. High-resolution images (512x512 pixels frames) were acquired at 1.4 lines/second scan speed. Myotubes' height was determined from AFM three-dimensional

reconstructions. Line profiling was used to assess the difference in height between myotubes summit and the surrounding cellular carpet. AFM elastic assessment of stiffness was done taking advantage of the distinctive force spectroscopy capabilities of the MFP-3D^{TM} AFM. In brief, force spectroscopy measures the deflection of an AFM cantilever while it is pushed to a surface. These data were subsequently converted in a force/indentation curve via cantilever spring constant and displacement knowledge [240]. Compliance of the material under the tip may be determined fitting the data with a Herztian model of surface indentation [241]. AFM indentation were performed positioning the tip apex on the larger and thicker part of myotubes, as determined by optical visualization. Cantilever used was a 40 nm tip radius probe characterized by a spring constant of about 0.50 nN/nm (HQ:NSC19/Cr/Au tips from MikroMasch Co.- Tallinn-Estonia). Force spectroscopy measurements were performed at constant speed (1 μm/s) and triggered to a maximum sample indentation of 150 nm, equal to about 10% of total cell height (1.40±0.45 μm, determined from AFM imaging). For each myotube 3 force spectroscopies were acquired: the first was rejected to allow tip stabilization, while the second was considered reliable if t differed less than 5% from the third. Elastic modulus values (E), in kPa, were determined by fitting the Hertz model for the tip used taking advantage of MFP-3D^{TM} control and analysis software. Particular effort was done in choosing isolated myotubes with comparable elongated morphology. Gwyddion software (www.gwyddion.net) was used to analyze AFM images while all statistics and data processing were performed using Igor Pro software (www.wavematrics.com).

Atomic force spectroscopy imaging and of HELPc hydrogel

AFM was used to characterize HELPc dehydrated hydrogels' thickness and morphology. AFM images were acquired using a commercially available microscope (Asylum Research MFP-3D^{TM} Stand Alone AFM; Oxford Instruments, Santa Barbara, CA, USA) endowed with a 90 x 90 x15 μm closed-loop metrological scanner. All AFM measurements were carried out in air at room temperature working in dynamic mode. HELPc hydrogels were carefully washed using Milli-Q water and gently dried in a nitrogen oven overnight at room temperature. Cantilevers used were characterized by a free resonance frequency of about 65 kHz and a force costant of about 0.6 nN/nm (HQ:NSC36/C; MikroMasch Co., Tallinn, Estonia). Images of 512 x 512 pixels were acquired at 0.5 lines/s scan speed to assess the morphology of dehydrated hydrogels. Thickness

was calculated as height difference between the film upper surface and the glass surface underneath previously exposed by scratching away the gel with a scalpel. Heights were evaluated as mean value of 10 height profile traced in different positions perpendicularly to a single scratch line. Gwyddion software was used to analyzed AFM images and to compute surface roughness (R_a), while all statistics and data processing were performed using Igor Pro software.

Bibliography

1. Wang, J.; Lü, D.; Mao, D.; Long, M. Mechanomics: an emerging field between biology and biomechanics. *Protein Cell* **2014**, *5*, 518–31.
2. Rianna, C.; Kumar, P.; Radmacher, M. The role of the microenvironment in the biophysics of cancer. *Semin. Cell Dev. Biol.* **2017**.
3. Clause, K. C.; Barker, T. H. Extracellular matrix signaling in morphogenesis and repair. *Curr. Opin. Biotechnol.* **2013**, *24*, 830–833.
4. Haase, K.; Al-Rekabi, Z.; Pelling, A. E. Mechanical Cues Direct Focal Adhesion Dynamics. In; 2014; pp. 103–134.
5. Theocharis, A. D.; Skandalis, S. S.; Neill, T.; Multhaupt, H. A. B.; Hubo, M.; Frey, H.; Gopal, S.; Gomes, A.; Afratis, N.; Lim, H. C.; Couchman, J. R.; Filmus, J.; Sanderson, R. D.; Schaefer, L.; Iozzo, R. V; Karamanos, N. K. Insights into the key roles of proteoglycans in breast cancer biology and translational medicine. *Biochim. Biophys. Acta* **2015**, *1855*, 276–300.
6. Kadler, K. E.; Baldock, C.; Bella, J.; Boot-Handford, R. P. Collagens at a glance. *J. Cell Sci.* **2007**, *120*, 1955–1958.
7. Bonnans, C.; Chou, J.; Werb, Z. Remodelling the extracellular matrix in development and disease. *Nat. Rev. Mol. Cell Biol.* **2014**, *15*, 786–801.
8. Ma, H.; Killaars, A. R.; DelRio, F. W.; Yang, C.; Anseth, K. S. Myofibroblastic activation of valvular interstitial cells is modulated by spatial variations in matrix elasticity and its organization. *Biomaterials* **2017**, *131*, 131–144.
9. Wagenseil, J. E.; Mecham, R. P. New insights into elastic fiber assembly. *Birth Defects Res. Part C Embryo Today Rev.* **2007**, *81*, 229–240.
10. Bax, D. V; Bernard, S. E.; Lomas, A.; Morgan, A.; Humphries, J.; Shuttleworth, C. A.; Humphries, M. J.; Kielty, C. M. Cell adhesion to fibrillin-1 molecules and microfibrils is mediated by alpha 5 beta 1 and alpha v beta 3 integrins. *J. Biol. Chem.* **2003**, *278*, 34605–16.
11. Theocharis, A. D.; Skandalis, S. S.; Gialeli, C.; Karamanos, N. K. Extracellular matrix structure. *Adv. Drug Deliv. Rev.* **2016**, *97*, 4–27.
12. Moretti, F. A.; Chauhan, A. K.; Iaconcig, A.; Porro, F.; Baralle, F. E.; Muro, A. F. A major fraction of fibronectin present in the extracellular matrix of tissues is plasma-derived. *J. Biol. Chem.* **2007**, *282*, 28057–62.
13. Miner, J. H.; Yurchenco, P. D. LAMININ FUNCTIONS IN TISSUE MORPHOGENESIS. *Annu. Rev. Cell Dev. Biol.* **2004**, *20*, 255–284.
14. Rozario, T.; DeSimone, D. W. The extracellular matrix in development and morphogenesis: A dynamic view. *Dev. Biol.* **2010**, *341*, 126–140.
15. Takagi, J. Structure of integrin 5 1 in complex with fibronectin. *EMBO J.* **2003**, *22*, 4607–4615.
16. Haase, K.; Pelling, A. E. Investigating cell mechanics with atomic force microscopy. *J. R. Soc. Interface* **2015**, *12*, 20140970–20140970.
17. Lodish H, Berk A, Zipursky SL, et al. Section 18.2, The Dynamics of Actin Assembly. In *Molecular Cell Biology. 4th edition.*; 2000.
18. Guolla, L.; Bertrand, M.; Haase, K.; Pelling, A. E. Force transduction and strain dynamics in actin stress fibres in response to nanonewton forces. *J. Cell Sci.* **2012**, *125*, 603–613.
19. GM., C. Microtubules. In *The Cell*; 2000.
20. Burridge, K.; Guilluy, C. Focal adhesions, stress fibers and mechanical tension. *Exp. Cell Res.* **2016**, *343*, 14–20.

21. Al-Rekabi, Z.; Pelling, A. E. Cross talk between matrix elasticity and mechanical force regulates myoblast traction dynamics. *Phys. Biol.* **2013**, *10*, 66003.
22. Haase, K.; Al-Rekabi, Z.; Pelling, A. E. Mechanical cues direct focal adhesion dynamics. *Prog. Mol. Biol. Transl. Sci.* **2014**, *126*, 103–34.
23. Giannone, G.; Sheetz, M. P. Substrate rigidity and force define form through tyrosine phosphatase and kinase pathways. *Trends Cell Biol.* **2006**, *16*, 213–23.
24. Elosegui-Artola, A.; Oria, R.; Chen, Y.; Kosmalska, A.; Pérez-González, C.; Castro, N.; Zhu, C.; Trepat, X.; Roca-Cusachs, P. Mechanical regulation of a molecular clutch defines force transmission and transduction in response to matrix rigidity. *Nat. Cell Biol.* **2016**, *18*, 540–548.
25. Tepass, U. FERM proteins in animal morphogenesis. *Curr. Opin. Genet. Dev.* **2009**, *19*, 357–367.
26. Swaminathan, V.; Waterman, C. M. The molecular clutch model for mechanotransduction evolves. *Nat. Cell Biol.* **2016**, *18*, 459–461.
27. Nagasato, A. I.; Yamashita, H.; Matsuo, M.; Ueda, K.; Kioka, N. The distribution of vinculin to lipid rafts plays an important role in sensing stiffness of extracellular matrix. *Biosci. Biotechnol. Biochem.* **2017**, *8451*, 1–12.
28. Grashoff, C.; Hoffman, B. D.; Brenner, M. D.; Zhou, R.; Parsons, M.; Yang, M. T.; Mclean, M. A.; Sligar, S. G.; S, C.; Ha, T.; Schwartz, M. A.; Berne, R. M. Regulation of Focal Adhesion Dynamics. **2011**, *466*, 263–266.
29. Devreotes, P.; Horwitz, A. R. Signaling Networks that Regulate Cell Migration. *Cold Spring Harb. Perspect. Biol.* **2015**, *7*, a005959.
30. Mierke, C. T. The role of focal adhesion kinase in the regulation of cellular mechanical properties. *Phys. Biol.* **2013**, *10*, 65005.
31. Hong, S.-Y.; Jeon, Y.-M.; Lee, H.-J.; Kim, J.-G.; Baek, J.-A.; Lee, J.-C. Activation of RhoA and FAK induces ERK-mediated osteopontin expression in mechanical force-subjected periodontal ligament fibroblasts. *Mol. Cell. Biochem.* **2010**, *335*, 263–72.
32. Hotulainen, P.; Lappalainen, P. Stress fibers are generated by two distinct actin assembly mechanisms in motile cells. *J. Cell Biol.* **2006**, *173*, 383–94.
33. Crisp, M.; Liu, Q.; Roux, K.; Rattner, J. B.; Shanahan, C.; Burke, B.; Stahl, P. D.; Hodzic, D. Coupling of the nucleus and cytoplasm. *J. Cell Biol.* **2006**, *172*, 41–53.
34. Luxton, G. W. G.; Gomes, E. R.; Folker, E. S.; Vintinner, E.; Gundersen, G. G. Linear arrays of nuclear envelope proteins harness retrograde actin flow for nuclear movement. *Science* **2010**, *329*, 956–9.
35. Maninova, M.; Caslavsky, J.; Vomastek, T. The assembly and function of perinuclear actin cap in migrating cells. *Protoplasma* **2017**, *254*, 1207–1218.
36. Hakkinen, K. M.; Harunaga, J. S.; Doyle, A. D.; Yamada, K. M. Direct Comparisons of the Morphology, Migration, Cell Adhesions, and Actin Cytoskeleton of Fibroblasts in Four Different Three-Dimensional Extracellular Matrices. *Tissue Eng. Part A* **2011**, *17*, 713–724.
37. Luo, Q.; Kuang, D.; Zhang, B.; Song, G. Cell stiffness determined by atomic force microscopy and its correlation with cell motility. *Biochim. Biophys. Acta* **2016**, *1860*, 1953–60.
38. Connelly, J. T.; Gautrot, J. E.; Trappmann, B.; Tan, D. W.-M.; Donati, G.; Huck, W. T. S.; Watt, F. M. Actin and serum response factor transduce physical cues from the microenvironment to regulate epidermal stem cell fate decisions. *Nat. Cell Biol.* **2010**, *12*, 711–718.
39. Dechat, T.; Pfleghaar, K.; Sengupta, K.; Shimi, T.; Shumaker, D. K.; Solimando, L.; Goldman, R. D. Nuclear lamins: major factors in the structural organization and function of the nucleus and chromatin. *Genes Dev.* **2008**, *22*, 832–853.
40. Swift, J.; Ivanovska, I. L.; Buxboim, A.; Harada, T.; Dingal, P. C. D. P.; Pinter, J.;

Pajerowski, J. D.; Spinler, K. R.; Shin, J.-W.; Tewari, M.; Rehfeldt, F.; Speicher, D. W.; Discher, D. E. Nuclear lamin-A scales with tissue stiffness and enhances matrix-directed differentiation. *Science* **2013**, *341*, 1240104.
41. Gerlitz, G.; Bustin, M. The role of chromatin structure in cell migration. *Trends Cell Biol.* **2011**, *21*, 6–11.
42. Jansen, K. A.; Donato, D. M.; Balcioglu, H. E.; Schmidt, T.; Danen, E. H. J.; Koenderink, G. H. A guide to mechanobiology: Where biology and physics meet. *Biochim. Biophys. Acta* **2015**, *1853*, 3043–52.
43. Pan, D. The Hippo Signaling Pathway in Development and Cancer. *Dev. Cell* **2010**, *19*, 491–505.
44. Panciera, T.; Azzolin, L.; Cordenonsi, M.; Piccolo, S. Mechanobiology of YAP and TAZ in physiology and disease. *Nat. Rev. Mol. Cell Biol.* **2017**, nrm.2017.87.
45. Zhao, B.; Li, L.; Wang, L.; Wang, C.-Y.; Yu, J.; Guan, K.-L. Cell detachment activates the Hippo pathway via cytoskeleton reorganization to induce anoikis. *Genes Dev.* **2012**, *26*, 54–68.
46. Praskova, M.; Xia, F.; Avruch, J. MOBKL1A/MOBKL1B Phosphorylation by MST1 and MST2 Inhibits Cell Proliferation. *Curr. Biol.* **2008**, *18*, 311–321.
47. Yin, F.; Yu, J.; Zheng, Y.; Chen, Q.; Zhang, N.; Pan, D. Spatial organization of Hippo signaling at the plasma membrane mediated by the tumor suppressor Merlin/NF2. *Cell* **2013**, *154*, 1342–55.
48. Zhao, B.; Li, L.; Tumaneng, K.; Wang, C.-Y.; Guan, K.-L. A coordinated phosphorylation by Lats and CK1 regulates YAP stability through SCF -TRCP. *Genes Dev.* **2010**, *24*, 72–85.
49. Mo, J.-S. The role of extracellular biophysical cues in modulating the Hippo-YAP pathway. *BMB Rep.* **2017**, *50*, 71–78.
50. Zhao, B.; Ye, X.; Yu, J.; Li, L.; Li, W.; Li, S.; Yu, J.; Lin, J. D.; Wang, C.-Y.; Chinnaiyan, A. M.; Lai, Z.-C.; Guan, K.-L. TEAD mediates YAP-dependent gene induction and growth control. *Genes Dev.* **2008**, *22*, 1962–71.
51. Wada, K.-I.; Itoga, K.; Okano, T.; Yonemura, S.; Sasaki, H. Hippo pathway regulation by cell morphology and stress fibers. *Development* **2011**, *138*, 3907–3914.
52. Codelia, V. A.; Sun, G.; Irvine, K. D. Regulation of YAP by mechanical strain through Jnk and Hippo signaling. *Curr. Biol.* **2014**, *24*, 2012–7.
53. Ridley, A. J. Rho GTPases and actin dynamics in membrane protrusions and vesicle trafficking. *Trends Cell Biol.* **2006**, *16*, 522–529.
54. Kaunas, R.; Nguyen, P.; Usami, S.; Chien, S. Cooperative effects of Rho and mechanical stretch on stress fiber organization. *Proc. Natl. Acad. Sci. U. S. A.* **2005**, *102*, 15895–900.
55. Cook, D. R.; Rossman, K. L.; Der, C. J. Rho guanine nucleotide exchange factors: regulators of Rho GTPase activity in development and disease. *Oncogene* **2014**, *33*, 4021–4035.
56. Lessey, E. C.; Guilluy, C.; Burridge, K. From Mechanical Force to RhoA Activation. *Biochemistry* **2012**, *51*, 7420–7432.
57. Dupont, S.; Morsut, L.; Aragona, M.; Enzo, E.; Giulitti, S.; Cordenonsi, M.; Zanconato, F.; Le Digabel, J.; Forcato, M.; Bicciato, S.; Elvassore, N.; Piccolo, S. Role of YAP/TAZ in mechanotransduction. *Nature* **2011**, *474*, 179–183.
58. Hao, J.; Zhang, Y.; Ye, R.; Zheng, Y.; Zhao, Z.; Li, J. Mechanotransduction in cancer stem cells. *Cell Biol. Int.* **2013**, *37*, 888–891.
59. Calvo, F.; Ege, N.; Grande-Garcia, A.; Hooper, S.; Jenkins, R. P.; Chaudhry, S. I.; Harrington, K.; Williamson, P.; Moeendarbary, E.; Charras, G.; Sahai, E. Mechanotransduction and YAP-dependent matrix remodelling is required for the generation and maintenance of cancer-associated fibroblasts. *Nat. Cell Biol.* **2013**, *15*, 637–646.

60. Neuman, K. C.; Nagy, A. Single-molecule force spectroscopy: optical tweezers, magnetic tweezers and atomic force microscopy. *Nat. Methods* **2008**, *5*, 491–505.
61. Keyser, U. F.; Koeleman, B. N.; van Dorp, S.; Krapf, D.; Smeets, R. M. M.; Lemay, S. G.; Dekker, N. H.; Dekker, C. Direct force measurements on DNA in a solid-state nanopore. *Nat. Phys.* **2006**, *2*, 473–477.
62. Kuo, S. C.; Sheetz, M. P. Optical tweezers in cell biology. *Trends Cell Biol.* **1992**, *2*, 116–8.
63. Longo, M. L.; Ly, H. V. Micropipet Aspiration for Measuring Elastic Properties of Lipid Bilayers. In *Methods in molecular biology (Clifton, N.J.)*; 2007; Vol. 400, pp. 421–437.
64. Lee, L. M.; Liu, A. P. The Application of Micropipette Aspiration in Molecular Mechanics of Single Cells. *J. Nanotechnol. Eng. Med.* **2014**, *5*, 40902.
65. Korin, N.; Bransky, A.; Dinnar, U. Theoretical model and experimental study of red blood cell (RBC) deformation in microchannels. *J. Biomech.* **2007**, *40*, 2088–2095.
66. Kiesewetter, H.; Dauer, U.; Teitel, P.; Schmid-Schönbein, H.; Trapp, R. The single erythrocyte rigidometer (SER) as a reference for RBC deformability. *Biorheology* **1982**, *19*, 737–53.
67. Tseng, P.; Judy, J. W.; Di Carlo, D. Magnetic nanoparticle-mediated massively parallel mechanical modulation of single-cell behavior. *Nat. Methods* **2012**, *9*, 1113–9.
68. JPK instruments A pratical guide to AFM force spectroscopy and data analysis http://www.jpk.com/app-technotes-img/AFM/pdf/jpk-tech-force-spectroscopy.14-2.pdf (accessed Oct 19, 2017).
69. Kaufman, A. M.; Lester, B. J.; Regal, C. A. Cooling a Single Atom in an Optical Tweezer to Its Quantum Ground State. *Phys. Rev. X* **2012**, *2*, 41014.
70. Unal, M.; Alapan, Y.; Jia, H.; Varga, A. G.; Angelino, K.; Aslan, M.; Sayin, I.; Han, C.; Jiang, Y.; Zhang, Z.; Gurkan, U. A. Micro and Nano-Scale Technologies for Cell Mechanics. *Nanobiomedicine* **2014**, *1*, 5.
71. Esch, E. W.; Bahinski, A.; Huh, D. Organs-on-chips at the frontiers of drug discovery. *Nat. Rev. Drug Discov.* **2015**, *14*, 248–260.
72. Meyer, G.; Amer, N. M. Novel optical approach to atomic force microscopy. *Appl. Phys. Lett.* **1988**, *53*, 1045–1047.
73. Piezo Response Imaging— A Crosspoint Switch Example Using the MFP-3D Atomic Force Microscope (AFM) from Asylum Research https://www.azom.com/article.aspx?ArticleID=3512 (accessed Nov 28, 2017).
74. Kasas, S.; Stupar, P.; Dietler, G. AFM contribution to unveil pro- and eukaryotic cell mechanical properties. *Semin. Cell Dev. Biol.* **2017**.
75. Shin, D.; Athanasiou, K. Cytoindentation for obtaining cell biomechanical properties. *J. Orthop. Res.* **1999**, *17*, 880–90.
76. Atkins, A. G.; Tabor, D. Plastic indentation in metals with cones. *J. Mech. Phys. Solids* **1965**, *13*, 149–164.
77. Chen, J. Nanobiomechanics of living cells: a review. *Interface Focus* **2014**, *4*, 20130055–20130055.
78. Alessandrini, A.; Facci, P. AFM: a versatile tool in biophysics. *Meas. Sci. Technol.* **2005**, *16*, R65–R92.
79. Santos, N. C.; Castanho, M. A. R. B. An overview of the biophysical applications of atomic force microscopy. *Biophys. Chem.* **2004**, *107*, 133–149.
80. Liu, H.; Sun, Y.; Simmons, C. A. Determination of local and global elastic moduli of valve interstitial cells cultured on soft substrates. *J. Biomech.* **2013**, *46*, 1967–1971.
81. Plodinec, M.; Loparic, M.; Monnier, C. A.; Obermann, E. C.; Zanetti-Dallenbach, R.; Oertle,

P.; Hyotyla, J. T.; Aebi, U.; Bentires-Alj, M.; Lim, R. Y. H.; Schoenenberger, C.-A. The nanomechanical signature of breast cancer. *Nat. Nanotechnol.* **2012**, *7*, 757–765.
82. Rianna, C.; Radmacher, M. Cell mechanics as a marker for diseases: Biomedical applications of AFM. In; 2016; p. 20057.
83. X. Liang, X. Shi, S. Ostrovidov, H. Wu, K. N. Probing stem cell differentiation using atomic force microscopy. *Appl. Surf. Sci.* **2016**, *366*, 254–259.
84. D'Andrea, P.; Scaini, D.; Severino, L. U.; Borelli, V.; Passamonti, S.; Lorenzon, P.; Bandiera, A. In vitro Myogenesis induced by Human Recombinant Elastin-Like Proteins. *Biomaterials* **2015**.
85. Simon, M.; Dokukin, M.; Kalaparthi, V.; Spedden, E.; Sokolov, I.; Staii, C. Load Rate and Temperature Dependent Mechanical Properties of the Cortical Neuron and Its Pericellular Layer Measured by Atomic Force Microscopy. *Langmuir* **2016**, *32*, 1111–1119.
86. Fallqvist, B.; Fielden, M. L.; Pettersson, T.; Nordgren, N.; Kroon, M.; Gad, A. K. B. Experimental and computational assessment of F-actin influence in regulating cellular stiffness and relaxation behaviour of fibroblasts. *J. Mech. Behav. Biomed. Mater.* **2016**, *59*, 168–184.
87. Wu, X.; Muthuchamy, M.; Reddy, D. S. Atomic Force Microscopy Protocol for Measurement of Membrane Plasticity and Extracellular Interactions in Single Neurons in Epilepsy. *Front. Aging Neurosci.* **2016**, *8*, 88.
88. Lekka, M. Discrimination Between Normal and Cancerous Cells Using AFM. *Bionanoscience* **2016**, *6*, 65–80.
89. Coceano, G.; Yousafzai, M. S.; Ma, W.; Ndoye, F.; Venturelli, L.; Hussain, I.; Bonin, S.; Niemela, J.; Scoles, G.; Cojoc, D.; Ferrari, E. Investigation into local cell mechanics by atomic force microscopy mapping and optical tweezer vertical indentation. *Nanotechnology* **2016**, *27*, 65102.
90. Ansardamavandi, A.; Tafazzoli-Shadpour, M.; Omidvar, R.; Jahanzad, I. Quantification of effects of cancer on elastic properties of breast tissue by Atomic Force Microscopy. *J. Mech. Behav. Biomed. Mater.* **2016**, *60*, 234–242.
91. Maherally, Z.; Smith, J. R.; Ghoneim, M. K.; Dickson, L.; An, Q.; Fillmore, H. L.; Pilkington, G. J. Silencing of CD44 in Glioma Leads to Changes in Cytoskeletal Protein Expression and Cellular Biomechanical Deformation Properties as Measured by AFM Nanoindentation. *Bionanoscience* **2016**, *6*, 54–64.
92. Holtzmann, K.; Gautier, H. O. B.; Christ, A. F.; Guck, J.; Káradóttir, R. T.; Franze, K. Brain tissue stiffness is a sensitive marker for acidosis. *J. Neurosci. Methods* **2016**, *271*, 50–54.
93. Acerbi, I.; Cassereau, L.; Dean, I.; Shi, Q.; Au, A.; Park, C.; Chen, Y. Y.; Liphardt, J.; Hwang, E. S.; Weaver, V. M. Human breast cancer invasion and aggression correlates with ECM stiffening and immune cell infiltration. *Integr. Biol.* **2015**, *7*, 1120–1134.
94. Elkin, B. S.; Ilankovan, A.; Morrison, B. Age-dependent regional mechanical properties of the rat hippocampus and cortex. *J. Biomech. Eng.* **2010**, *132*, 11010.
95. Luque, T.; Kang, M. S.; Schaffer, D. V.; Kumar, S. Microelastic mapping of the rat dentate gyrus. *R. Soc. Open Sci.* **2016**, *3*, 150702.
96. Koser, D. E.; Moeendarbary, E.; Hanne, J.; Kuerten, S.; Franze, K. CNS cell distribution and axon orientation determine local spinal cord mechanical properties. *Biophys. J.* **2015**, *108*, 2137–47.
97. Moeendarbary, E.; Weber, I. P.; Sheridan, G. K.; Koser, D. E.; Soleman, S.; Haenzi, B.; Bradbury, E. J.; Fawcett, J.; Franze, K. The soft mechanical signature of glial scars in the central nervous system. *Nat. Commun.* **2017**, *8*, 14787.
98. Jorba, I.; Menal, M. J.; Torres, M.; Gozal, D.; Piñol-Ripoll, G.; Colell, A.; Montserrat, J. M.;

Navajas, D.; Farré, R.; Almendros, I. Ageing and chronic intermittent hypoxia mimicking sleep apnea do not modify local brain tissue stiffness in healthy mice. *J. Mech. Behav. Biomed. Mater.* **2017**, *71*, 106–113.
99. Liu, F.; Mih, J. D.; Shea, B. S.; Kho, A. T.; Sharif, A. S.; Tager, A. M.; Tschumperlin, D. J. Feedback amplification of fibrosis through matrix stiffening and COX-2 suppression. *J. Cell Biol.* **2010**, *190*, 693–706.
100. Sader, J. E.; Chon, J. W. M.; Mulvaney, P. Calibration of rectangular atomic force microscope cantilevers. *http://oasc12039.247realmedia.com/RealMedia/ads/click_lx.ads/www.aip.org/pt/adcenter/pdfcover_test/L-37/988558375/x01/AIP-PT/MCL_RSIArticleDL_111517/MCL_banner.jpg/434f71374e315a556e61414141774c75?x* **1999**.
101. Demichelis, A.; Divieto, C.; Mortati, L.; Pavarelli, S.; Sassi, G.; Sassi, M. P. Toward the realization of reproducible Atomic Force Microscopy measurements of elastic modulus in biological samples. *J. Biomech.* **2015**, *48*, 1099–104.
102. Lin, D. C.; Shreiber, D. I.; Dimitriadis, E. K.; Horkay, F. Spherical indentation of soft matter beyond the Hertzian regime: numerical and experimental validation of hyperelastic models. *Biomech. Model. Mechanobiol.* **2009**, *8*, 345–58.
103. Chen, J.; Lu, G. Finite element modelling of nanoindentation based methods for mechanical properties of cells. *J. Biomech.* **2012**, *45*, 2810–6.
104. Sweers, K. K. M.; Bennink, M. L.; Subramaniam, V. Nanomechanical properties of single amyloid fibrils. *J. Phys. Condens. Matter* **2012**, *24*, 243101.
105. Zhu, X.; Siamantouras, E.; Liu, K. K.; Liu, X. Determination of work of adhesion of biological cell under AFM bead indentation. *J. Mech. Behav. Biomed. Mater.* **2016**, *56*, 77–86.
106. Panagiotopoulou, O. Finite element analysis (FEA): Applying an engineering method to functional morphology in anthropology and human biology. *Ann. Hum. Biol.* **2009**, *36*, 609–623.
107. Misfeld, M.; Sievers, H.-H. Heart valve macro- and microstructure. *Philos. Trans. R. Soc. Lond. B. Biol. Sci.* **2007**, *362*, 1421–36.
108. Rabkin, E.; Aikawa, M.; Stone, J. R.; Fukumoto, Y.; Libby, P.; Schoen, F. J. Activated interstitial myofibroblasts express catabolic enzymes and mediate matrix remodeling in myxomatous heart valves. *Circulation* **2001**, *104*, 2525–32.
109. Sacks, M. S.; David Merryman, W.; Schmidt, D. E. On the biomechanics of heart valve function. *J. Biomech.* **2009**, *42*, 1804–1824.
110. Schoen, F. J. Evolving concepts of cardiac valve dynamics: the continuum of development, functional structure, pathobiology, and tissue engineering. *Circulation* **2008**, *118*, 1864–80.
111. Tompkins, R. G.; Schnitzer, J. J.; Yarmush, M. L. Macromolecular transport within heart valves. *Circ. Res.* **1989**, *64*, 1213–23.
112. Chen, J. H.; Simmons, C. A. Cell-matrix interactions in the pathobiology of calcific aortic valve disease: Critical roles for matricellular, matricrine, and matrix mechanics cues. *Circ. Res.* **2011**, *108*, 1510–1524.
113. Lindman, B. R.; Clavel, M.-A.; Mathieu, P.; Iung, B.; Lancellotti, P.; Otto, C. M.; Pibarot, P. Calcific aortic stenosis. *Nat. Rev. Dis. Prim.* **2016**, *2*, 16006.
114. Otto, C. M.; Prendergast, B. Aortic-Valve Stenosis — From Patients at Risk to Severe Valve Obstruction. *N. Engl. J. Med.* **2014**, *371*, 744–756.
115. Towler, D. A. Molecular and Cellular Aspects of Calcific Aortic Valve Disease. *Circ. Res.* **2013**, *113*, 198–208.
116. Rajamannan, N. M.; Subramaniam, M.; Rickard, D.; Stock, S. R.; Donovan, J.; Springett,

M.; Orszulak, T.; Fullerton, D. A.; Tajik, A. J.; Bonow, R. O.; Spelsberg, T. Human aortic valve calcification is associated with an osteoblast phenotype. *Circulation* **2003**, *107*, 2181–4.
117. Chen, W. L. K.; Simmons, C. A. Lessons from (patho)physiological tissue stiffness and their implications for drug screening, drug delivery and regenerative medicine. *Adv. Drug Deliv. Rev.* **2011**, *63*, 269–276.
118. Chen, J. H.; Chen, W. L. K.; Sider, K. L.; Yip, C. Y. Y.; Simmons, C. A. ??-Catenin Mediates Mechanically Regulated, Transforming Growth Factor-??1-Induced Myofibroblast Differentiation of Aortic Valve Interstitial Cells. *Arterioscler. Thromb. Vasc. Biol.* **2011**, *31*, 590–597.
119. Manuscript, A.; Nanostructures, S. P. C. NIH Public Access. *Nano* **2008**, *6*, 2166–2171.
120. Changes, A.; The, I. N.; Valves, M. I904.1. **1964**.
121. Liu, F.; Mih, J. D.; Shea, B. S.; Kho, A. T.; Sharif, A. S.; Tager, A. M.; Tschumperlin, D. J. Feedback amplification of fibrosis through matrix stiffening and COX-2 suppression. *J. Cell Biol.* **2010**, *190*, 693–706.
122. Wyss, K.; Yip, C. Y. Y.; Mirzaei, Z.; Jin, X.; Chen, J. H.; Simmons, C. A. The elastic properties of valve interstitial cells undergoing pathological differentiation. *J. Biomech.* **2012**, *45*, 882–887.
123. Merryman, W. D. Correlation between heart valve interstitial cell stiffness and transvalvular pressure: implications for collagen biosynthesis. *AJP Hear. Circ. Physiol.* **2005**, *290*, H224–H231.
124. Huang, S.; Huang, H.-Y. S. Biaxial stress relaxation of semilunar heart valve leaflets during simulated collagen catabolism: Effects of collagenase concentration and equibiaxial strain state. *Proc. Inst. Mech. Eng. Part H J. Eng. Med.* **2015**, *229*, 721–731.
125. Yang, C.; DelRio, F. W.; Ma, H.; Killaars, A. R.; Basta, L. P.; Kyburz, K. A.; Anseth, K. S. Spatially patterned matrix elasticity directs stem cell fate. *Proc. Natl. Acad. Sci.* **2016**, *113*, E4439–E4445.
126. Siegel, R.; Naishadham, D.; Jemal, A. Cancer statistics, 2013. *CA. Cancer J. Clin.* **2013**, *63*, 11–30.
127. Egeblad, M.; Nakasone, E. S.; Werb, Z. Tumors as Organs: Complex Tissues that Interface with the Entire Organism. *Dev. Cell* **2010**, *18*, 884–901.
128. Hanahan, D.; Weinberg, R. A. The hallmarks of cancer. *Cell* **2000**, *100*, 57–70.
129. Hanahan, D.; Weinberg, R. A. Hallmarks of Cancer: The Next Generation. *Cell* **2011**, *144*, 646–674.
130. Pickup, M. W.; Mouw, J. K.; Weaver, V. M. The extracellular matrix modulates the hallmarks of cancer. *EMBO Rep.* **2014**, *15*, 1243–1253.
131. Wells, R. G. The role of matrix stiffness in regulating cell behavior. *Hepatology* **2008**, *47*, 1394–1400.
132. Bonnans, C.; Chou, J.; Werb, Z. Remodelling the extracellular matrix in development and disease. *Nat. Rev. Mol. Cell Biol.* **2014**, *15*, 786–801.
133. Lu, P.; Weaver, V. M.; Werb, Z. The extracellular matrix: A dynamic niche in cancer progression. *J. Cell Biol.* **2012**, *196*, 395–406.
134. Nelson, M. T.; Short, A.; Cole, S. L.; Gross, A. C.; Winter, J.; Eubank, T. D.; Lannutti, J. J. Preferential, enhanced breast cancer cell migration on biomimetic electrospun nanofiber "cell highways." *BMC Cancer* **2014**, *14*, 825.
135. Giussani, M.; Merlino, G.; Cappelletti, V.; Tagliabue, E.; Daidone, M. G. Tumor-extracellular matrix interactions: Identification of tools associated with breast cancer progression. *Semin. Cancer Biol.* **2015**, *35*, 3–10.

136. Seewaldt, V. ECM stiffness paves the way for tumor cells. *Nat. Med.* **2014**, *20*, 332–3.
137. Rianna, C.; Kumar, P.; Radmacher, M. The role of the microenvironment in the biophysics of cancer. *Semin. Cell Dev. Biol.* **2017**.
138. Schrader, J.; Gordon-Walker, T. T.; Aucott, R. L.; van Deemter, M.; Quaas, A.; Walsh, S.; Benten, D.; Forbes, S. J.; Wells, R. G.; Iredale, J. P. Matrix stiffness modulates proliferation, chemotherapeutic response, and dormancy in hepatocellular carcinoma cells. *Hepatology* **2011**, *53*, 1192–1205.
139. Kandoth, C.; McLellan, M. D.; Vandin, F.; Ye, K.; Niu, B.; Lu, C.; Xie, M.; Zhang, Q.; McMichael, J. F.; Wyczalkowski, M. A.; Leiserson, M. D. M.; Miller, C. A.; Welch, J. S.; Walter, M. J.; Wendl, M. C.; Ley, T. J.; Wilson, R. K.; Raphael, B. J.; Ding, L. Mutational landscape and significance across 12 major cancer types. *Nature* **2013**, *502*, 333–339.
140. Mantovani, F.; Walerych, D.; Sal, G. Del Targeting mutant p53 in cancer: a long road to precision therapy. *FEBS J.* **2017**, *284*, 837–850.
141. Ashcroft, M.; Vousden, K. H. Regulation of p53 stability. *Oncogene* **1999**, *18*, 7637–7643.
142. Terzian, T.; Suh, Y.-A.; Iwakuma, T.; Post, S. M.; Neumann, M.; Lang, G. A.; Van Pelt, C. S.; Lozano, G. The inherent instability of mutant p53 is alleviated by Mdm2 or p16INK4a loss. *Genes Dev.* **2008**, *22*, 1337–44.
143. Girardini, J. E.; Napoli, M.; Piazza, S.; Rustighi, A.; Marotta, C.; Radaelli, E.; Capaci, V.; Jordan, L.; Quinlan, P.; Thompson, A.; Mano, M.; Rosato, A.; Crook, T.; Scanziani, E.; Means, A. R.; Lozano, G.; Schneider, C.; Del Sal, G. A Pin1/mutant p53 axis promotes aggressiveness in breast cancer. *Cancer Cell* **2011**, *20*, 79–91.
144. Koga, T.; Hashimoto, S.; Sugio, K.; Yoshino, I.; Nakagawa, K.; Yonemitsu, Y.; Sugimachi, K.; Sueishi, K. Heterogeneous distribution of P53 immunoreactivity in human lung adenocarcinoma correlates with MDM2 protein expression, rather than with P53 gene mutation. *Int. J. cancer* **2001**, *95*, 232–9.
145. Bouchalova, P.; Nenutil, R.; Muller, P.; Hrstka, R.; Appleyard, M. V.; Murray, K.; Jordan, L. B.; Purdie, C. A.; Quinlan, P.; Thompson, A. M.; Vojtesek, B.; Coates, P. J. Mutant p53 accumulation in human breast cancer is not an intrinsic property or dependent on structural or functional disruption but is regulated by exogenous stress and receptor status. *J. Pathol.* **2014**, *233*, 238–246.
146. Walerych, D.; Lisek, K.; Del Sal, G. Mutant p53: One, No One, and One Hundred Thousand. *Front. Oncol.* **2015**, *5*, 289.
147. Parrales, A.; Iwakuma, T. Targeting Oncogenic Mutant p53 for Cancer Therapy. *Front. Oncol.* **2015**, *5*, 288.
148. Sorrentino, G.; Ruggeri, N.; Specchia, V.; Cordenonsi, M.; Mano, M.; Dupont, S.; Manfrin, A.; Ingallina, E.; Sommaggio, R.; Piazza, S.; Rosato, A.; Piccolo, S.; Del Sal, G. Metabolic control of YAP and TAZ by the mevalonate pathway. *Nat. Cell Biol.* **2014**, *16*, 357–366.
149. Zanconato, F.; Cordenonsi, M.; Piccolo, S. YAP/TAZ at the Roots of Cancer. *Cancer Cell* **2016**, *29*, 783–803.
150. E. Ingallina, G. Sorrentino, R. Bertolio, K. Lisek, A. Zannini, L. Azzolin, L. Ulloa Severino, D. Scaini, M. Mano, F. Mantovani, A. Rosato, S. Bicciato, S. Piccolo, G. D. S. Mechnical cues control mutant p53 stability throught a Mevalonate/RhoA axis. *Nat. Cell Biol.* **2017**.
151. Bentzinger, C. F.; Wang, Y. X.; Rudnicki, M. A. Building Muscle: Molecular Regulation of Myogenesis. *Cold Spring Harb. Perspect. Biol.* **2012**, *4*, a008342–a008342.
152. Yin, H.; Price, F.; Rudnicki, M. A. Satellite Cells and the Muscle Stem Cell Niche. *Physiol. Rev.* **2013**, *93*, 23–67.
153. Clark, K. A.; McElhinny, A. S.; Beckerle, M. C.; Gregorio, C. C. Striated muscle

cytoarchitecture: an intricate web of form and function. *Annu. Rev. Cell Dev. Biol.* **2002**, *18*, 637–706.
154. Schultz, G. S.; Wysocki, A. Interactions between extracellular matrix and growth factors in wound healing. *Wound Repair Regen.* **2009**, *17*, 153–162.
155. Calve, S.; Simon, H.-G. Biochemical and mechanical environment cooperatively regulate skeletal muscle regeneration. *FASEB J.* **2012**, *26*, 2538–45.
156. Järvinen, T. A. H.; Järvinen, T. L. N.; Kääriäinen, M.; Kalimo, H.; Järvinen, M. Muscle Injuries: biology and treatment. *Am. J. Sports Med.* **2005**, *33*, 745–764.
157. Tidball, J. G. Mechanisms of Muscle Injury, Repair, and Regeneration. In *Comprehensive Physiology*; John Wiley & Sons, Inc.: Hoboken, NJ, USA, 2011; Vol. 1, pp. 2029–62.
158. Hayashi, S.; Aso, H.; Watanabe, K.; Nara, H.; Rose, M. T.; Ohwada, S.; Yamaguchi, T. Sequence of IGF-I, IGF-II, and HGF expression in regenerating skeletal muscle. *Histochem. Cell Biol.* **2004**, *122*, 427–34.
159. Grasman, J. M.; Zayas, M. J.; Page, R. L.; Pins, G. D. Biomimetic scaffolds for regeneration of volumetric muscle loss in skeletal muscle injuries. *Acta Biomater.* **2015**, *25*, 2–15.
160. Stern-Straeter, J.; Riedel, F.; Bran, G.; Hörmann, K.; Goessler, U. R. Advances in skeletal muscle tissue engineering. *In Vivo 21*, 435–44.
161. Mertens, J. P.; Sugg, K. B.; Lee, J. D.; Larkin, L. M. Engineering muscle constructs for the creation of functional engineered musculoskeletal tissue. *Regen. Med.* **2014**, *9*, 89–100.
162. Vandenburgh, H.; Del Tatto, M.; Shansky, J.; Lemaire, J.; Chang, A.; Payumo, F.; Lee, P.; Goodyear, A.; Raven, L. Tissue-engineered skeletal muscle organoids for reversible gene therapy. *Hum. Gene Ther.* **1996**, *7*, 2195–200.
163. Huang, Y.-C.; Dennis, R. G.; Larkin, L.; Baar, K. Rapid formation of functional muscle in vitro using fibrin gels. *J. Appl. Physiol.* **2005**, *98*, 706–13.
164. Bandiera, A.; Sist, P.; Urbani, R. Comparison of thermal behavior of two recombinantly expressed human elastin-like polypeptides for cell culture applications. *Biomacromolecules* **2010**, *11*, 3256–65.
165. Bandiera, A. Transglutaminase-catalyzed preparation of human elastin-like polypeptide-based three-dimensional matrices for cell encapsulation. *Enzyme Microb. Technol.* **2011**, *49*, 347–52.
166. Ciofani, G.; Genchi, G. G.; Liakos, I.; Athanassiou, A.; Mattoli, V.; Bandiera, A. Human recombinant elastin-like protein coatings for muscle cell proliferation and differentiation. *Acta Biomater.* **2013**, *9*, 5111–5121.
167. D'Andrea, P.; Scaini, D.; Severino, L. U.; Borelli, V.; Passamonti, S.; Lorenzon, P.; Bandiera, A. In vitro myogenesis induced by human recombinant elastin-like proteins. *Biomaterials* **2015**, *67*, 240–53.
168. D'Andrea, P.; Civita, D.; Cok, M.; Ulloa Severino, L.; Vita, F.; Scaini, D.; Casalis, L.; Lorenzon, P.; Donati, I.; Bandiera, A. Myoblast adhesion, proliferation and differentiation on human elastin-like polypeptide (HELP) hydrogels. *J. Appl. Biomater. Funct. Mater.* **2016**, *15*, 0–0.
169. Engler, A. J.; Sen, S.; Sweeney, H. L.; Discher, D. E. Matrix Elasticity Directs Stem Cell Lineage Specification. *Cell* **2006**, *126*, 677–689.
170. Uehata, M.; Narumiya, S.; Ishizaki, T.; Satoh, H.; Ono, T.; Kawahara, T.; Morishita, T.; Tamakawa, H.; Yamagami, K.; Inui, J.; Maekawa, M. Calcium sensitization of smooth muscle mediated by a Rho-associated protein kinase in hypertension. *Nature* **1997**, *389*, 990–994.
171. Engler, A. J.; Sen, S.; Sweeney, H. L.; Discher, D. E. Matrix elasticity directs stem cell lineage specification. *Cell* **2006**, *126*, 677–89.

172. Cellot, G.; Cilia, E.; Cipollone, S.; Rancic, V.; Sucapane, A.; Giordani, S.; Gambazzi, L.; Markram, H.; Grandolfo, M.; Scaini, D.; Gelain, F.; Casalis, L.; Prato, M.; Giugliano, M.; Ballerini, L. Carbon nanotubes might improve neuronal performance by favouring electrical shortcuts. *Nat. Nanotechnol.* **2009**, *4*, 126–133.
173. K.A.Shah, B. A. T. Synthesis of carbon nanotubes by catalytic chemical vapour deposition: A review on carbon sources, catalysts and substrates. *Mater. Sci. Semicond. Process.* **2016**, *41*, 67–82.
174. Chiang, W.-H.; Sankaran, R. M. Microplasma synthesis of metal nanoparticles for gas-phase studies of catalyzed carbon nanotube growth. *Appl. Phys. Lett.* **2007**, *91*, 121503.
175. Michaelis, F. B.; Weatherup, R. S.; Bayer, B. C.; Bock, M. C. D.; Sugime, H.; Caneva, S.; Robertson, J.; Baumberg, J. J.; Hofmann, S. Co-catalytic Absorption Layers for Controlled Laser-Induced Chemical Vapor Deposition of Carbon Nanotubes. *ACS Appl. Mater. Interfaces* **2014**, *6*, 4025–4032.
176. Liang Zhang, †; Zhongrui Li, †; Yongqiang Tan, †; Giulio Lolli, †; Nataphan Sakulchaicharoen, †; Félix G. Requejo, ‡; B. Simon Mun, § and; Daniel E. Resasco*, † Influence of a Top Crust of Entangled Nanotubes on the Structure of Vertically Aligned Forests of Single-Walled Carbon Nanotubes. **2006**.
177. C. J. Lee, J. Park, Y. Huh, J. Y. L. Temperature effect on the growth of carbon nanotubes using thermal chemical vapor deposition. *Chem. Phys. Lett.* **2001**, *343*, 33–38.
178. Charlier*, J.-C. Defects in Carbon Nanotubes. **2002**.
179. Costa, S.; Borowiak-Palen, E.; Kruszyńska, M.; Bachmatiuk, A.; Kaleńczuk, R. J. Characterization of carbon nanotubes by Raman spectroscopy. *Mater. Sci.* **2008**, *26*.
180. E.F. Antunes, A.O. Lobo, E.J. Corat, V. J. T.-A. Influence of diameter in the Raman spectra of aligned multi-walled carbon nanotubes. *Carbon N. Y.* **2007**, *45*, 913–921.
181. Bulusheva, L. G.; Okotrub, A. V.; Kinloch, I. A.; Asanov, I. P.; Kurenya, A. G.; Kudashov, A. G.; Chen, X.; Song, H. Effect of nitrogen doping on Raman spectra of multi-walled carbon nanotubes. *Phys. status solidi* **2008**, *245*, 1971–1974.
182. Saito, R.; Grüneis, A.; Samsonidze, G. G.; Brar, V. W.; Dresselhaus, G.; Dresselhaus, M. S.; Jorio, A.; Cançado, L. G.; Fantini, C.; Pimenta, M. A.; Filho, A. G. S. Double resonance Raman spectroscopy of single-wall carbon nanotubes. *New J. Phys.* **2003**, *5*, 157–157.
183. Kim, K. K.; Park, J. S.; Kim, S. J.; Geng, H. Z.; An, K. H.; Yang, C.-M.; Sato, K.; Saito, R.; Lee, Y. H. Dependence of Raman spectra G′ band intensity on metallicity of single-wall carbon nanotubes. *Phys. Rev. B* **2007**, *76*, 205426.
184. Roeges, N. P. G. *A guide to the complete interpretation of infrared spectra of organic structures*; Wiley, 1994.
185. Long, D. A. (Derek A. *Raman spectroscopy*; McGraw-Hill, 1977.
186. Mattevi, C.; Wirth, C. T.; Hofmann, S.; Blume, R.; Cantoro, M.; Ducati, C.; Cepek, C.; Knop-Gericke, A.; Milne, S.; Castellarin-Cudia, C.; Dolafi, S.; Goldoni, A.; Schloegl, R.; Robertson, J. In-situ X-ray Photoelectron Spectroscopy Study of Catalyst−Support Interactions and Growth of Carbon Nanotube Forests. *J. Phys. Chem. C* **2008**, *112*, 12207–12213.
187. Hofmann, S.; Blume, R.; Wirth, C. T.; Cantoro, M.; Sharma, R.; Ducati, C.; Hävecker, M.; Zafeiratos, S.; Schnoerch, P.; Oestereich, A.; Teschner, D.; Albrecht, M.; Knop-Gericke, A.; Schlögl, R.; Robertson, J. State of Transition Metal Catalysts During Carbon Nanotube Growth. *J. Phys. Chem. C* **2009**, *113*, 1648–1656.
188. M. Scardamaglia, M. Amati, B. Llorente, P. Mudimela, J.F. Colomer, J. Ghijsen, C. Ewels, R. Snyders, L. Gregoratti, C. B. Nitrogen ion casting on vertically aligned carbon nanotubes: Tip and sidewall chemical modification. *Carbon N. Y.* **2014**, *77*, 319–328.

189. Okpalugo, T. I. T.; Papakonstantinou, P.; Murphy, H.; McLaughlin, J.; Brown, N. M. D. High resolution XPS characterization of chemical functionalised MWCNTs and SWCNTs. *Carbon N. Y.* **2005**, *43*, 153–161.
190. Foldbjerg, R.; Irving, E. S.; Wang, J.; Thorsen, K.; Sutherland, D. S.; Autrup, H.; Beer, C. The toxic effects of single-walled carbon nanotubes are linked to the phagocytic ability of cells. *Toxicol. Res. (Camb).* **2014**, *3*, 228.
191. Patlolla, A.; Knighten, B.; Tchounwou, P. Multi-walled carbon nanotubes induce cytotoxicity, genotoxicity and apoptosis in normal human dermal fibroblast cells. *Ethn. Dis.* **2010**, *20*, S1-65–72.
192. Lovat, V.; Pantarotto, D.; Lagostena, L.; Cacciari, B.; Grandolfo, M.; Righi, M.; Spalluto, G.; Prato, M.; Ballerini, L. Carbon Nanotube Substrates Boost Neuronal Electrical Signaling. *Nano Lett.* **2005**, *5*, 1107–1110.
193. Latif, N.; Quillon, A.; Sarathchandra, P.; McCormack, A.; Lozanoski, A.; Yacoub, M. H.; Chester, A. H. Modulation of human valve interstitial cell phenotype and function using a fibroblast growth factor 2 formulation. *PLoS One* **2015**, *10*, e0127844.
194. Baum, J.; Duffy, H. S. Fibroblasts and myofibroblasts: what are we talking about? *J. Cardiovasc. Pharmacol.* **2011**, *57*, 376–9.
195. Levy, J. R.; Holzbaur, E. L. F.; Parsons, J. T.; Horwitz, A. R.; Schwartz, M. a; Larson, D. R.; Singer, R. H.; Zenklusen, D.; Campellone, K. G.; Welch, M. D.; Schneider-poetsch, T.; Ju, J.; Eyler, D. E.; Dang, Y.; Bhat, S.; Merrick, W. C.; Green, R.; Shen, B.; Liu, J. O.; Schnitzer, J.; Storm, N. Cell adhesion: integrating cytoskeletal dynamics and cellular tension. *Mol. Cell* **2010**, *11*, 633–643.
196. Lehnert, D.; Wehrle-Haller, B.; David, C.; Weiland, U.; Ballestrem, C.; Imhof, B. a; Bastmeyer, M. Cell behaviour on micropatterned substrata: limits of extracellular matrix geometry for spreading and adhesion. *J. Cell Sci.* **2004**, *117*, 41–52.
197. Ziegler, U.; Vinckier, a; Kernen, P.; Zeisel, D.; Biber, J.; Semenza, G.; Murer, H.; Groscurth, P. Preparation of basal cell membranes for scanning probe microscopy. *FEBS Lett* **1998**, *436*, 179–184.
198. Pampaloni, N. P.; Scaini, D.; Perissinotto, F.; Bosi, S.; Prato, M.; Ballerini, L. Sculpting neurotransmission during synaptic development by 2D nanostructured interfaces. *Nanomedicine Nanotechnology, Biol. Med.* **2017**.
199. Weisz, L.; Oren, M.; Rotter, V. Transcription regulation by mutant p53. *Oncogene* **2007**, *26*, 2202–2211.
200. Mullen, P. J.; Yu, R.; Longo, J.; Archer, M. C.; Penn, L. Z. The interplay between cell signalling and the mevalonate pathway in cancer. *Nat. Rev. Cancer* **2016**, *16*, 718–731.
201. Zhang, F. L.; Casey, P. J. Protein Prenylation: Molecular Mechanisms and Functional Consequences. *Annu. Rev. Biochem.* **1996**, *65*, 241–269.
202. Sorrentino, G.; Ruggeri, N.; Specchia, V.; Cordenonsi, M.; Mano, M.; Dupont, S.; Manfrin, A.; Ingallina, E.; Sommaggio, R.; Piazza, S.; Rosato, A.; Piccolo, S.; Del Sal, G. Metabolic control of YAP and TAZ by the mevalonate pathway. *Nat. Cell Biol.* **2014**, *16*, 357–366.
203. Zhang, C.; Liu, J.; Liang, Y.; Wu, R.; Zhao, Y.; Hong, X.; Lin, M.; Yu, H.; Liu, L.; Levine, A. J.; Hu, W.; Feng, Z. Tumour-associated mutant p53 drives the Warburg effect. *Nat. Commun.* **2013**, *4*, 2935.
204. Ingber, D. E. Cellular mechanotransduction: putting all the pieces together again. *FASEB J.* **2006**, *20*, 811–827.
205. Zhao, X.; Hu, X. Dosing of zoledronic acid with its anti-tumor effects in breast cancer. *J. bone Oncol.* **2015**, *4*, 98–101.

206. Yaffe, D.; Saxel, O. Serial passaging and differentiation of myogenic cells isolated from dystrophic mouse muscle. *Nature 270*, 725–7.
207. Çelebi, B.; Cloutier, M.; Balloni, R.; Mantovani, D.; Bandiera, A.; Bandiera, A. Human Elastin-Based Recombinant Biopolymers Improve Mesenchymal Stem Cell Differentiation. *Macromol. Biosci.* **2012**, *12*, 1546–1554.
208. Bellingham, C. M.; Lillie, M. A.; Gosline, J. M.; Wright, G. M.; Starcher, B. C.; Bailey, A. J.; Woodhouse, K. A.; Keeley, F. W. Recombinant human elastin polypeptides self-assemble into biomaterials with elastin-like properties. *Biopolymers* **2003**, *70*, 445–455.
209. Pepe, A.; Guerra, D.; Bochicchio, B.; Quaglino, D.; Gheduzzi, D.; Pasquali Ronchetti, I.; Tamburro, A. M. Dissection of human tropoelastin: Supramolecular organization of polypeptide sequences coded by particular exons. *Matrix Biol.* **2005**, *24*, 96–109.
210. Collinsworth, A. M.; Zhang, S.; Kraus, W. E.; Truskey, G. A. Apparent elastic modulus and hysteresis of skeletal muscle cells throughout differentiation. *AJP Cell Physiol.* **2002**, *283*, C1219–C1227.
211. Duan, B.; Yin, Z.; Hockaday Kang, L.; Magin, R. L.; Butcher, J. T. Active tissue stiffness modulation controls valve interstitial cell phenotype and osteogenic potential in 3D culture. *Acta Biomater.* **2016**, *36*, 42–54.
212. Engler, A. J.; Rehfeldt, F.; Sen, S.; Discher, D. E. Microtissue Elasticity: Measurements by Atomic Force Microscopy and Its Influence on Cell Differentiation. In *Methods in cell biology*; 2007; Vol. 83, pp. 521–545.
213. Peyton, S. R.; Putnam, A. J. Extracellular matrix rigidity governs smooth muscle cell motility in a biphasic fashion. *J. Cell. Physiol.* **2005**, *204*, 198–209.
214. Aragona, M.; Panciera, T.; Manfrin, A.; Giulitti, S.; Michielin, F.; Elvassore, N.; Dupont, S.; Piccolo, S. A Mechanical Checkpoint Controls Multicellular Growth through YAP/TAZ Regulation by Actin-Processing Factors. *Cell* **2013**, *154*, 1047–1059.
215. Zhao, B.; Wei, X.; Li, W.; Udan, R. S.; Yang, Q.; Kim, J.; Xie, J.; Ikenoue, T.; Yu, J.; Li, L.; Zheng, P.; Ye, K.; Chinnaiyan, A.; Halder, G.; Lai, Z.-C.; Guan, K.-L. Inactivation of YAP oncoprotein by the Hippo pathway is involved in cell contact inhibition and tissue growth control. *Genes Dev.* **2007**, *21*, 2747–61.
216. Gan, Q.; Yoshida, T.; Li, J.; Owens, G. K. Smooth Muscle Cells and Myofibroblasts Use Distinct Transcriptional Mechanisms for Smooth Muscle -Actin Expression. *Circ. Res.* **2007**, *101*, 883–892.
217. Lin, K. C.; Park, H. W.; Guan, K.-L. Regulation of the Hippo Pathway Transcription Factor TEAD. *Trends Biochem. Sci.* **2017**, *42*, 862–872.
218. Nardone, G.; Oliver-De La Cruz, J.; Vrbsky, J.; Martini, C.; Pribyl, J.; Skládal, P.; Pešl, M.; Caluori, G.; Pagliari, S.; Martino, F.; Maceckova, Z.; Hajduch, M.; Sanz-Garcia, A.; Pugno, N. M.; Stokin, G. B.; Forte, G. YAP regulates cell mechanics by controlling focal adhesion assembly. *Nat. Commun.* **2017**, *8*, 15321.
219. Affo, S.; Yu, L.-X.; Schwabe, R. F. The Role of Cancer-Associated Fibroblasts and Fibrosisin Liver Cancer. *Annu. Rev. Pathol. Mech. Dis.* **2017**, *12*, 153–186.
220. Calvo, F.; Ege, N.; Grande-Garcia, A.; Hooper, S.; Jenkins, R. P.; Chaudhry, S. I.; Harrington, K.; Williamson, P.; Moeendarbary, E.; Charras, G.; Sahai, E. Mechanotransduction and YAP-dependent matrix remodelling is required for the generation and maintenance of cancer-associated fibroblasts. *Nat. Cell Biol.* **2013**, *15*, 637–46.
221. Mosqueira, D.; Pagliari, S.; Uto, K.; Ebara, M.; Romanazzo, S.; Escobedo-Lucea, C.; Nakanishi, J.; Taniguchi, A.; Franzese, O.; Di Nardo, P.; Goumans, M. J.; Traversa, E.; Pinto-do-Ó, P.; Aoyagi, T.; Forte, G. Hippo pathway effectors control cardiac progenitor cell fate by acting

as dynamic sensors of substrate mechanics and nanostructure. *ACS Nano* **2014**, *8*, 2033–47.
222. Hinderer, S.; Seifert, J.; Votteler, M.; Shen, N.; Rheinlaender, J.; Schäffer, T. E.; Schenke-Layland, K. Engineering of a bio-functionalized hybrid off-the-shelf heart valve. *Biomaterials* **2014**, *35*, 2130–9.
223. Hasirci, V.; Kenar, H. Novel surface patterning approaches for tissue engineering and their effect on cell behavior. *Nanomedicine* **2006**, *1*, 73–90.
224. Kim, D.-H.; Kim, P.; Song, I.; Cha, J. M.; Lee, S. H.; Kim, B.; Suh, K. Y. Guided Three-Dimensional Growth of Functional Cardiomyocytes on Polyethylene Glycol Nanostructures. *Langmuir* **2006**, *22*, 5419–5426.
225. Usmani, S.; Aurand, E. R.; Medelin, M.; Fabbro, A.; Scaini, D.; Laishram, J.; Rosselli, F. B.; Ansuini, A.; Zoccolan, D.; Scarselli, M.; De Crescenzi, M.; Bosi, S.; Prato, M.; Ballerini, L. 3D meshes of carbon nanotubes guide functional reconnection of segregated spinal explants. *Sci. Adv.* **2016**, *2*, e1600087.
226. Bosi, S.; Rauti, R.; Laishram, J.; Turco, A.; Lonardoni, D.; Nieus, T.; Prato, M.; Scaini, D.; Ballerini, L. From 2D to 3D: novel nanostructured scaffolds to investigate signalling in reconstructed neuronal networks. *Sci. Rep.* **2015**, *5*, 9562.
227. Chen, W. L. K.; Simmons, C. a Lessons from (patho)physiological tissue stiffness and their implications for drug screening, drug delivery and regenerative medicine. *Adv. Drug Deliv. Rev.* **2011**, *63*, 269–76.
228. Pesce, M.; Santoro, R. Feeling the right force: How to contextualize the cell mechanical behavior in physiologic turnover and pathologic evolution of the cardiovascular system. *Pharmacol. Ther.* **2017**, *171*, 75–82.
229. Mabry, K. M.; Lawrence, R. L.; Anseth, K. S. Dynamic stiffening of poly(ethylene glycol)-based hydrogels to direct valvular interstitial cell phenotype in a three-dimensional environment. *Biomaterials* **2015**, *49*, 47–56.
230. Usprech, J.; Chen, W. L. K.; Simmons, C. A. Heart valve regeneration: the need for systems approaches. *Wiley Interdiscip. Rev. Syst. Biol. Med.* **2016**, *8*, 169–82.
231. Terzian, T.; Suh, Y.-A.; Iwakuma, T.; Post, S. M.; Neumann, M.; Lang, G. A.; Van Pelt, C. S.; Lozano, G. The inherent instability of mutant p53 is alleviated by Mdm2 or p16INK4a loss. *Genes Dev.* **2008**, *22*, 1337–44.
232. Hersel, U.; Dahmen, C.; Kessler, H. RGD modified polymers: biomaterials for stimulated cell adhesion and beyond. *Biomaterials* **2003**, *24*, 4385–415.
233. Blanchoin, L.; Boujemaa-Paterski, R.; Sykes, C.; Plastino, J. Actin Dynamics, Architecture, and Mechanics in Cell Motility. *Physiol. Rev.* **2014**, *94*, 235–263.
234. Discher, D. E.; Janmey, P.; Wang, Y.-L. Tissue Cells Feel and Respond to the Stiffness of Their Substrate. *Science (80-.).* **2005**, *310*, 1139–1143.
235. Lange, J. R.; Fabry, B. Cell and tissue mechanics in cell migration. *Exp. Cell Res.* **2013**, *319*, 2418–2423.
236. Pelham, R. J.; Wang, Y. l Cell locomotion and focal adhesions are regulated by substrate flexibility. *Proc. Natl. Acad. Sci. U. S. A.* **1997**, *94*, 13661–5.
237. J.W. Ward, B.Q. Wei, P. M. A. Substrate effects on the growth of carbon nanotubes by thermal decomposition of methane. *Chem. Phys. Lett.* **2003**, *376*, 717–725.
238. KERN; W. Cleaning solutions based on hydrogen peroxide for use in silicon semiconductor technology. *RCA Rev.* **1970**, *31*, 187–206.
239. Santoro, R.; Consolo, F.; Spiccia, M.; Piola, M.; Kassem, S.; Prandi, F.; Vinci, M. C.; Forti, E.; Polvani, G.; Fiore, G. B.; Soncini, M.; Pesce, M. Feasibility of pig and human-derived aortic valve interstitial cells seeding on fixative-free decellularized animal pericardium. *J. Biomed.*

Mater. Res. - Part B Appl. Biomater. **2016**, *104*, 345–356.
240. Alonso, J. L.; Goldmann, W. H. Feeling the forces: Atomic force microscopy in cell biology. *Life Sci.* **2003**, *72*, 2553–2560.
241. I.N.Sneddon The relation between load and penetration in the axisymmetric boussinesq problem for a punch of arbitrary profile. *Int. J. Eng. Sci.* **1965**, *3*, 47–57.
242. Sneddon, I. N. the Total Depth of Penetration of the Tip of the Punch, and for. *Int. J. Eng. Sci.* **1965**, *3*, 47–57.
243. Girardini, J. E.; Napoli, M.; Piazza, S.; Rustighi, A.; Marotta, C.; Radaelli, E.; Capaci, V.; Jordan, L.; Quinlan, P.; Thompson, A.; Mano, M.; Rosato, A.; Crook, T.; Scanziani, E.; Means, A. R.; Lozano, G.; Schneider, C.; Del Sal, G. A Pin1/Mutant p53 Axis Promotes Aggressiveness in Breast Cancer. *Cancer Cell* **2011**, *20*, 79–91.
244. Bandiera, A.; Taglienti, A.; Micali, F.; Pani, B.; Tamaro, M.; Crescenzi, V.; Manzini, G. Expression and characterization of human-elastin-repeat-based temperature-responsive protein polymers for biotechnological purposes. *Biotechnol. Appl. Biochem.* **2005**, *42*, 247–56.
245. Bandiera, A. ASSEMBLY AND OPTIMIZATION OF EXPRESSION OF SYNTHETIC GENES DERIVED FROM THE HUMAN ELASTIN REPEATED MOTIF. *Prep. Biochem. Biotechnol.* **2010**, *40*, 198–212.

Appendix

List of papers published or under submission:

1. Activation of human aortic valve interstitial cells by local stiffness involves YAP-dependent transcriptional signaling

Rosaria Santoro[1,*,] Denis Scaini [2,3,*], Luisa Ulloa Severino[3,4], Francesco Amadeo[1], Giacomo Bernava[1], Silvia Ferrari[1], Marco Agrifoglio[5], Loredana Casalis[3] and Maurizio Pesce[1, §]

1. Unità di Ingegneria Tissutale Cardiovascolare - Centro Cardiologico Monzino, IRCCS, Milan, ITALY
2. Scuola Internazionale Superiore di Studi Avanzati - via Bonomea, 265 – 34136, Trieste, ITALY
3. Elettra-Sincrotrone Trieste S.C.p.A. – 34149, Basovizza, Trieste, ITALY
4. Università di Trieste - Piazzale Europa, 1 – 34127, Trieste, ITALY
5. Dipartimento di Scienze Cliniche e di Comunità, Università di Milano – Via Parea 4 – 20138, Milan, ITALY

Abstract

The pathologic evolution of the valve interstitial cells (VICs) into pro-inflammatory and pro-calcific cells is recognized as one of the central events in calcific aortic valve (AoV) disease. While the paracrine pathways and the responsivity of VICs to the mechanical compliance of the surrounding environment are well characterized, the intracellular signaling elicited by variations in local stiffness and its link to cytoskeleton dynamics is less consolidated. By using a simple method to manufacture 2D poly-acrylamide gels with atomic force microscopy validated stiffness, we obtained adhesion substrates onto which human AoV VICs were plated, and subsequently investigated for the cytoskeleton dynamics and the activity of the mechanosensing-activated transcription factor YAP. We found that cells were subject to a reversible stiffness-dependent nuclear translocation of the transcription factor in concert with an increase in cytoskeleton tensioning and loading of the myofibroblast-specific protein αSMA onto the F-actin cytoskeleton. YAP was transcriptionally active in human VICs, and it was localized into the nucleus in cells present in regions of the valve leaflets juxtaposed to calcific lesions. Since determination of the tissue elasticity by AFM force mapping showed changes in the elasticity of healthy vs. calcific leaflets areas in the range associated to YAP nuclear translocation in vitro, we conclude that subtle variations in matrix stiffness are involved in mechanosensation-dependent VICs pathological programming in valve tissue.

This paper was submitted to Biomaterials in December 2017. I performed the mechanical characterization of substrates, cells and tissues by AFM.

2. Carbon nanotubes scaffold induce regulation of valvular interstitial cells fate

Luisa Ulloa Severino[1,2], I. Rago[1,2], F. Perissinotto[1,2], R. Santoro[3], M. Pesce[3], L. Casalis[2], D. Scaini[1,2]
1. University of Trieste, PhD course in Nanotechnology, Trieste, Italy
2. Elettra-Sincrotrone S.C.p.A., Trieste, Italy
3. Centro Cardiologico Monzino, IRCCS, Milano, Italy

Abstract

Calcific Aortic Valve Disease is the most common form of valve disease in the Western world and represents a major healthcare burden. The primary driver for valvular calcification is the differentiation of valvular interstitial cells (VICs) into a diseased phenotype, the osteoblastic-like cells.

Moreover, the disease induces significant changes in the organization, composition and mechanical properties of the extracellular matrix that it seems to contribute to the progression of the pathology altering cellular molecular signaling. Cells interact with ECM through the focal adhesion points (FAs). The FA number and distribution are modulated by the extracellular matrix rigidity and determine the intracellular tensions. FAs contain ECM receptors, called integrins, and cytoplasmatic protein, such as vinculin, connecting the actin stress fibers to the integrins. Vinculin plays an important role in mechano-transduction and an accumulation of this in FAs has a role in intracellular tensions regulation and ECM stiffness.

In recent years, the quest for biocompatible (nano)materials capable of mimicking the natural ECM for tissue regeneration has increased. Carbon nanotubes (CNTs) are optimal candidate in this context, showing dimensions comparable to fibril ECM constituents and both in-vitro and in-vivo cellular biocompatibility. In the present study, we show the mechanical, morphological and molecular properties of VICs grown on transparent, randomly oriented, CNTs. Using Atomic Force Microscopy and immunofluorescence experiments we assessed the biomechanics, morphology and the pathway involved in the mechanical stress in onset of pathology. We observed that cell density does not vary between VICs grown on CNts or glass controls, indicating that CNTs are not toxic for VICs. Interestingly a morphological variation between VICs grown on glass and on CNTs was pointed out. In particular we observed that, on CNTs, the percentage of myofibroblast (Mfib) diminishes significatively with respect to glass. M_{fib} are correlated with VICs differentiation into osteoblastic-like cells and, therefore, with a diseased

phenotype. A variation in the mechanical properties of fibroblast grown on CNTs was measured via AFM force-spectroscopy experiments, in particular Mfib grown on CNTs are a softer than those on controls. No difference has been observed, instead, for smooth muscle cell phenotype on both substrates. Our results identified CNTs as a promising material to engineer novel artificial scaffolds for aortic valve regeneration.

This paper is in preparation. I performed the experimental design, the immunofluorescence assays, all the mechanical characterizations by AFM and statistical analysis.

3. Mechanical cues control mutant p53 stability through a mevalonate–RhoA axis

Eleonora Ingallina[1], Giovanni Sorrentino[1,9], Rebecca Bertolio[1,2], Kamil Lisek[1,10], Alessandro Zannini[1,2],Luca Azzolin[3], Luisa Ulloa Severino[2,4], Denis Scaini[2,4], Miguel Mano[5,6], Fiamma Mantovani[1,2], Antonio Rosato[7], Silvio Bicciato [8], Stefano Piccolo[3] and Giannino Del Sal [1,2*]

1. Laboratorio Nazionale CIB, Area Science Park Padriciano, Trieste, Italy.
2. Dipartimento di Scienze della Vita, Università degli Studi di Trieste, Trieste, Italy.
3. Department of Molecular Medicine, School of Medicine, University of Padova, Padova, Italy.
4. NanoInnovation Lab at Elettra-Sincrotrone Trieste, Basovizza, Trieste, Italy.
5. Center for Neuroscience and Cell Biology, University of Coimbra, Coimbra, Portugal.
6. International Centre for Genetic Engineering and Biotechnology, Trieste, Italy.
7. Veneto Institute of Oncology IOV-IRCCS, Padova, Italy.
8. Department of Life Sciences, University of Modena and Reggio Emilia, Modena, Italy.
9. Laboratory of Metabolic Signaling, Institute of Bioengineering, Ecole Polytechnique Fé dé rale de Lausanne, Lausanne, Switzerland.
10. Max-Delbrück-Centrum for Molecular Medicine in Hemholtz Association, Berlin, Germany.

Abstract

Tumour-associated p53 missense mutants act as driver oncogenes affecting cancer progression, metastatic potential and drug resistance (gain-of-function). Mutant p53 protein stabilization is a prerequisite for gain-of-function manifestation; however, it does not represent an intrinsic property of p53 mutants, but rather requires secondary events. Moreover, mutant p53 protein levels are often heterogeneous even within the same tumour, raising questions on the mechanisms that control local mutant p53 accumulation in some tumour cells but not in their neighbours. By investigating the cellular pathways that induce protection of mutant p53 from ubiquitin-mediated proteolysis, we found that HDAC6/Hsp90-dependent mutant p53 accumulation is sustained by RhoA geranylgeranylation downstream of the mevalonate pathway, as well as by RhoA- and actin-dependent transduction of mechanical inputs, such as the stiffness of the extracellular environment. Our results provide evidence for an unpredicted layer of mutant p53 regulation that relies on metabolic and mechanical cues.

This paper was published on Nature Cell Biology in December 2017. I performed the single cell AFM force spectroscopy measurements and the AFM mechanical characterization of breast cancer tissues.

4. In vitro myogenesis induced by human recombinant elastin-like proteins

Paola D'Andrea [a, *], Denis Scaini [a, b], Luisa Ulloa Severino [a, b], Violetta Borelli [a],Sabina Passamonti [a], Paola Lorenzon [a, c], Antonella Bandiera [a]

a Department of Life Sciences, University of Trieste, I-34127 Trieste, Italy

b NanoInnovation Lab at ELETTRA, Synchrotron Light Source S.S. 14 km 163.5, 34012 Basovizza, Trieste, Italy

c Centre for Neuroscience B.R.A.I.N., University of Trieste, I-34127 Trieste, Italy

Abstract

Mammalian adult skeletal muscle has a limited ability to regenerate after injury, usage or trauma. A promising strategy for successful regenerative technology is the engineering of bio interfaces that mimic the characteristics of the extracellular matrix. Human elastin-like polypeptides (HELPs) have been synthesized as biomimetic materials that maintain some peculiar properties of the native protein. We developed a novel Human Elastin Like Polypeptide obtained by fusing the elastin-like backbone to a domain present in the a2 chain of type IV collagen, containing two RGD motives. We employed this peptide as adhesion substrate for C2C12 myoblasts and compared its effects to those induced by two other polypeptides of the HELP series. Myoblast adhered to all HELPs coatings, where they assumed morphology and cytoarchitecture that depended on the polypeptide structure. Adhesion to HELPs stimulated at a different extent cell proliferation and differentiation, the expression of Myosin Heavy Chain and the fusion of aligned fibers into multinucleated myotubes. Adhesion substrates significantly altered myotubes stiffness, measured by Atomic Force Microscopy, and differently affected the cells Ca^{2+} handling capacity and the maturation of excitation-contraction coupling machinery, evaluated by Ca^{2+} imaging. Overall, our findings indicate that the properties of HELP biopolymers can be exploited for dissecting the molecular connections underlying myogenic differentiation and for designing novelsubstrates for skeletal muscle regeneration.

This paper was published on Biomaterials in July 2015. I performed the characterization of HELPc coating by AFM imaging and AFM mechanical characterization of myotubes cells.

5. Myoblast adhesion, proliferation and differentiation on human elastin-like polypeptide (HELP) hydrogels

Paola D'Andrea[1], Deborah Civita[1], Michela Cok[1], Luisa Ulloa Severino[1,2], Francesca Vita[1], Denis Scaini[1,2], Loredana Casalis[2,3], Paola Lorenzon[1], Ivan Donati[1], Antonella Bandiera[1]
1 Department of Life Sciences, University of Trieste, Trieste – Italy
2 NanoInnovation Lab at ELETTRA Synchrotron Light Source, Basovizza, Trieste – Italy
3 B.R.A.I.N. Centre for Neuroscience, University of Trieste, Trieste – Italy

Abstract

Background

The biochemical, mechanical and topographic properties of extracellular matrix are crucially involved in determining skeletal muscle cell morphogenesis, proliferation and differentiation. Human elastin-like polypeptides (HELPs) are recombinant biomimetic proteins designed to mimic some properties of the native matrix protein; when employed as myoblast adhesion substrates, they stimulate in vitro myogenesis. Given the influence that the biophysical properties of extracellular matrix have on skeletal muscle cells, the aim of this work was to investigate the effects of HELP hydrogels on myoblasts' viability and functions.

Methods

We recently synthesized a novel polypeptide, HELPc, by fusing the elastin-like backbone to a 41aa sequence present in the α2 chain of type IV collagen, containing two arginyl-glycyl-aspartic acid (RGD) motifs. To obtain hydrogels, the enzymatic cross-linking of the HELPc was accomplished by transglutaminase. Here, we employed both non-cross-linked HELPc glass coatings and cross-linked HELPc hydrogels at different monomer densities, as adhesion substrates for C2C12 cells, used as a myoblast model.

Results

By comparing cell adhesion, proliferation and differentiation, we revealed several striking differences. Depending on support rigidity, adhesion to HELPc substrates dictated cell morphology, spreading, focal adhesion formation and cytoskeletal organization. Hydrogels greatly stimulated cell proliferation, particularly in low-serum medium, and partially inhibited myogenic differentiation.

ConclusionsOn the whole, the results underline the potential of these genetically engineered polypeptides as a tool for dissecting crucial steps in myogenesis.

This paper was published on Journal of Applied Biomaterials & Functional Materials in January 2017. I performed the AFM characterization of HELPc hydrogels.